

國立交通大學

電機與控制工程學系

博士論文

影像處理與電腦視覺技術應用於駕駛輔助系統之研究

A Study of Image Processing and Computer Vision Techniques for
Driving Assistance Systems



研究生：林全財

指導教授：吳炳飛 教授

中華民國九十八年六月

影像處理與電腦視覺技術應用於駕駛輔助系統之研究
**A Study of Image Processing and Computer Vision
Techniques for Driving Assistance Systems**

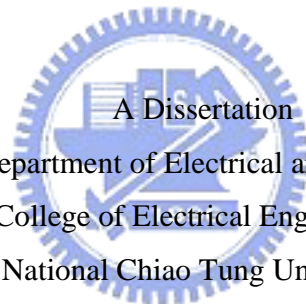
研究生：林全財

Student : Chuan-Tsai Lin

指導教授：吳炳飛

Advisor : Prof. Bing-Fei Wu

國立交通大學
電機與控制學系
博士論文



Submitted to Department of Electrical and Control Engineering
College of Electrical Engineering
National Chiao Tung University
in partial Fulfillment of the Requirements
for the Degree of
Doctor of Philosophy
in

Electrical and Control Engineering

June 2009

Hsinchu, Taiwan, Republic of China

中華民國九十八年六月

影像處理與電腦視覺技術應用於駕駛輔助系統之研究

研究生：林全財

指導教授：吳炳飛教授

國立交通大學電機與控制工程學系博士班

中文摘要

本論文主要探討應用於駕駛輔助系統之影像處理與電腦視覺技術，包括車道偵測、車輛偵測、前車距離估測、誤差估測及攝影機動態校正。電腦視覺為基礎(Vision-based)的駕駛輔助系統利用安裝在智慧車內的攝影機拍攝前方路況，透過車道與車輛偵測技術估測車道位置、前方車輛與智慧車的距離，這些資訊可以用來提高駕駛安全。本論文主要包含三個部份，第一部份簡介電腦視覺技術應用於駕駛輔助系統。第二部份為分析偵測道路所得的資訊及降低誤差的方法，第三部份則提出一些演算法，以應用於估測車輛距離及誤差、動態校正、以及車道與車輛偵測。

本論文提出一些新的方法來估測前車與智慧車的距離、快速估計前方物件的大小、距離與物件大小估測結果的誤差分析、及動態校正攝影機參數以降低誤差。首先，利用攝影機模型將世界座標的地平面座標轉換成影像座標，用以估計前方車輛與攝影機的相對位置，然後，利用一個新的估計方法估計前車的大小與投射的大小。這個方法利用前方車輛輪胎與地面的接觸點估計前車與攝影機的距離，並且利用前方車輛的其它頂點之投射位置，估計車輛的真實大小。因為前車投射的大小會隨著其與攝影機之距離而改變，論文中提出一個簡單且快速估計投射高度的方法，它能簡化繁複計算及降低計算時間，使得此設計能應用於即時處理系統。

距離估測的誤差分析結果顯示出當估測車輛與攝影機之間的距離時，攝影機的安裝參數也會影響到估測的結果，我們藉由誤差分析來找出最合適的攝影機參數以降低誤差。此

外，因為車輛會因路況不平或載重不平衡而晃動或傾斜，安裝在車上的攝影機的外在參數也會隨著車輛的行進晃動而改變，因此，我們亦提出了動態校正的方法，以取得正確的攝影機參數，降低估測誤差。實驗結果顯示我們的方法可以準確的估測車輛大小及距離。

論文中也提出了一個快速估測投射的車道與車道線寬度的方法，用以預測車道的可能位置。另外，設計了一個車道線擷取狀態機 Lane Marking Extraction (*LME*) Finite State Machine (*FSM*)，用以辨識影像中的車道線；並將 cubic B-spline 應用於曲線擬合以重建道路邊界。另外還發展了一個統計搜尋演算法用以決定在不同亮度條件下所設定的車道線擷取門檻值。此外，有時會有部份車道線被遮蔽而影響偵測，我們應用模糊演算法來判斷車道線可能被遮蔽的情形，進而利用已有的車道線資訊及估算的車道寬度補償被遮蔽的部份資訊。最後，為了加速偵測、減少偵測誤差及影像雜訊干擾，亦規劃一個 *ROI* (Region of Interest) 決定策略，它能提高偵測系統的穩健性並加快偵測速度。

另外，本論文發展了一個以模糊邏輯演算法為基礎的外形大小相似性演算法(Contour Size Similarity, *CSS*)。利用偵測和估測的影像中車輛大小的比較結果及模糊規則來辨識車輛。車輛偵測主要針對和智慧車相同車道的前方車輛。實驗結果顯示提出的方法可以有效的偵測車輛並估計其距離，而且當有車輛切入前方車道時，偵測的目標也會轉移到目前因切入而成為離智慧車最近的這一輛車。最後章節呈現了本篇論文的結論與未來的研究展望。

A Study of Image Processing and Computer Vision Techniques for Driving Assistance Systems

Student : Chuan-Tsai Lin

Advisor : Prof. Bing-Fei Wu

Department of Electrical and Control Engineering
National Chiao Tung University

ABSTRACT

The dissertation aims to explore techniques of image processing and computer vision applicable to driving assistance system, including lane detection, vehicle detection, estimation of the distance to the preceding car, error estimation, and dynamic calibration of cameras. The vision-based driving assistance system films the front road scenes with a camera equipped on the intelligent vehicle, computes lane positions and the distance to the preceding car by the lane and vehicle detection and then adopts the obtained information to improve driving safety. The dissertation mainly includes three sections. The first section is a brief introduction of the application of computer vision techniques to the driving assistance system. The second section presents analyses of the information obtained from lane detection and approaches for reducing errors. The third section proposes some algorithms and their application to the range estimation, error estimation, dynamic calibration, and detection of lanes and vehicles.

The dissertation presents several approaches to estimate the range between the preceding vehicle and the intelligent vehicle, to compute vehicle size and its projective size, and to dynamically calibrate cameras. First, a camera model is developed to transform coordinates from the ground plane onto the image plane to estimate the relative positions between the detected vehicle and the camera. Then, a new estimation method is proposed to estimate the actual and projective size of the preceding vehicle. This method can estimate the range between the preceding vehicle and the camera with the information of the contact points between vehicle tires and the ground and then estimate the actual size of the vehicle according to the positions of its vertexes in the image. Because the projective size of a vehicle varies with its distance to the camera, a simple and rapid method is presented to estimate the vehicle's projective height, which

allows a reduction of the computation time in the size estimation of the real-time systems.

Errors caused by the application of different camera parameters are also estimated and analyzed in this study. The estimation results are used to determine suitable parameters during camera installation to reduce estimation errors. Finally, to guarantee robustness of the detection system, a new efficient approach of dynamic calibration is presented to obtain accurate camera parameters, even when they are changed by camera vibration arising from on-road driving. Experimental results demonstrate that our approaches can provide accurate and robust estimation of range and size of the target vehicles.

In the dissertation, an approach for rapidly computing the projective lane width is presented to predict the projective lane positions and widths. Lane Marking Extraction (*LME*) Finite State Machine (*FSM*) is designed to extract points with features of lane markings in the image and a cubic B-spline is adopted to conduct curve fitting to reconstruct road geometry. A statistical search algorithm is also proposed to correctly and adaptively determine thresholds under various kinds of illumination. Furthermore, parameters of the camera in a moving car may change with vibration, so a dynamic calibration algorithm is applied to calibrate camera parameters and lane widths based on the information of lane projection. Besides, a fuzzy logic is used to discern the situation of occlusion. Finally, an *ROI* (Region of Interest) determination strategy is developed to narrow the search region and make the detection more robust with respect to the occlusion on the lane markings or complicated changes of curves and road boundaries.

The developed fuzzy-based vehicle detection method, Contour Size Similarity (*CSS*), performs the comparison between the projective vehicle sizes and the estimated ones by fuzzy logic. The aim of vehicle detection is to detect the closest preceding car in the same lane with the intelligent vehicle. Results of the experiments demonstrate that the proposed approach is effective in vehicle detection. Furthermore, the approach can rapidly adjust to the changes of detection targets when another car cuts in the lane of the intelligent vehicle. Finally, a conclusion and future works are also presented.

誌 謝

終於等到這榮耀的一刻，感覺收獲滿滿，充實自在，辛苦耕耘，含淚收割的果實真是甜美。回首近六年來的酸甜苦辣，感謝有這些波濤起伏的過程，豐富了我生命的色彩。心中充滿感謝，感謝很多人的幫助，讓我可以完成這艱鉅的使命。

感謝敬愛的指導教授 吳炳飛教授，嚴謹的教學態度與孜孜不倦的研究精神，啟發我很多教學及研究的方法，恩師所給的兼具理論與實務的研究方向，使我可以深入探索影像處理與電腦視覺研究領域的奧秘，進而在這幾年的研究及學習上獲益匪淺。恩師的成長經歷及奮鬥過程更是學生的榜樣，值得終身學習。

感謝口試委員曾定章教授、張志永教授、賈叢林教授、蘇崇彥教授、陳彥霖教授在論文口試時的細心斧正與指導，使論文更臻完善。感謝林昇甫教授、張志永教授、鄒應嶼教授、董蘭榮教授及林一平教授在課業上的教導，使我能順利完成博士班的課業。感謝阿霖在論文寫作上提供了很多很好的建議，感謝忠哥、暉哥、馬哥、世孟、坤卿、重甫在研究上，分享了很多的經驗，感謝阿誠、淑閔、秉宗、至明、威儀、正隆及實驗室的學長學弟，在準備實驗裝備上的協助。感謝和我一起修課的東龍、堯俊、則全、富章、信元、松傑、學長同學學弟們，一起準備考試、團隊合作完成作業，你們是我的最佳拍檔，我想我會很懷念在 CSSP 實驗室夜宿苦戰的日子。

感謝碩士班的指導教授劉立頌教授，奠定我理論及研究的基礎。您對學生的關心鼓勵與親切的教導，也讓我學習到做人處世應有的態度，對事物的看法更為宏觀。

感謝彰化師大附工鍾校長瑞國、劉校長豐旗、與黃校長榮文的鼓勵與對進修的支持，讓我能有機會持續充實本職學能。

感謝彰化師大附工電子科的老師同仁，瑞祥老師、朝發老師、志洋老師、永安老師、文漢老師、旺泉老師、文欽老師、建斌老師、志文老師、玉燕老師、明聰老師、及萬金老師在很多方面的教導與協助；生活上、工作上、專業教學上的經驗分享讓我減少很多獨自摸索的時間，也讓我的進修學習過程更為順利。感謝勝正、曜忠、天助、泰天、俊宏、冠宇、豐溢、志偉、信宏、行健、穎俊、勝民、美惠、國隆及這一路相伴的很多學長、同學與好朋友們，謝謝你們的鼓勵及分享了很多學習上、工作上的寶貴經驗，讓我在無形中增添了很多智慧，慶幸我有很多好朋友在我的學習歷程中，給我各方面的支援。還有很多曾

經教導我、幫助我、鼓勵我的師長、同仁、朋友，無法一一致意，謹在此表達由衷的感謝，謝謝您們。

感謝父親母親哥哥姊姊家人們，您們的支持與鼓勵是我的最大動力來源，您們也是我最有力的後盾。感謝兩個寶貝俞叡與庭陞，你們兩個小調皮總在將家裡搞得天翻地覆的時候，讓老爸有個鍛鍊身體運動的機會，你們天真無邪的歡笑聲，也讓我發現人生的更重要價值，一切憂愁隨之飄散。感謝摯愛的妻子曉蕙，無論家庭的照料、論文的校稿、甚至連道路實驗時，擔任實驗車的駕駛助手，都有極高效能的表現，你是最佳賢內助，感謝有你。

感謝父母、家人、親朋好友們在我遭逢挫折，論文屢次被拒的極度低潮時，對我的支持鼓勵，讓我雖深陷困厄，仍然從未曾想過放棄，終於能在畢業前能有五篇國際期刊論文及一個發明專利的成果，謹將這榮耀獻給您們。未來也期許自己能秉持虛心求知的精神持續學習，在面對人生的各種挑戰上，盡力扮演好自己的角色。

林全財 於 交通大學電機與控制工程學系 CSSP 實驗室 2009/6/1



Contents

摘要.....	iii
ABSTRACT	v
誌謝	viii
Contents	ix
List of Figures	xii
List of Tables	xv
Chapter 1 Introduction	1
1.1 Motivation	1
1.2 Literature Survey	2
1.2.1 Range Estimation and Dynamic Calibration	2
1.2.2 Lane Detection	4
1.2.3 Vehicle Detection	7
1.3 Research Objectives and Organization of the Thesis	8
Chapter 2 Range Estimation and Dynamic Calibration	11
2.1 Introduction	11
2.2 Position and Size estimation using Projective Geometry	12
2.2.1 Coordinates transformation Model	12
2.2.2 Rapid Estimation of Projective Height	15
2.3 Range and Error Estimation	19
2.3.1 Digitalized Equation of Range Estimation	19
2.3.2 Error Estimation	21
2.3.2.1 Quantization errors	21
2.3.2.2 Influence of Changes in Translation	22
2.3.2.3 Influence of Changes in Camera Tilt Angles	23

2.3.2.4 Influence of Changes in Camera Pan Angles	24
2.3.2.5 Influence of Changes in Camera Swing Angles	25
2.4 Dynamic Calibration Method	27
2.5 Application and Experimental Results	28
2.5.1 Performance Evaluation on Range Estimation	29
2.5.2 Simulation Results of Height Estimation	32
2.5.3 Dynamic Calibration of the Swing Angle	33
2.5.4 Comparative Performance Evaluation	34
Chapter 3 Lane Detection	37
3.1 Introduction	37
3.2 Camera Model with Dynamic Calibration	38
3.2.1 Camera Model	38
3.2.2 Rapid Estimation of the Projective Width	41
3.2.3 Dynamic Calibration	42
3.3 Lane Detection	46
3.3.1 Model of Lane Markings	46
3.3.2 Lane Marking Extraction	47
3.3.3 ROI Determination Strategy	51
3.3.4 Post processing by Fuzzy Reasoning	59
3.3.5 Reconstruction Process of Occluded lanes	61
3.3.6 Overall Process of Lane Detection	64
3.4 Experimental Results	65
3.4.1 Lane Detection Results	66
3.4.2 Comparative Performance Evaluation	81
3.4.3 Comparative Analysis	89
Chapter 4 Vehicle Detection	91
4.1 Introduction	91

4.2 Vehicle Model	91
4.2.1 Vehicle Features	92
4.2.2 Adaptive Edge Detection	94
4.3 Vehicle Detection Based on Contour Size Similarity	94
4.3.1 Vehicle Detection Procedures	95
4.3.2 Fuzzy Match	97
4.3.3 Vehicle Recognition Based on Fuzzy Rules	100
4.3.4 Vehicle Recognition Based on a Defuzzifier	100
4.4 Experimental Results	100
4.4.1 Vehicle Detection Results	101
4.4.2 Comparative Analysis	104
Chapter 5 Conclusion and Future Works	106
5.1 Range Estimation and Dynamic Calibration	106
5.2 Lane Detection	106
5.3 Vehicle Detection	107
5.4 Future works	108
Appendix A Relation of Projected Width and ν-coordinate	109
Appendix B Adaptation to Illumination Conditions	111
Reference	115
Vita	126
Publication List.....	127
專利證書—發明名稱：車輛週圍障礙物之偵測方法及顯示方法.....	129

List of Figures

Figure 1-1. Structure of the thesis.....	10
Figure 2-1. Coordinate transformation between image plane and ground plane.....	13
Figure 2-2. The projective geometry of a camera model. (a) A cuboid C . (b) Side view. (c) Top view.....	14
Figure 2-3. Relation between M - N image coordinates and u - v image coordinates.....	21
Figure 2-4. The relation between the Z -axis and the direction of movement of vehicles, denoted by \vec{S}	26
Figure 2-5. Relation between the Coordinates (u, v) and (u', v')	26
Figure 2-6. Projection of a vehicle and lane markings in the image coordinates....	28
Figure 2-7. A comparison between the manual range measurement and the estimated range.....	29
Figure 2-8. A comparison between the manual height measurement and the estimated height.....	30
Figure 2-9. A comparison of estimation results between Schoepflin's approach and ours.....	31
Figure 2-10. Estimation of a cuboid's projective height.....	32
Figure 2-11. Dynamic calibration of the swing angle.....	33
Figure 2-12. The swing angle calculated by Liang <i>et al</i> 's and our approaches. (a) Straight lane markings. (b) The curve of lane markings.....	36
Figure 3-1. The projective geometry of a camera model. (a) The mapping of the Y and Z coordinates on the v -coordinate; (b) The mapping of the X and Z coordinates on the u -coordinate.....	40
Figure 3-2. Relation between $w_L(v)$ and the v -coordinate.....	40
Figure 3-3. The estimated vanishing point.....	44

Figure 3-4. Lane Marking Model on a road with lane markings. (a)Actual lane marking image; (b)The gray level distribution of (a); (c) The gray level distribution of lane markings in the image coordinates; (d) The variance of gray level in a row of lane marking.....	46
Figure 3-5. The lane marking's relative positions to P_A and P_B in different states.....	48
Figure 3-6. State diagram of <i>LME FSM</i>	49
Figure 3-7. The flow chart of the selection of ROI determination strategies.....	51
Figure 3-8. <i>ROI</i> of fixed area.....	53
Figure 3-9. (a)Bi-directional expansion scheme; (b) Tendency expansion scheme.....	55
Figure 3-10. The acquirement of <i>BFT</i> in a fixed area.....	56
Figure 3-11. The select of <i>ROI</i> and its range. (a)(b)(c) The application of the expansion approach; (d) The adoption of the tracking approach.....	58
Figure 3-12. The B-spline model for lane marking detection.....	63
Figure 3-13. Procedures of the lane marking detection.....	64
Figure 3-14. The result of the dynamic calibration of camera's tilt angle.....	66
Figure 3-15. The estimated lane width in every frame.....	67
Figure 3-16. The gray level of lane markings under different illumination. (a) General light;(b) Strong sunshine; (c)Dusk ; (d) Night.....	68
Figure 3-17. (a) Curves; (b) A slope; (c)(d) A cloverleaf interchange.....	72
Figure 3-18. (a)(b)(c)(d)(e)(f) Situations of occlusion with different obstacles.....	75
Figure 3-19. Results of the nighttime road scene. (a)(b) With road lamps; (c)(d) Without road lamps.....	77
Figure 3-20. The detection results under strong sunlight. (a)(b) No occlusion of vehicles; (c)(d) with the occlusion of a vehicle.....	79
Figure 3-21. The detection result of a motorcycle inside and outside the lane. (a)	

Inside; (b) Outside.....	80
Figure 3-22. Results of the road scene that the lane markings are occluded with shadows, signs of braking. (a) Results of Jung and Kelber's [41]; (b) Results of the proposed approach.....	82
Figure 3-23. Results of road scenes with a curve lane and occlusion. (a)Results of Jung and Kelber's [41]; (b) Results of the proposed approach.....	83
Figure 3-24. Results of the road scene under strong sunlight. (a)Results of Jung and Kelber [41]; (b) Results of the proposed approach.....	84
Figure 3-25. Results of the nighttime road scene. (a). Results of Jung and Kelber's [41]; (b) Results of the proposed approach.....	86
Figure 3-26. Results of the road scene with a S-shaped lane. (a)(b) Results of Jung and Kelber's [41]; (c)(d) Results of the proposed approach.....	88
Figure 4-1. (a) The projection of an obstacle in the image. (b) The projection of a pattern in the image. (c) The relation between H_w and h_i	93
Figure 4-2. Vehicle detection flowchart.....	96
Figure 4-3. (a) Size of the obstacle projected on the image. (b) Size of the vehicle projected on the image.....	97
Figure 4-4. (a) The membership function of F_h (b) The membership function of F_v	99
Figure 4-5. Vehicle detection with regular illumination.....	101
Figure 4-6. Vehicle detection with patterns on the road.....	102
Figure 4-7. Vehicle detection under sunny conditions.....	102
Figure 4-8. The results of vehicle detection with vehicles cutting in the lane of the autonomous vehicle.....	103
Figure 4-9. Results of lane and vehicle detection.	104
Figure B-1. The gray level distribution with a row of lane marking in the search window.....	111

List of Tables

Table 2-1 Relations between N and Z coordinates.....	19
Table 2-2 Error analysis of range estimation.....	20
Table 2-3 Error analysis of range estimation caused by change of tilt angles	22
Table 2-4 Variation ratio between P_1 and P_3 on the Z -coordinate.....	24
Table 2-5 Variations between (u, v) and (u', v')	25
Table 2-6 Experimental results of camera angle estimation.....	31
Table 2-7 Comparison of Approaches.....	35
Table 2-8 A comparison in estimation results of camera angle and errors.....	35
Table 3-1 Denotations of the five G_d conditions.....	50
Table 3-2 The computation timings under different conditions by the proposed system.....	66
Table 3-3 Results of lane width estimation in the four situations.....	69
Table 3-4 The obtained parameters under different illumination conditions.....	70
Table 3-5 Comparison of different algorithms.....	90
Table 4-1 Comparison of Approaches in Lane and Vehicle Detection.....	105

Chapter 1

Introduction

1.1 Motivation

Driving assistance systems have become an active research area in recent years for developing intelligent transportation systems (ITS). On average, there is at least one man dying of vehicle crash every minute and more than 10 million people getting injured in the auto accidents, 2 or 3 million of whom are seriously wounded. Therefore, researches concerning crash avoidance, the reduction of injury and accidents, and the manufacture of safer vehicles are very important. Vehicle accident statistics reveal that the greatest threat to a driver comes from other vehicles. Accordingly, the objective of automatic driving assistance systems is to provide drivers with the information with respect to the surrounding traffic environment to lower the possibility of collision [1]-[3].

Currently, various sensors have been applied to driving assistance systems. Driving assistance systems require information regarding lanes, the preceding vehicle and its range to the intelligent vehicle. Lane detection usually entails vision-based techniques, which require the use of single cameras or stereo cameras. Approaches to vehicle detection and range estimation are multiple. Besides vision-based techniques, laser sensors are often adopted. If a system involves several or many kinds of sensors, the cost will rise and the complexity of the system will increase. By contrast, the use of only a single camera can significantly reduce the cost.

The preceding lane scenes can be filmed by the camera mounted in a vehicle. Parameters of

the camera can affect the results of range estimation; however, the parameters are easily changed by the vibration caused by the vehicle movements. Therefore, setting parameters correctly to reduce errors and dynamic camera calibration are necessary issues for researches. Besides, vehicles often move rapidly so driving assistance systems should be able to promptly respond to results of lane and vehicle detection to avoid the occurrence of traffic accidents. Hence, the acceleration of detection is also a major research issue. Furthermore, adaptive lane and vehicle detection systems are required to cope with changes of weather and illumination in the outdoor environment. Accordingly, the objective of this study is to develop methodologies for adaptive and real-time driving assistance systems [4]-[8].

1.2 Literature Survey

1.2.1 Range Estimation and Dynamic Calibration

Previous studies often adopted laser, radar or computer vision techniques in range estimation issues. For example, Chen [9] presented a radar-based detector to find obstacles in the forward collision warning system, where a vision-based module was adopted to confirm that the detected object is not an overhead structure to avoid false alarms of the warning system. Segawa et al. [10] developed a preceding vehicle detection system for collision avoidance by using a combination of stereo images and non-scanning millimeter-wave radar. In Hautiere et al.'s method [11], a depth map of the road environment is computed and applied for detecting the vertical objects on the road. Stereo-vision based techniques can also be applied on range estimation. By comparing the disparities of two images, obstacles can be detected and their distance to the experimental vehicle can also be estimated [11][12]. However, the methods above need multiple cameras or at least one set of radar to detect obstacles and estimate the range. If only one single camera is required, the cost and the complexity of the system will be significantly decreased. Nevertheless, the estimation results

of a single camera are often influenced by external camera parameters and thus serious errors arise. For example, an outdoor camera is often affected by the wind or rain. Furthermore, camera parameters vary with the pressure of tires, unbalanced load or bumpy roads when the camera is mounted on a moving vehicle. Therefore, automatic calibration is necessary to deal with the above issues. Studies of camera calibration usually adopted points in the world coordinates or certain distinctive patterns [13]-[15]. For instance, Wang and Tsai [13] proposed a camera calibration approach using a planar hexagon pattern drawn on the ground. However, this approach may only be suitable for calibration of fixed cameras. Schoepflin and Dailey [14] supposed the camera swing angle was zero and searched for the vanishing point by extending lane markings in the image to calibrate the tilt angle. Nevertheless, when the camera swing angle is not zero, errors may arise. Liang, *et al.* [15] calibrated the tilt angle of a moving camera with the coordinate of the vanishing point. However, the assumption of vehicles staying in the center of lanes may not be reasonable under typical driving conditions and thus such methods may cause more errors on roads with curves. Therefore, it is better if calibration targets are objects available on the road and errors caused by incomplete assumptions should be estimated. In fact, camera intrinsic parameters are usually fixed while extrinsic parameters such as angles and heights are variable. Intrinsic parameters can be obtained by analyzing a sequence of images captured by cameras [16]-[19]. To solve the problem of changing extrinsic parameters, we propose an approach of automatic calibration to provide robust range estimation for vision-based systems.

Object features, like sizes and shapes, are widely employed in the recognition of objects [20]-[25]. Yilmaz *et al.*[20] adopted a method of contour-based object tracking to detect pedestrians and to solve the problem of occlusion between objects. Lin *et al.*[21] computed the number of people in crowded scenes by detecting features of human heads. Pang *et al.*[22] analyzed vehicle projections with geometry and divided their occlusions in the images to

provide essential information to the traffic surveillance systems. Broggi *et al.*[23] utilized inverse perspective mapping to transfer images of the front driving lanes into a bird's view of parallel lanes to detect and identify vehicles with a bounding box. However, most of the above-mentioned approaches may need the prior information about the projective size and shape of the target object, and it may not be possible to obtain this information accurately and rapidly in many situations. Moreover, the loss of dimensional information during the transformation from 3-D coordinates to 2-D image coordinates often increases difficulties in estimating the projective size and shape of the target object. To solve the problem, we regard a vehicle as a cuboid and with the world coordinates of the cuboid's vertex on the ground, we can estimate the world coordinates of other vertices in the cuboid, determine their projective positions and estimate the size of the cuboid. Since vehicle sizes are within certain ranges, cuboids on the drive lanes whose sizes fit general vehicle sizes should be vehicles. So our method can be applied to vehicle recognition.



1.2.2 Lane Detection

There are many ways lane detection can be achieved. In early studies, Dickmanns *et al.* [26]-[28] conducted 3-D road recognition by adopting horizontal and vertical mapping models, the approach of extracting features with edge elements, and recursive estimation techniques. The results were applied to their test vehicle (VaMoRs) to function as autonomous vehicle guidance. Broggi *et al.* [29][30] used *IPM* (Inverse Perspective Mapping) to transfer a 3-D world coordinate to a 2-D image coordinate, and detected road markings using top-view images. Kreucher and Lakshmanan [31] suggested detecting lane markings with frequency domain features that capture relevant information about edge-oriented features. The objectives of many studies on lane detection include autonomous vehicle guidance and driving assistance such as lane-departure-warning and Driver-Attention Monitoring systems. Some

assumptions in common are as follows: 1) The road is flat or follows a precise model. 2) The appearance of lane markings follows strict rules. 3) The road texture is consistent. The main difficulty in lane detection is how to recognize roads efficiently in various situations, including complex shadowing and changes in illumination [32][33]. Furthermore, the vibration of a moving camera causes changes in camera parameters and thus leads to errors in geometric transformation. To solve the problem, dynamic calibration of cameras is required to improve robustness [34]-[36].

The task of lane detection can be summarized as two main sections: 1) The acquirement of features. 2) A road model for reconstructing road geometry. In addition, to accelerate the detection and make it robust, some approaches are added such as narrowing the search region, the determination of *ROI* (Region of Interest), dynamic calibration for the camera and position-tracking methods using consecutive images.

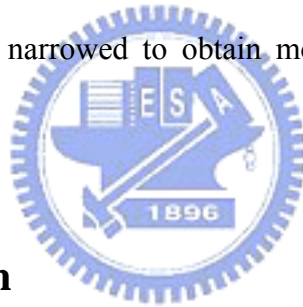
The first step of detecting lanes is to extract their features. On most occasions there are lane markings on both the left and the right side of the driving lane, while sometimes only the boundaries of the road exist without any lane marking. Most parts of the lane markings are like two parallel ribbons with some variations, for example, being straight or curved, solid lines or dashed lines, and in the color of white, yellow or red. The occlusion of trees and buildings and their shadows makes it more difficult to detect positions of lanes. Also, visibility varying with illumination increases difficulty to detections [37]-[41].

In acquiring features, there are four major types of methods: pixel-based, edge detection-based, marking-based, and color-based methods. The pixel-based type is to classify pixels into certain domains and put pixels of the road boundaries in one category [42]-[44]. The edge detection-based type involves conducting edge detection in the image first. Then, find straight lines with Hough transform [45][46] or adopt an ant-based approach to start a bottom-up search for possible path of the road boundary in the image [47]-[50] or determine

search regions by road models for detection of road boundaries [1][51]-[53]. Those two methods are time-consuming, and easily cause errors when complex shadows or obstacle occlusion exist. The marking-based type is based on features of lane markings. For example, Bertozzi and Broggi [29] proposed *IPM* and black-white-black transitions to detect lane markings. This method may effectively deal with some situations of shadows or obstacle occlusions. However, the vibration caused by the moving vehicle may influence the extrinsic parameters of the camera, and thus arouse unexpected mapping distortions on images, which may cause errors on lane detection results. The color-based type is to utilize color information of the road in the image [44][54]-[56]. In this way, there is more information about the lane and better abilities to resist noise. However, it takes more computation time to extract color features of interest.

Since shadows of trees or other noises usually exist and some lane markings are dash lines, the detected features of road boundaries are often incomplete. Therefore, the methods of interpolation or curve fitting are needed to reconstruct the road geometry. Kreucher and Lakshmanan [31] used a deformable template shape model to detect lanes. They believed that two sides of a road respectively approximate a quadratic equation, so they established their coefficients to determine the curvature and orientation of the road. However, curve fitting cannot be done by a quadratic equation on the lanes with S-shaped turns. So Wang *et al.* [57] adopted spline interpolation which can be used in various curves to connect line segments. However, when there are vehicles in the lane occluding parts of the lane boundary, some errors may arise, because this approach found a vanishing point depending on Hough transform followed by line-length voting. Thus, vehicles on the lanes may form spurious lines which may influence the determination of the vanishing line. Furthermore, Hough transform and Canny edge detector utilized in Wang *et al.*'s approaches may take more computation time.

Another issue to promote lane detection efficiency and depress noise sensitivity is to set appropriate *ROI*. Lin *et al.*[58] applied the information of both lane boundaries obtained from initial detection in the first frame to the finding of *ROI* on Hough domain. Then *ROI* was adopted as search parameters of lane boundaries in the subsequent frames. The method can effectively accelerate lane detection process on a straight lane but errors may arise on road curves. Chapuis *et al.*'s method [59] utilized an initially determined *ROI* to recursively recognize a probabilistic model to conduct iterative computation, and adopted a training phase to define the best interesting zone. The initially set *ROI* is effective in the general roads; however, diverse road curves may make the initial *ROI* too large on the farther part of the road and thus raise noise sensitivity. Therefore, an effective method is needed for adaptive determination of *ROI* and adjustment to changes of road curves in the image sequences, and thus *ROI* can be significantly narrowed to obtain more accurate and faster lane detection results.



1.2.3 Vehicle Detection

Besides lane detection, detections of obstacles and vehicles are also important issues in the research of crash avoidance and vehicle following. Some investigations exploited stereo visual systems to detect obstacles by comparing differences between two images [60][61]. Two cameras were required by those approaches, and thus the cost increased. In some previous studies, an obstacle was recognized as a vehicle by its shape and symmetry [12][62]-[64]. Practically, features of the vehicles presented in the images are also helpful to the detection. Sun *et al.* analyzed features of vehicles in the images, segmented and recognized vehicles with a Gabor filter and neural network techniques. In their study, the possible positions of vehicles were checked with hypothesis generation (HG) first and then the presence of the vehicles was verified by hypothesis verification (HV) [65][66]. Some

researchers performed optical flow analysis to detect obstacles. In consecutive images, positions of an object only have slight changes. Therefore, in the subsequent images, an object is found by the prediction of its motion based on its previous position [67]-[69]. Still, some problems may increase the detection time and make it difficult to achieve real-time vehicle detection. For example, the range between the camera and a recognizable vehicle is about 5-60m. The size of the vehicle in the range of 5m has changed enormously from that in the 60m. Besides, the diversity of vehicle colors, shapes, and sizes complicates the design of classifiers in vehicle recognition. Therefore, to detect vehicles rapidly, the feature of a rectangle-like contour in most vehicles should be adopted and the problem that projective sizes of vehicles vary with their range to the camera should be taken into consideration.

In vehicle detection, an approach of geometry transformation is proposed to estimate the projective sizes of vehicles. Furthermore, Contour Size Similarity (CSS) approach is presented to discover vehicles that threaten driving safety. With only one single camera applied, the cost of CSS is far less than that of a stereo vision approach. Furthermore, the search area of the vehicle detection can be narrowed based on results of lane detection, because only the closest preceding car in the lane of the autonomous vehicle is interested. Once the closest car is detected, the approach of vehicle detection starts to compute its range to the camera [70][71]. When another vehicle cuts in, the approach can also shift its detection target immediately.

1.3 Research Objectives and Organization of the Thesis

The objective of this dissertation is to develop advanced vision-based methodologies for driving assistance systems. The developed approaches consist of range and size estimation, error analysis of the estimated results, dynamic camera calibration, lane model, lane detection, the approach of Contour Size Similarity, and vehicle detection. For driving assistance systems,

information concerning the positions of lanes and the preceding vehicles are important. In the study, a camera model is first adopted to estimate the actual and the projective sizes of the detected targets and approaches to reduce detection errors and accelerate detection are also developed. Then, lane positions in the images are extracted by Lane Marking Extraction (*LME*) Finite State Machine (*FSM*) based on information of properties of lane markings. B-spline is also used to reconstruct road boundaries. Afterwards, the approach of contour size similarity is presented to detect vehicles within the driving lane and estimate their range to the camera. The obtained information is applied to driving assistance systems to improve driving safety.

The material in dissertation is organized according to the approaches used in driving assistance systems. A simplified overview is shown in Fig. 1-1. In Chapter 2, the dissertation presents new approaches to estimate the range between the preceding vehicle and the intelligent vehicle, to estimate vehicle size and its projective size, and to dynamically calibrate cameras. A lane model is presented in Chapter 3. For lane detection, a *LME FSM* is designed to extract lane markings with a lane model. Then, the obtained lane boundaries can be applied to determine the search region of vehicle detection. In Chapter 4, the developed fuzzy-based vehicle detection method, Contour Size Similarity (*CSS*), performs the comparison between the projective vehicle sizes and the estimated ones to recognize the target vehicle by fuzzy logic. The target of vehicle detection is the closest preceding car in the same lane with the intelligent vehicle. The experimental results demonstrate that our approaches effectively detect vehicles under different situations.

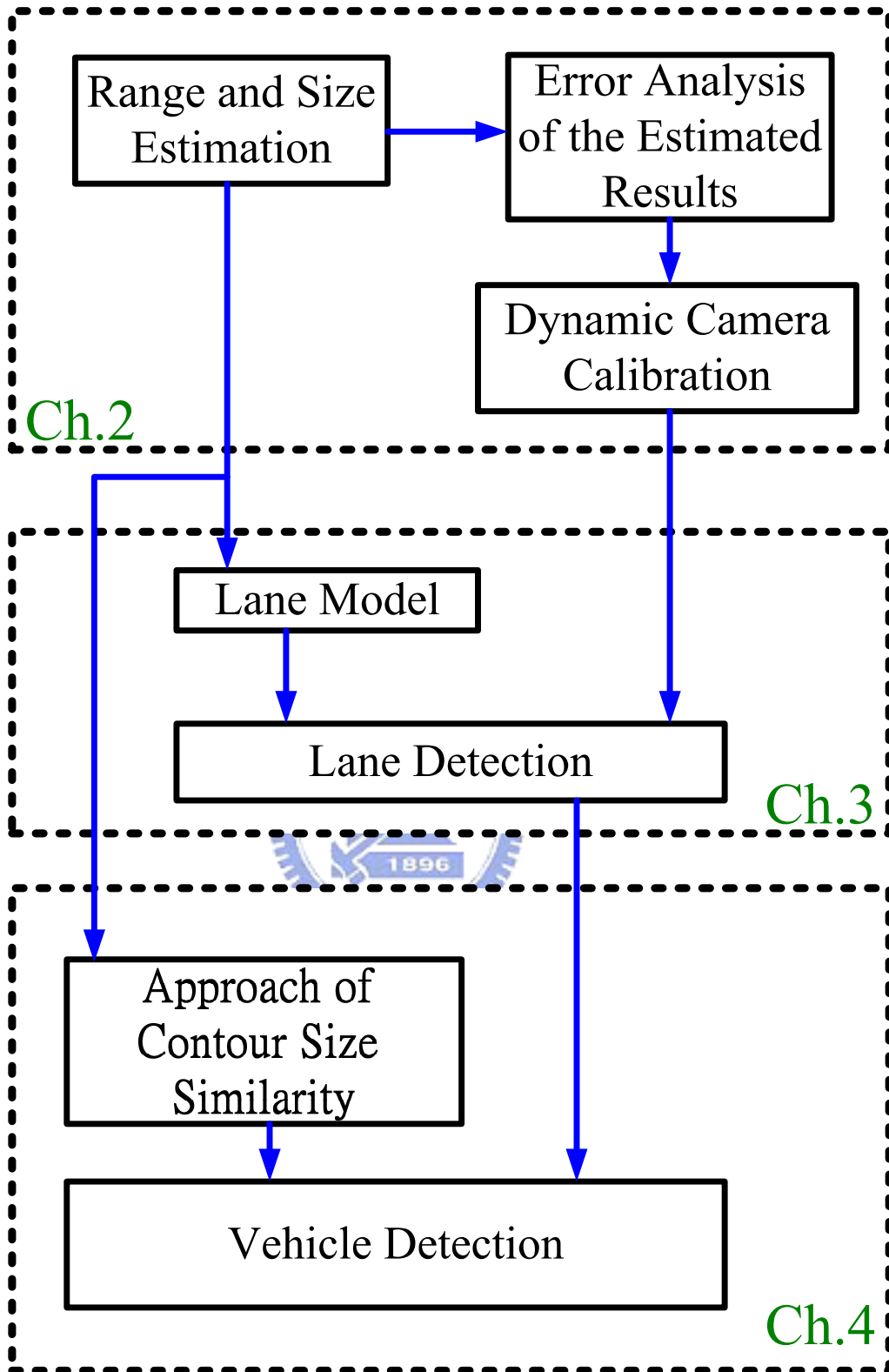


Fig. 1-1. Structure of the thesis.

Chapter 2

Range Estimation and Dynamic Calibration

2.1 Introduction

Accurate and real-time detection of vehicle position, speed and traffic flows are important issues for driving assistance systems and traffic surveillance systems [1][72]-[74]. During the detection, errors often arise because of camera vibration and constraints such as the limitations of image resolution, quantization errors, and lens distortions [34][75]. Therefore, accurate error estimation is important in vehicle detection issues, and image processing techniques for position estimation or motion detection are necessary in many situations [7][76]-[78]. However, most of the previous studies have not involved methods of reducing errors caused by changes of camera parameters, while some important issues like error estimation and the way to set appropriate camera parameters were seldom considered. This may influence the determination of camera parameters and the specifications of a detection system. Therefore, we propose an effective strategy to reduce errors of range estimation by determining the most suitable camera parameters.

In this study, we apply error estimation to determine proper camera parameters and then estimate actual and projective sizes of target objects to facilitate vehicle recognition. An approach to rapidly compute projective sizes is also proposed to significantly reduce the computational cost of vehicle detection process for real-time and embedded systems. Then, a

dynamic calibration approach is presented to calibrate the tilt and swing angles of the camera with information of lane markings and vehicles in the image. The experimental results demonstrate that our work can provide accurate and robust range and size estimation of target vehicles. The rest of this chapter is organized as follows: Section 2.2 presents position and size estimation using projective geometry. Section 2.3 explores range estimation and error estimation with various camera parameters. Section 2.4 proposes a dynamic calibration approach to deal with the problem of camera vibration and variation in camera angle. Section 2.5 displays experimental results of range and height estimation, dynamic calibration of camera angles, and comparisons with other approaches.

2.2 Position and Size estimation using Projective Geometry

The position of any point in the 3-D world coordinates (X, Y, Z) projected to a 2-D image plane (x, y) can be calculated through perspective transformation [13]. Mapping a 3-D scene onto the 2-D image plane is a many-to-one transformation. However, mapping a point on the front horizon of the camera onto an image plane is a one-to-one transformation. Therefore, the relative position between the camera and any point on the ground can be estimated by the coordinate transformation between image plane and ground plane.

2.2.1 Coordinates Transformation Model

Figure 2-1 shows the coordinate transformation between image plane and ground plane, where O_w denotes the origin of the world coordinates (X, Y, Z) , and O represents the origin of the image coordinates (u, v) . Let λ be the focal length of the camera; p denote the lens center; h represent the height. As shown in Fig.2-2(a), there is a cuboid C associated with a target object, whose lengths, widths and heights are L_1 , W_1 , and H_1 , respectively. Let $P_1(X, 0, Z)$ be located on the ground, then $P_2=(X, H_1, Z)$, $P_3=(X + W_1, 0, Z)$, and $P_5=(X, 0, Z+L_1)$, which are

inferred from the size of C . Other vertices can be estimated in the same way. Based on the cuboid's size and the position of its vertex, P_1 , the projective positions of other vertices in a cuboid can be estimated to accurately estimate the contour and size of the cuboid's projection.

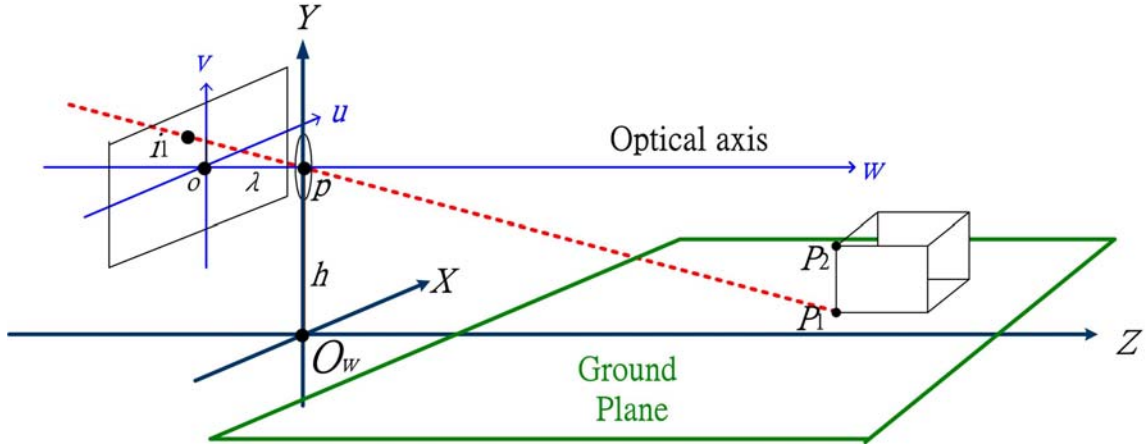
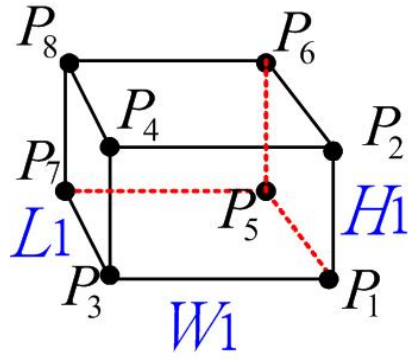


Fig. 2-1. Coordinate transformation between image plane and ground plane.

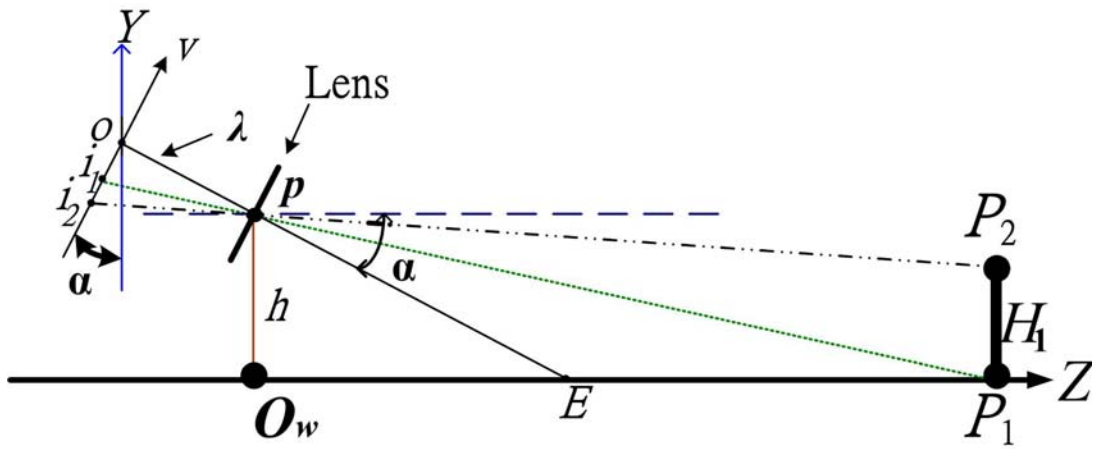
Figure 2-2(b)(c) presents the side view and top view of the image formation. In the figure, tilt angle α denotes the angle between the Z -axis and the optical axis, \overline{pE} . $P_1(X, 0, Z)$ projects onto $i_1(u, v)$ on the image plane, and the transformation between the two coordinates can be expressed as (2.1) and (2.2) by applying trigonometric function properties and our previous study [34], where $\|Z\|$ and $\|X\|$ respectively denote the range and lateral position between P_1 and the camera.

$$Z(v) = h \cdot \tan\left(\left(\frac{\pi}{2} - \alpha\right) - \tan^{-1}\left(\frac{v}{\lambda}\right)\right) \quad (2.1)$$

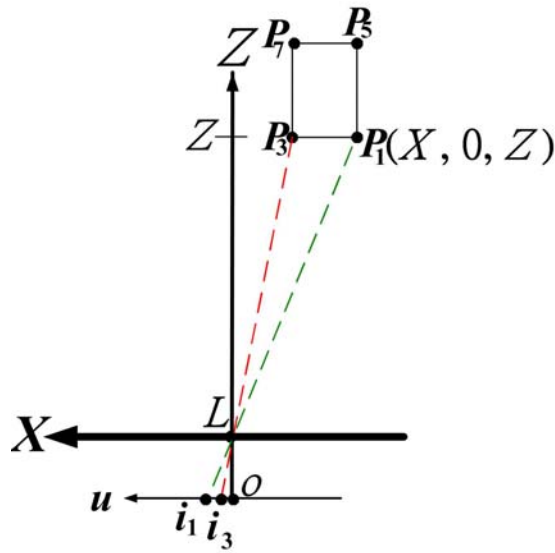
$$X(u, v) = -\frac{u}{\lambda} \times h \cdot \tan\left(\left(\frac{\pi}{2} - \alpha\right) - \tan^{-1}\left(\frac{v}{\lambda}\right)\right) \quad (2.2)$$



(a)



(b)



(c)

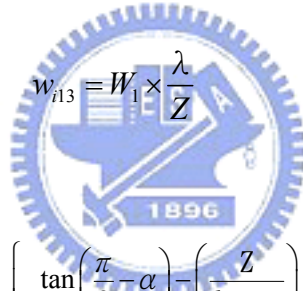
Fig. 2-2. The projective geometry of a camera model. (a) A cuboid C . (b) Side view. (c) Top view.

Let P_2 and P_3 respectively project onto $i_2(u_2, v_2)$ and $i_3(u_3, v_3)$. The $\overline{P_1P_2}$ is the height of cuboid C , whose projective height is h_{i12} in (2.3). The distance between P_1 and P_3 is the width of C ; its projective width is w_{i13} in (2.4).

Based on (2.1)-(2.4), if P_1 of the cuboid can be found in the image, then the position and size of the cuboid can be estimated. Likewise, the relation between v_2 and H_1 can be obtained by (2.3), as shown as (2.5). Further by applying (2.5), we can have the height of the cuboid C as in (2.6).

$$h_{i12} = v - v_2, \quad (2.3)$$

$$\text{where } v(Z) = \lambda \times \tan \left[\left(\frac{\pi}{2} - \alpha \right) - \tan^{-1} \left(\frac{Z}{h} \right) \right], \quad v_2(Z) = \lambda \times \tan \left[\left(\frac{\pi}{2} - \alpha \right) - \tan^{-1} \left(\frac{Z}{h - H_1} \right) \right]$$



$$w_{i13} = W_1 \times \frac{\lambda}{Z} \quad (2.4)$$

$$v_2 = \lambda \cdot \left\{ \frac{\tan \left(\frac{\pi}{2} - \alpha \right) - \left(\frac{Z}{h - H_1} \right)}{1 + \tan \left(\frac{\pi}{2} - \alpha \right) \times \left(\frac{Z}{h - H_1} \right)} \right\} \quad (2.5)$$

$$H_1 = \left(h \cdot \tan \left(\frac{\pi}{2} - \alpha \right) - Z - \frac{v_2 \cdot \left(Z \cdot \tan \left(\frac{\pi}{2} - \alpha \right) - h \right)}{\lambda} \right) \left(\frac{\lambda}{\lambda \cdot \tan \left(\frac{\pi}{2} - \alpha \right) - v_2} \right) \quad (2.6)$$

2.2.2 Rapid Estimation of Projective Height

A cuboid's projective size varies with its relative position with the camera. From (2.3), we can estimate its projective height. When applied to driving assistance, the rapid size estimation of the front vehicle's projection can provide helpful information for vehicle recognition and determination of vehicle size.

$$v(Z) = \lambda \left\{ \frac{h \cdot \tan\left(\frac{\pi}{2} - \alpha\right) - Z}{h + Z \cdot \tan\left(\frac{\pi}{2} - \alpha\right)} \right\} \quad (2.7)$$

From (2.1), we can obtain the relation between Z and v as shown in (2.7). In Fig. 2-2 (b), there is an object whose height is H_1 . Therefore, supposing that $P_1(X, 0, Z)$ projects onto $i_1(u, v)$, we can re-write (2.3) to turn $h_{i12}(v)$ into a linear equation shown in (2.8). Since the camera is mounted on an experimental vehicle for object detection, when α is too large, the farther part of the lane will not appear in the image. Therefore, α is usually between 0-6 degrees. Also, the height of the camera is restricted by the height of the vehicle roof, to be lower than 1.5 meters. Furthermore, the range Z of the preceding vehicle is usually over 10m, and thus we can obtain (2.9) and (2.10). Then, substitute (2.9) and (2.10) into (2.8) to get (2.11). Also, by substituting (2.1) into (2.11), we obtain $h_{i12}(v)$ as shown in (2.12). Equation (2.13) means the first derivative for v to $h_{i12}(v)$. Let $\xi = (\pi/2 - \alpha)$, and $\tau = \tan^{-1}(v/\lambda)$. (2.15), (2.16) and (2.17) derive from (2.13) and (2.14). In this study, let $\alpha < 6^\circ$, so $\xi > 84^\circ$, to get (2.18) and (2.19). Then they are substituted to (2.17) to obtain (2.20) and (2.21). (2.21) shows the first derivative of $h_{i12}(v)$ is a constant. Therefore, the relation between the projective height of $\overline{P_1P_2}$, $h_{i12}(v)$, and the projected v -coordinate of P_1 can be expressed by a linear equation as (2.22).

$$h_{i12}(v) = \lambda \left\{ \frac{h \cdot \tan\left(\frac{\pi}{2} - \alpha\right) - Z}{h + Z \cdot \tan\left(\frac{\pi}{2} - \alpha\right)} - \frac{(h - H_1) \cdot \tan\left(\frac{\pi}{2} - \alpha\right) - Z}{(h - H_1) + Z \cdot \tan\left(\frac{\pi}{2} - \alpha\right)} \right\} \quad (2.8)$$

$$h + Z \cdot \tan\left(\frac{\pi}{2} - \alpha\right) \cong Z \cdot \tan\left(\frac{\pi}{2} - \alpha\right) \quad (2.9)$$

where $h < 1.5$, $\alpha < 6^\circ$, $Z > 10$.

$$(h - H_1) + Z \cdot \tan\left(\frac{\pi}{2} - \alpha\right) \cong Z \cdot \tan\left(\frac{\pi}{2} - \alpha\right) \quad (2.10)$$

where $H_1 < 2$.

$$h_{i12}(v) \cong \frac{H_1 \times \lambda}{Z} \quad (2.11)$$

$$h_{i12}(v) \cong \frac{H_1 \times \lambda}{h \cdot \tan\left(\left(\frac{\pi}{2} - \alpha\right) - \tan^{-1}\left(\frac{v}{\lambda}\right)\right)} \quad (2.12)$$

$$\frac{dh_{i12}(v)}{dv} \cong \frac{H_1 \times \lambda}{h} \times \frac{d \cot\left(\left(\frac{\pi}{2} - \alpha\right) - \tan^{-1}\left(\frac{v}{\lambda}\right)\right)}{dv} \quad (2.13)$$

$$\cot(\xi - \tau) = \frac{1 + \tan(\xi) \times \tan(\tau)}{\tan(\xi) - \tan(\tau)} \quad (2.14)$$

$$\frac{dh_{i12}(v)}{dv} \cong \frac{H_1 \times \lambda}{h} \times \frac{f_{d1} - f_{d2}}{(\tan(\xi) - \tan(\tau))^2} \quad (2.15)$$

where $f_{d1} = (\tan(\xi) - \tan(\tau)) \times \frac{d(1 + \tan(\xi) \times \tan(\tau))}{dv}$,

$$f_{d2} = (1 + \tan(\xi) \times \tan(\tau)) \times \frac{d(\tan(\xi) - \tan(\tau))}{dv}.$$

$$\begin{aligned} \frac{dh_{i12}(v)}{dv} \cong & \\ \frac{H_1 \times \lambda}{h} \times & \frac{\left(\tan(\xi) - \frac{v}{\lambda}\right) \times \frac{d\left(1 + \tan(\xi) \times \frac{v}{\lambda}\right)}{dv} - \left(1 + \tan(\xi) \times \frac{v}{\lambda}\right) \times \frac{d\left(\tan(\xi) - \frac{v}{\lambda}\right)}{dv}}{\left(\tan(\xi) - \frac{v}{\lambda}\right)^2} \end{aligned} \quad (2.16)$$

$$\frac{dh_{i12}(v)}{dv} \cong \frac{H_1 \times \lambda}{h} \times \frac{\left(\tan(\xi) - \frac{v}{\lambda}\right) \times \frac{\tan(\xi)}{\lambda} - \left(1 + \tan(\xi) \times \frac{v}{\lambda}\right) \times \left(-\frac{1}{\lambda}\right)}{\left(\tan(\xi) - \frac{v}{\lambda}\right)^2} \quad (2.17)$$

$$\tan(\xi) \gg \frac{v}{\lambda} \quad (2.18)$$

where $\xi > 84^\circ$.

$$\tan(\xi) \times \frac{\tan(\xi)}{\lambda} \gg \left(\frac{v}{\lambda^2} \times \tan(\xi) + \frac{1}{\lambda} \right) \quad (2.19)$$

$$\frac{dh_{i12}(v)}{dv} \cong \frac{H_1 \times \lambda}{h} \times \frac{\tan(\xi) \times \frac{\tan(\xi)}{\lambda}}{(\tan(\xi))^2} \quad (2.20)$$

$$\frac{dh_{i12}(v)}{dv} \cong \frac{H_1}{h} \quad (2.21)$$

$$h_{i12}(v) \cong \frac{H_1}{h} \times v + C_1 \quad (2.22)$$

where C_1 is a constant.

From the sequential images, we get the actual projective height of $\overline{P_1P_2}$. Let the projective height of $\overline{P_1P_2}$ be $h_{i12}(v_a)$ when P_1 projects onto v_a , and the height be $h_{i12}(v_b)$ when projecting onto v_b . Then, by substituting the obtained $h_{i12}(v_a)$ and $h_{i12}(v_b)$ into (2.22), C_1 and H_1 can be obtained as expressed in (2.23) and (2.24).

$$H_1 \cong \frac{h \cdot [h_{i12}(v_a) - h_{i12}(v_b)]}{(v_a - v_b)} \quad (2.23)$$

$$C_1 \cong h_{i12}(v_a) - \frac{H_1}{h} \times v_a \quad (2.24)$$

By comparing (2.3) and (2.22), we can find that the proposed approach of projective height estimation significantly reduces the computation cost. Also, the comparison between (2.6) and (2.23) shows that the proposed approach requires much less computation timing for estimating the actual height of the target object.

2.3 Range and Error Estimation

Inaccurate camera parameters often cause estimation errors. Even if the parameters are initially set accurately, they could be changed by external forces, or by the use of mechanical devices, causing the estimated value to be different from the real value. The range estimation results are discussed below.

2.3.1 Digitalized Equation of Range Estimation

To estimate range with a single camera, the equation evolved by the camera model should be digitalized first. Therefore, an affine transformation from real image coordinates (u, v) to bitmap image coordinates (M, N) can be obtained by (2.25). Figure 2-3 displays the relationship between the M - N bitmap image coordinates and the u - v real image coordinates, where the left bottom images denotes the origin $Q(0, 0)$.

$$M = -d_x^{-1} \times u + M_m / 2, N = -d_y^{-1} \times v + N_n / 2, \quad (2.25)$$

where d_x and d_y are respectively horizontal and vertical physical distances between adjacent pixels, and the frame size is M_m by N_n pixels.

Table 2-1 Relations between N and Z coordinates

Parameters		Z-coordinate (Meter)					
		$N=0$	$N=100$	$N=200$	$N=300$	$N=400$	$N=492$
$\alpha=0^\circ$	$\lambda=8\text{mm}$	5.715	9.63	30.56	∞	∞	∞
$\alpha=0^\circ$	$\lambda=16\text{mm}$	11.43	19.25	61.11	∞	∞	∞
$\alpha=2^\circ$	$\lambda=8\text{mm}$	4.91	7.61	16.76	∞	∞	∞
$\alpha=2^\circ$	$\lambda=16\text{mm}$	8.71	12.66	23.12	130.82	∞	∞
$\alpha=6^\circ$	$\lambda=16\text{mm}$	5.87	7.48	10.26	16.27	38.66	∞
$\alpha=8^\circ$	$\lambda=16\text{mm}$	5.03	6.19	8.01	11.29	18.94	49.35

The units of N and Z are the numbers of pixels and meters respectively.

Table 2-2 Error analysis of range estimation

Parameters		Error ratio					
		Z=10	Z=20	Z=30	Z=40	Z=50	Z=60
$\alpha=0^\circ$	$\lambda=8\text{mm}$	0.36%	0.72%	1.08%	1.44%	1.82%	2.18%
$\alpha=0^\circ$	$\lambda=16\text{mm}$	—	0.36%	0.54%	0.72%	0.90%	1.08%
$\alpha=2^\circ$	$\lambda=8\text{mm}$	0.36%	0.72%	1.08%	1.44%	1.82%	2.18%
$\alpha=2^\circ$	$\lambda=16\text{mm}$	0.18%	0.36%	0.54%	0.72%	0.90%	1.08%

* “—“ means beyond the field of view.

The relation between N -coordinates and v -coordinates is shown in (2.25). Substitute (2.25) into (2.1), we have the coordinate transformation of Z and N as shown in (2.26), which is the digitalized equation of range estimation.

$$Z = h \cdot \tan \left(\left(\frac{\pi}{2} - \alpha \right) - \tan^{-1} \left(\frac{((N_n / 2) - N) \times d_y}{\lambda} \right) \right) \quad (2.26)$$

The Range Estimation is analyzed as follows. This study utilized a Hitachi KP-F3 camera with a physical pixel size of $7.4(\text{H}) \times 7.4(\text{V}) \mu\text{m}$, that is $d_x = d_y = 7.4 \mu\text{m}$, the number of pixels is 644×493 , and $h=1.3$ meters. In the analyses, with different camera parameters, Table 2-1 shows the mapping relation between the N -coordinate and the Z -coordinate based on (2.26). $N=0$ is mapped to the smallest Z -coordinate in the field of view. The table shows that the smaller Z -coordinate can be included in the field of view when the focal length is smaller or the tilt angle is larger. When $\alpha=0^\circ$, the mapping of $N>246$ is $Z=\infty$. Here ∞ means that the Z -coordinate approaches infinity. Therefore, with a larger α , a smaller Z -coordinate is still in the field of view. The range of the N -coordinate onto which the Z -coordinate is mapped will be relatively larger. For example, the mapping range is $N=[0, 246]$ when $\alpha=0^\circ$, and $N=[0, 492]$ when $\alpha=8^\circ$. So a larger α leads to a compact mapping, thus the estimation errors can be accordingly reduced. However, if α is too large, the mapping range of Z shrinks and distant objects are out of the field of view. When $\alpha=8^\circ$ and $\lambda=16 \text{ mm}$, the Z -coordinate will be $[5.03, 49.35]$ meters in the camera's field of view. Hence, it should make the focal length smaller or $\alpha<8^\circ$, the range of estimation can be larger than 49.35 m.

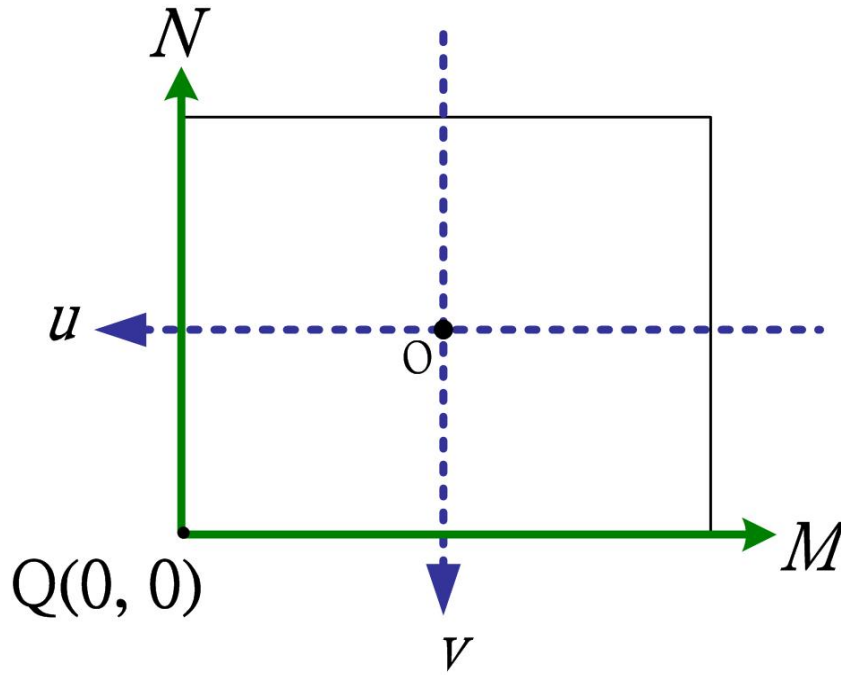


Fig. 2-3. Relation between M - N image coordinates and u - v image coordinates.

2.3.2 Error Estimation

Factors influencing the accuracy of range estimation will be discussed and their impact will be estimated in this section.

2.3.2.1 Quantization errors

Image digitization may causes quantization errors, errors in range estimation are particularly caused by spatial quantization, and are within $\pm \frac{1}{2}$ pixels [79][80]. The results of range estimation are dominated by the projective v -coordinate of P_1 . Therefore, the largest quantization error in mapping to the Z -coordinate can be estimated with the condition that the errors of v are within $\pm \frac{1}{2}$ pixels. Based on (2.26), when $Y=0$, the range of Z should be between the largest range Z_L and the smallest range Z_S as shown in (2.27)(2.28) and e_q the percentage of the largest quantization error is displayed in (2.29).

Table 2-3 Error analysis of range estimation caused by change of tilt angles

Parameters		Error ratio					
		Z=10	Z=20	Z=30	Z=40	Z=50	Z=60
$\alpha=0^\circ$	$\alpha_1=1^\circ$	12.04%	21.25%	28.75%	34.93%	40.17%	44.5%
$\alpha=0^\circ$	$\alpha_1=2^\circ$	21.53%	35.10%	44.71%	51.85%	57.36%	61.73%
$\alpha=2^\circ$	$\alpha_1=3^\circ$	12.04%	21.25%	28.75%	34.93%	40.17%	44.5%
$\alpha=2^\circ$	$\alpha_1=4^\circ$	21.53%	35.10%	44.71%	51.85%	57.36%	61.73%

Table 2-2 displays the largest quantization error in the range $Z=[10, 60]$ m with specific α and λ . As can be seen from Table 2-1, the relation between quantization errors and the N -coordinate can be derived from the relation between Z and N -coordinate. In Table 2-2, the largest quantization error grows with an increasing Z . The larger the focal length of the camera is, the smaller the quantization errors become. The tilt angle of the camera will not influence the largest quantization error according to the analysis results shown in Table 2-2.

$$Z_L = h \cdot \tan \left(\left(\frac{\pi}{2} - \alpha \right) - \tan^{-1} \left(\frac{((N_n/2) - N - 0.5) \times d_y}{\lambda} \right) \right) \quad (2.27)$$

$$Z_S = h \cdot \tan \left(\left(\frac{\pi}{2} - \alpha \right) - \tan^{-1} \left(\frac{((N_n/2) - N + 0.5) \times d_y}{\lambda} \right) \right) \quad (2.28)$$

$$e_q = \frac{\max(|Z - Z_L|, |Z - Z_S|)}{Z} \quad (2.29)$$

2.3.2.2 Influence of changes in translation

The analyses of translation can be divided into the directions of X , Y and Z . The origin of the world coordinates is on the ground below the camera, so the Z -coordinate is the range between the preceding vehicle and the camera. Therefore, the subsection will analyze how the changes of X and Y translation influence the range estimation on the Z -coordinate.

X -translation: in (2.1), the projective position of P_1 onto the v -coordinate determines the Z -coordinate. Figure 2-2(b) shows that the changes of X -translation rarely affect the mapping

position of P_1 onto the v -coordinate. So X -translation seldom influences the accuracy of range estimation.

Y -translation: if the ground is flat, the Y -translation of every point on the ground is zero. When the ground is uneven or when the height of the camera is changed because of vibrations, then the initially determined camera height h may be influenced. Let h denote the initially determined height, and h_2 denote the actual height. According to (2.26), the Z -coordinate mapping result can be obtained by (2.30). If the original height h is adopted, then the error coming from changes of height will be Z_{dh} in (2.31) and the error ratio is e_{rh} in (2.32). Accordingly, errors caused by the Y -translation can be suppressed by increasing the camera height or making the changes of height smaller.

$$Z_{h_2} = h_2 \cdot \tan \left(\left(\frac{\pi}{2} - \alpha \right) - \tan^{-1} \left(\frac{((N_n/2) - N) \times d_y}{\lambda} \right) \right) \quad (2.30)$$

$$Z_{dh} = \left| (h - h_2) \cdot \tan \left(\left(\frac{\pi}{2} - \alpha \right) - \tan^{-1} \left(\frac{((N_n/2) - N) \times d_y}{\lambda} \right) \right) \right| \quad (2.31)$$

$$e_{rh} = \frac{Z_{dh}}{Z_h} = \frac{(h - h_2)}{h} \quad (2.32)$$

2.3.2.3 Influence of changes in camera tilt angles

If vibrations cause the tilt angle of the camera to change from α to α_1 , the result of mapping is computed by (2.33). Therefore, if the original α is applied, the error ratio of range estimation caused by changes of tilt angles is $e_{r\alpha}$ in (2.34).

$$Z_{\alpha_1} = h \cdot \tan \left(\left(\frac{\pi}{2} - \alpha_1 \right) - \tan^{-1} \left(\frac{((N_n/2) - N) \times d_y}{\lambda} \right) \right) \quad (2.33)$$

$$e_{r\alpha} = \frac{|Z_{\alpha_1} - Z|}{Z} \quad (2.34)$$

To estimate errors caused by tilt angle changes of the camera during the range estimation, let h be 1.3 meters, and focal length λ be 8 mini-meters. The analysis of errors is shown in Table 2-3. As depicted in Table 2-3, when both $\alpha=0^\circ$ and $\alpha=2^\circ$ have a variation of 1° , the obtained errors are the same. So the initially set tilt angle does not influence the errors of results. However, errors increase when changes of tilt angle grow larger. The error ratio is about 40% at $Z=50$ meters with a change of 1° on the tilt angle, revealing that changes of angles significantly affect the results of range estimation. With the same camera parameters but the focal length being changed to 16mm, the result will remain unchanged, which demonstrates that the focal length is not related to errors arising from changes of tilt angles. This is because when the focal length varies, the estimated ranges Z and $Z\alpha_1$ will still remain the same, representing that the error ratio will still keep constant.

2.3.2.4 Influence of changes in camera pan angles

Table 2-4 Variation ratio between P_1 and P_3 on the Z -coordinate

θ	Z_d (m)	Variation ratio	
		$Z=30\text{m}$	$Z=40\text{m}$
1°	0.024	0.08%	0.006%
5°	0.122	0.41%	0.31%
10°	0.243	0.81%	0.61%

Figure 2-2(c) shows the condition that the Z -axis parallels the preceding direction of vehicles, denoted by \bar{S} . However, the condition may not be always valid. For example, in Fig. 2-4, the pan angle between \bar{S} and the Z -axis is θ , the variation between P_1 and P_3 on the Z -coordinate is Z_{dp} as expressed in (2.35) and the variation ratio is modeled by (2.36). When the distance between P_1 and P_3 is 1.4m, the related value of Z_{dp} and the variation ratio are shown in Table 2-4. In Table 2-4, the influence turns smaller with a smaller pan angle or a larger range. Even when $\theta=10^\circ$ and the range is 30m, the variation ratio is still less than 1%, which shows that pan angles have little influence on the range estimation.

$$Z_{dp} = W_1 \times \cos \theta \quad (2.35)$$

$$e_{dp} = \frac{Z_{dp}}{Z} \quad (2.36)$$

2.3.2.5 Influence of changes in camera swing angles

The swing angle, i.e. the u - v image plane rotation angle, denotes the angle between the u -axis in the image coordinates and the X -axis in the world coordinates. As shown in Fig. 2-5, let P_1 project onto i_1 and let i_1 be (u, v) on the $u-v$ plane and (u', v') on the $u'-v'$ plane. (u, v) and (u', v') are the coordinates when $\psi \neq 0$ and $\psi=0$, respectively. The transformation of the two coordinates can be computed by (2.37).

$$\begin{bmatrix} u' \\ v' \end{bmatrix} = \begin{bmatrix} \cos \psi & -\sin \psi \\ \sin \psi & \cos \psi \end{bmatrix} \begin{bmatrix} u \\ v \end{bmatrix} \quad (2.37)$$

If $\psi \neq 0$, from (1), we can obtain the results of range estimation by using (2.38).

Table 2-5 shows that the variation between the two coordinates grows with the increasing ψ , u and v . Even if ψ is very small, it still has a great influence when the coordinates are far away from the image center.

$$Z(v) = h \cdot \tan \left(\left(\frac{\pi}{2} - \alpha \right) - \tan^{-1} \left(\frac{-\sin \psi \times u + \cos \psi \times v}{\lambda} \right) \right) \quad (2.38)$$

Table 2-5 Variations between (u, v) and (u', v')

(u, v)	(u', v')	
	$\psi=1^\circ$	$\psi=2^\circ$
(100, 200)	(98.24, 101.73)	(96.45, 103.43)
(200, 200)	(196.48, 203.46)	(192.90, 206.86)

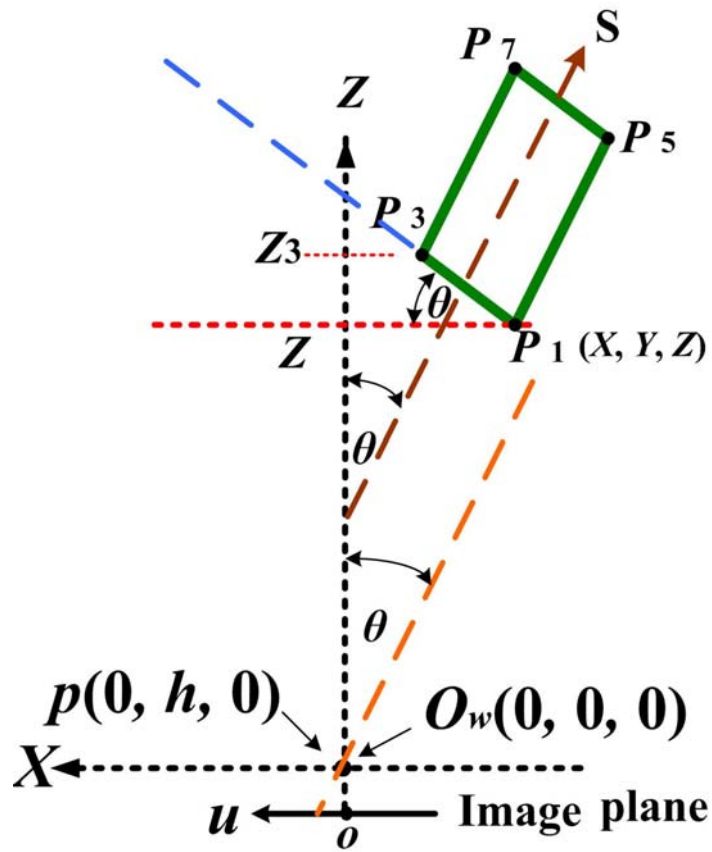


Fig. 2-4 The relation between the Z-axis and the direction of movement of vehicles, denoted by \bar{S} .

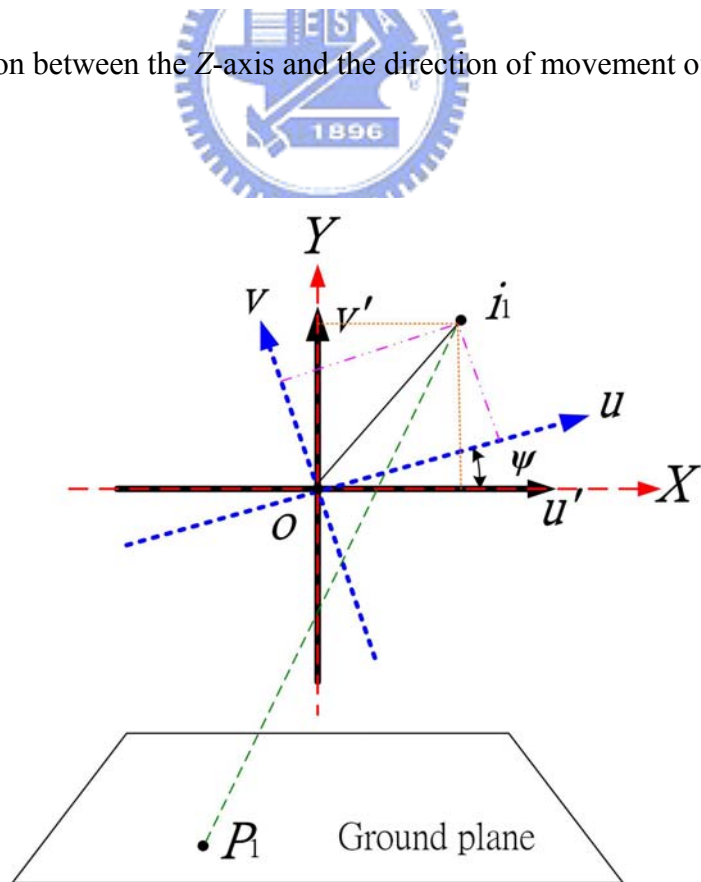
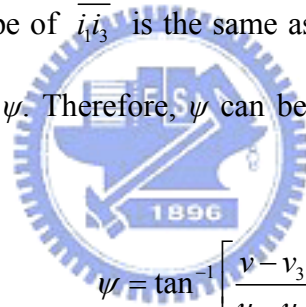


Fig. 2-5. Relation between the Coordinates (u, v) and (u', v')

2.4 Dynamic Calibration Method

Error estimation shows that the variation of camera swing and tilt angles significantly affects the range estimation results. Therefore, an approach is proposed to reduce estimation errors by automatically calibrating camera angles.

The proposed approach can obtain the swing angle ψ by finding a line that is parallel to the X -axis. In Fig. 2-4, when the direction of the camera is the same as the moving direction of the preceding vehicle, the camera's pan angle to the vehicle can be reasonably supposed to be zero. Let contact points between the ground and the two rear wheels of the preceding vehicle be P_1 and P_3 as shown in Fig. 2-2 (a). The world coordinates of the two points have the same Z -coordinate, so $\overline{P_1P_3}$ is parallel to X -axis. In Fig. 2-6, let P_1 and P_3 respectively project onto $i_1(u, v)$ and $i_3(u_3, v_3)$. The slope of $\overline{i_1i_3}$ is the same as u' -axis. Then, the angle between $\overline{i_1i_3}$ and u -axis is the swing angle ψ . Therefore, ψ can be derived from $i_1(u, v)$ and $i_3(u_3, v_3)$ as computed by (2.39).



$$\psi = \tan^{-1} \left[\frac{v - v_3}{u - u_3} \right] \quad (2.39)$$

The analyses in Table 2-4 show that when the swing angle $\psi=0$, even if the camera pan angle $\theta \neq 0$, the Z -coordinates of P_1 and P_3 are still very close and the mapped v -coordinates of the two points are almost the same. So the influence of the pan angle can be neglected and the angle between $\overline{i_1i_3}$ and the u -axis can be regarded as the swing angle ψ as shown in Fig. 2-6.

When the distance between a point on the ground to the camera approaches infinity, its projective point onto the image is named by a vanishing point. When two parallel lines on the ground project to the image coordinates, they tend to converge in a vanishing point. In Fig. 2-6, let the convergent point of the extended driving markings L_1 and L_2 be $p_v(u_v, v_v)$. Then, p_v is a vanishing point. Suppose that the associated world coordinate of p_v be $P_{vw}(X, 0, Z_v)$ whose range to the camera approaches infinity. Based on (2.38), we can compute α by (2.40).

2.5.1 Performance evaluation on range estimation

We conduct experiments to compare the differences between the estimated and measured results concerning the range and size of the experimental objects. The height of experimental target is 1 meter; the parameters of the camera, Hitachi KP-F3, were set to be $\alpha=0^\circ$, $h=1.3\text{m}$ and $\lambda=10\text{mm}$. An image was taken at every meter at the range of 11–60 meters.

In Fig. 2-7, the horizontal axis denotes the range between the experimental target and the camera, while the vertical axis represents the contact points between the experimental target and the ground, P_1 , which projects onto the N -coordinate. ‘Manual’ curve shows the result of manual measurement and ‘Estimated’ is the result of range estimation using (2.26). The two curves approximately match each other, and these results demonstrate that the proposed range estimation approach yields similar results to those of the actual measurements.

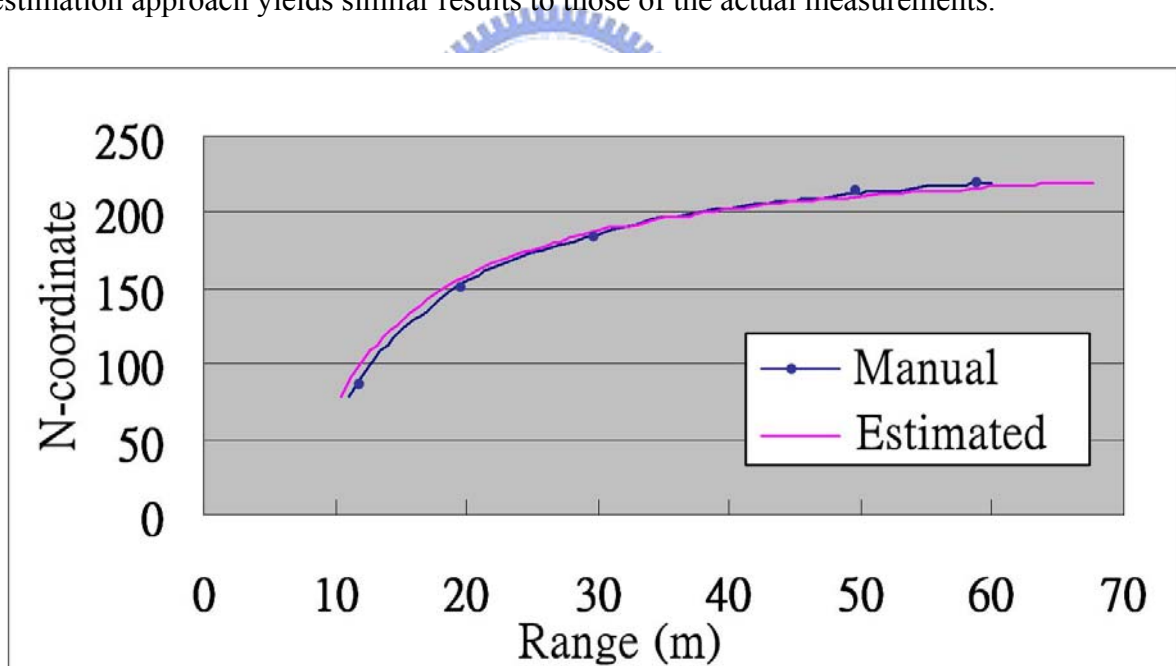


Fig. 2-7. A comparison between the manual range measurement and the estimated range.

In Fig. 2-8, the horizontal axis denotes the contact point, P_1 , which projects onto the N -coordinate, while the vertical axis indicates the projective height of the experimental target. The figure reveals that the results of manual measurement closely match those of the

estimated ones by our proposed method. Figure 2-9 also reveals that the manually measured results and those estimated by our proposed method are quite close. The experimental target is estimated as 0.98 m by our approach to height estimation, which shows a slight error of 0.02 m when compared with the actual height 1 meter. Those results demonstrate that the proposed approach is efficient in the estimation of vehicle heights and can be used to determine the vehicle sizes.

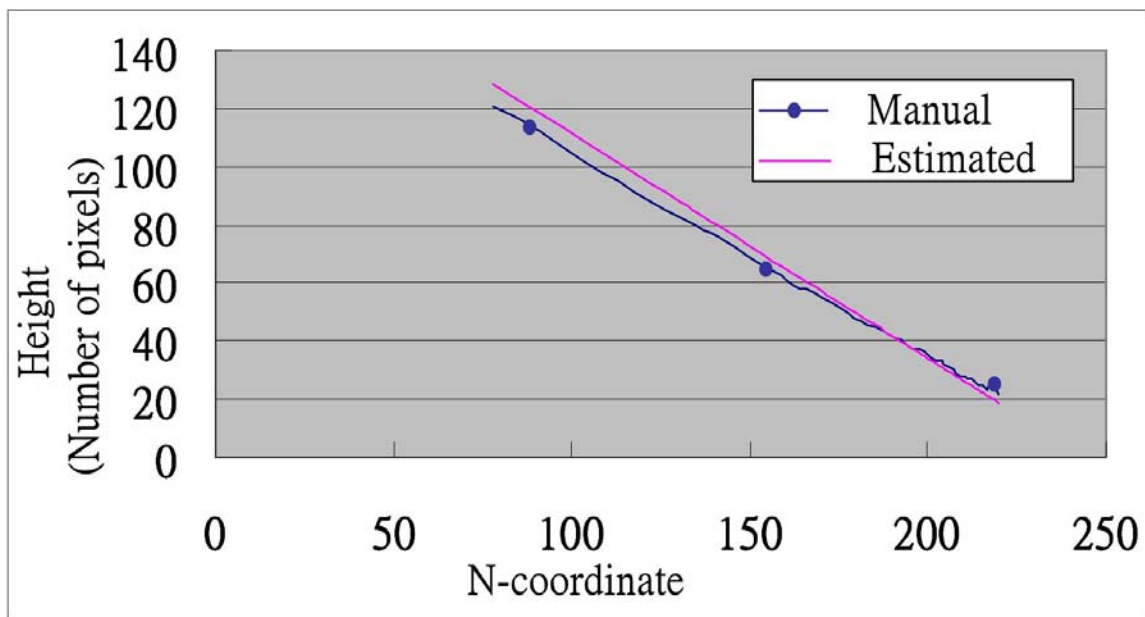


Fig. 2-8. A comparison between the manual height measurement and the estimated height.

Figure 2-9 indicates that the dynamic calibration of angles can improve the accuracy of estimations when the camera angles change. In the experiments, $h=1.32\text{m}$; $\lambda=20\text{mm}$; $\alpha=5^\circ$, $\theta=0^\circ$; $\psi=4.8^\circ$. To capture images of a calibrated target, measurements were taken every 5 meters within a distance of 15–50m. The proposed approach was then applied to estimate the camera’s swing angle based on those images. The estimated average of ψ was 4.71° , and the standard deviation was 0.256° . Compared with the setting of $\psi=4.8^\circ$, the estimation error was about 0.09° . The estimated results and errors of Schoepflin and Dailey’s [14] approach in the same case are compared with ours as shown in Table 2-6, where Schoepflin and Dailey

suppose $\psi=0^\circ$. However, the hypothesis of $\psi=0^\circ$ differs from the actual situation and thus leads to larger errors in tilt angle estimation. In Fig. 2-9, curve ‘A’ shows the difference between manual range measurement and estimated range results using $\alpha=4.70^\circ$ obtained by Schoepflin and Dailey’s approach. The comparison in the ‘B’ curve uses our approach whose computed $\alpha=4.93^\circ$. The comparison between curve ‘A’ and ‘B’ shows that errors of range estimation are significantly suppressed using our approach.

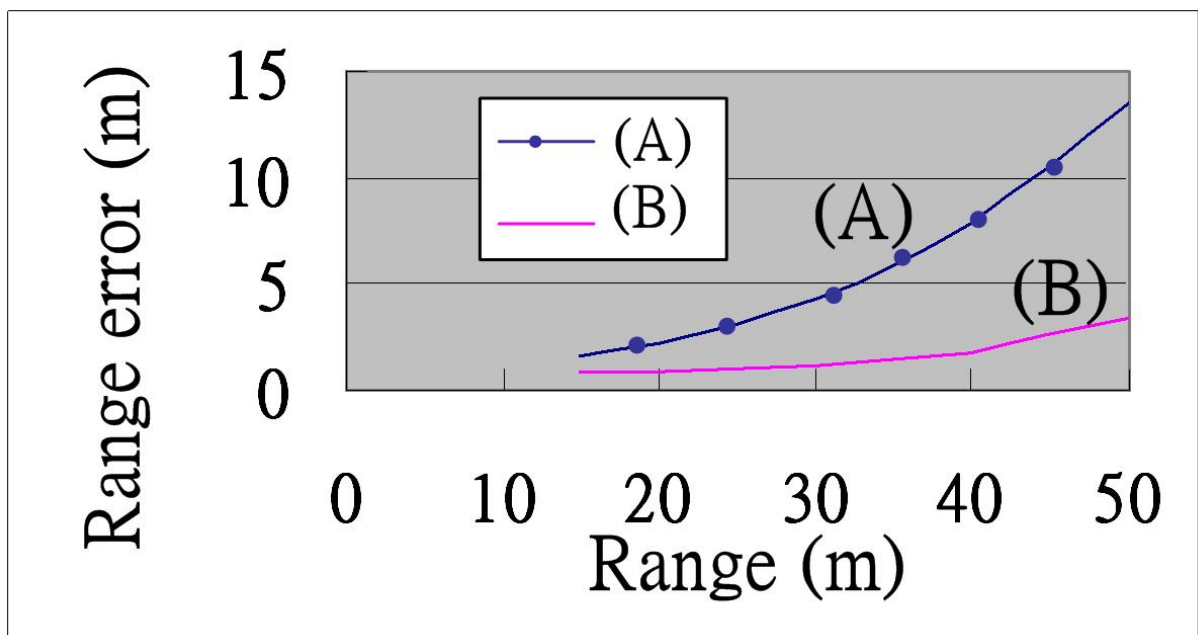


Fig. 2-9. A comparison of estimation results between Schoepflin’s approach and ours.

Table 2-6 Experimental results of camera angle estimation

Approach	estimated ψ , error	Estimate α , error
Schoepflin and Dailey [14]	$0^\circ, 4.8^\circ$	$4.70^\circ, 0.30^\circ$
Our approach	$4.71^\circ, 0.09^\circ$	$4.93^\circ, 0.07^\circ$

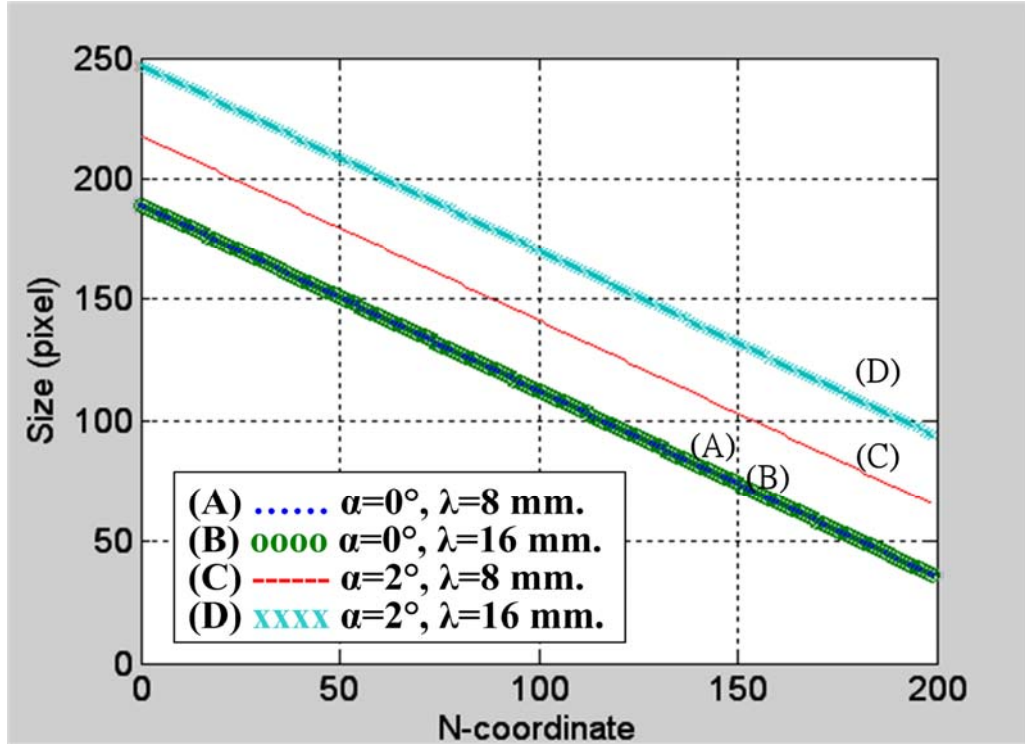


Fig. 2-10. Estimation of a cuboid's projective height.

2.5.2 Simulation Results of Height Estimation

Figure 2-10 depicts the analytical results of the height estimation. We set the camera height $h = 1.3\text{m}$ and the height $\overline{P_1P_2}$ of the target object to be 1m ; as shown in Fig. 2-2(a). Then, as shown in Fig. 2-10, the horizontal axis represents the projective N -coordinate of P_1 and the vertical axis is the projective height of $\overline{P_1P_2}$. Lines (A) and (B) show that if $\alpha = 0^\circ$, the changes in focal length seem not to influence the relationship between the projective N -coordinate of P_1 and the projective height of $\overline{P_1P_2}$. Conversely, Lines (C) and (D) display that if $\alpha \neq 0^\circ$, differences in focal length can change their relationship. In Fig. 2-10, the projective height of $\overline{P_1P_2}$ varies with the projective position of P_1 in the N -coordinate, and their relationship can be approximated by the linear equation, as in (4.5). In Fig. 2-10, the slopes of lines (A) and (B) are the same, -0.769 , while in line (C), it is -0.767 , and line (D) -0.768 . From the proposed approach of fast height estimation in (2.22), the slope H_1/h , can be estimated to be -0.769 ,

which shows that our fast computation model can provide quite accurate estimation results. The computation using (2.3) requires 2 \tan operations, 2 \tan^{-1} operations, 3 division, 2 multiplications, and 5 deductions, however, our approach needs only 1 multiplication and 1 addition, which obviously promotes executive efficiency.

2.5.3 Dynamic calibration of the swing angle

The camera mounted on the experimental vehicle is slightly adjusted to an incline of $\psi=4^\circ$ based on the manual estimation. In the experiments, with the experimental vehicle driving on the road, 500 frames were taken to detect the nearest vehicle in the front driving lane and the contact points between its two rear wheels and the ground. The mean and variance of ψ were estimated to be 3.859° and 0.99° , respectively.

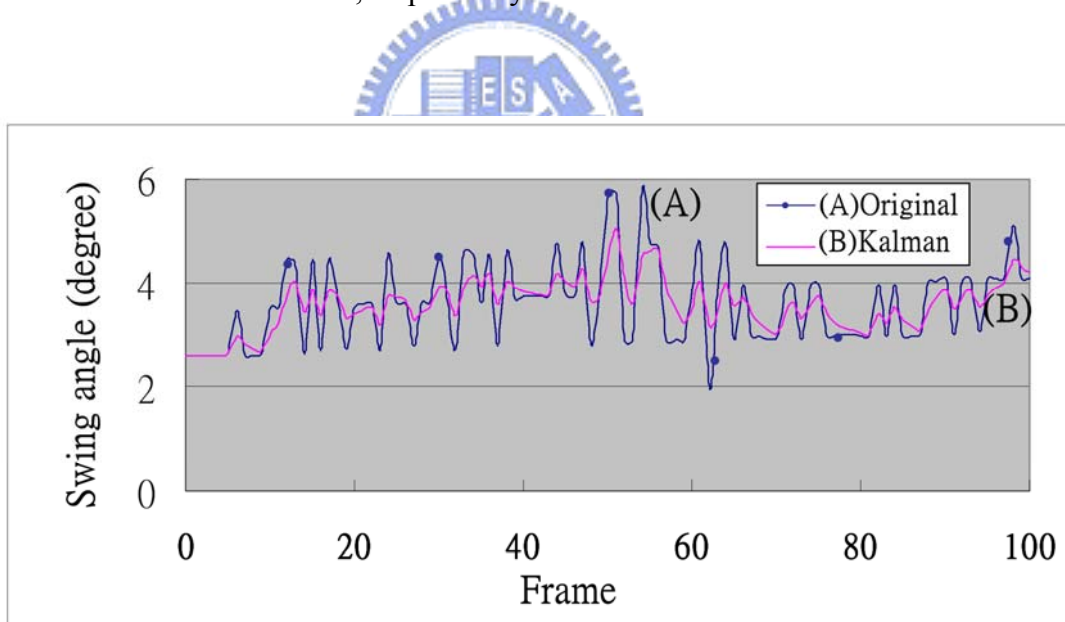


Fig. 2-11. Dynamic calibration of the swing angle.

In this study, we analyze errors caused by image digitalization, algorithmic limitations, lens distortion, the vibration of the experimental vehicle, and the uneven surfaces of the roads. The mean and variance obtained by a tracking process with a Kalman filter were 3.861° and 0.58°

respectively. In Fig. 2-11, the curve “Original” is the value of the swing angle derived by the original algorithm without the tracking process. The curve “Kalman” displays the results of utilizing a Kalman filter to improve the robustness of the estimation results. The experiments confirm that the proposed dynamic calibration approach can efficiently and accurately estimate the camera parameters.

2.5.4 Comparative Performance Evaluation

The proposed approach was compared with the well-known methods shown in Table 2-7 [13][15]. Wang and Tsai [13] utilized a hexagon as the calibration target. However, the hexagon is not available under the moving camera, and needs to be pre-determined in the field of view. Conversely, calibration targets applied in other approaches are objects appearing in general traffic scenes, so require no additional effort on manual setting of the calibration target. The camera angle calibration in the range estimation depends only on the tilt α and the swing angle ψ , so only the access to these two angles were compared. Liang *et al.* [15] assumed that the vanishing point would be in the center of the image, and accordingly estimated an approximate tilt α . Liang *et al.*'s hypothesis is valid only in the conditions that the location of the camera is in the middle of the driving lane and the lane markings are straight lines. However, even when vehicles are driving on an ideal straight lane, it is still not easy to keep them stably in the center of lanes. Figure 2-12(a) and (b) are two cases of comparisons between Liang *et al.*'s and our approach to estimate the tilt angle. Liang *et al.* [15] proposed extending the lane markings to search for the vanishing line V_p (u_v, v_v) and estimating α by V_p . In Fig. 2-12, the convergent point of the u -axis and v -axis is O , the center of the image. L_1 and L_2 respectively represent the extensions of the right and left lane markings, and their convergent point is a vanishing point, V_{p1} . Liang *et al.*'s approach estimated tilt angle by V_{p1} . P_1 and P_3 are the right and left contact points between the

preceding vehicle and the ground. The two points are applied to (2.39) to acquire the swing angle by our methods. The estimated α and estimated errors of camera angles are shown in Table 2-8, where case 1 and case 2 present the situation of Fig. 2-12(a) and Fig. 2-12(b) respectively. The camera setting in Fig. 2-12(a) is $\psi=6^\circ$ and $\alpha=3.5^\circ$, and in Fig. 2-12(b) is $\psi=0^\circ$, $\alpha=2.5^\circ$. As shown in Table 2-8, the estimated results of tilt angle by Liang *et al.*'s approach may have larger errors in these cases. That is because the camera is not at the center of the lane, the swing angle is not correctly estimated, and the lane markings are not straight. Comparatively, in our method, the swing angle can be correctly obtained by (2.39) and then the tilt angle can also be appropriately estimated by (2.42). Therefore, in these cases, our approach can obtain more accurate results without the limitations due to some pre-determined conditions. Among the three approaches in Table 2-7, only Liang *et al.*'s and our approach use calibration targets on the road to achieve dynamic calibration, when the moving camera causes continuously variations of tilt angle α .

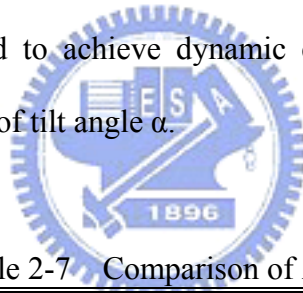
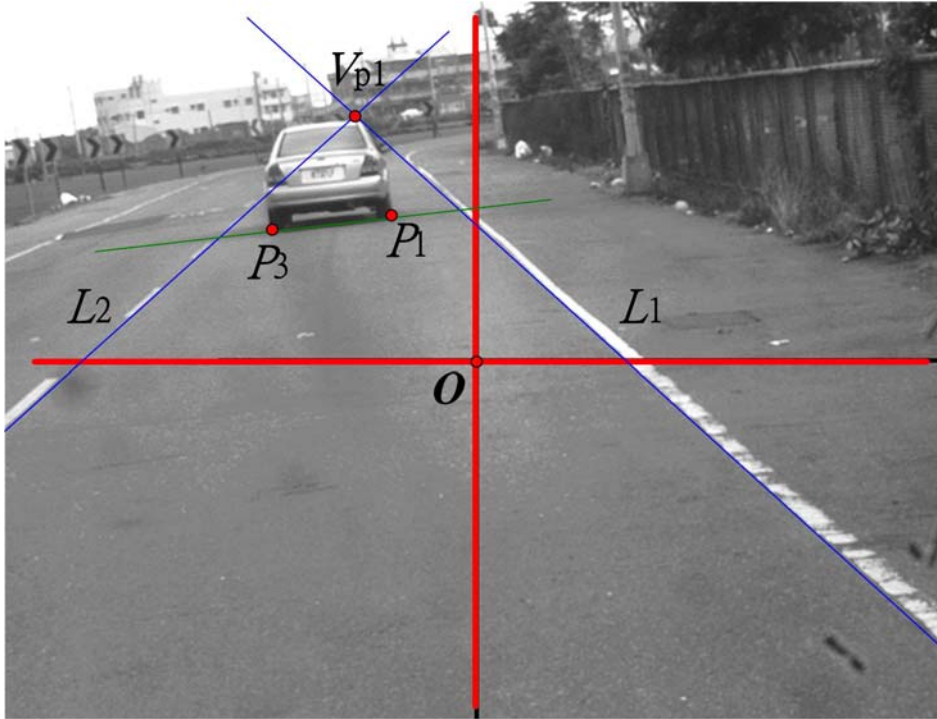


Table 2-7 Comparison of Approaches

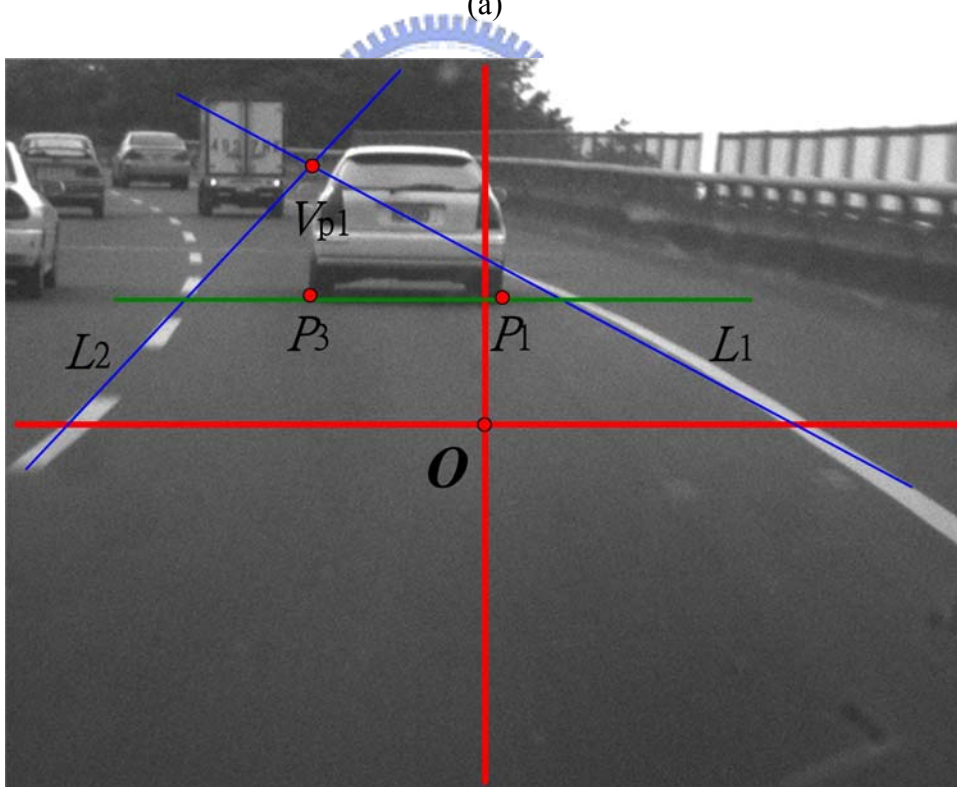
Approach	Calibration Target	Calibration angle	Occasion
Wang and Tsai [13]	Hexagon	ψ, α	Fixed camera
Liang <i>et al.</i> [15]	Lane marking	Approximation of α	Moving camera
Our approach	Lane marking, Vehicle	ψ, α	Moving camera

Table 2-8 A comparison in estimation results of camera angle and errors

Approach	Case 1, $\psi=6^\circ; \alpha=3.5^\circ$		Case 2, $\psi=0^\circ, \alpha=2.5^\circ$	
	α	error	α	error
Liang <i>et al.</i> [15]	0.52°	2.98°	2.81°	0.31°
Our approach	3.51°	0.01°	2.29°	0.21°



(a)



(b)

Fig. 2-12. The swing angle calculated by Liang *et al*'s and our approaches. (a) Straight lane markings. (b) The curve of lane markings.

Chapter 3

Lane Detection

3.1 Introduction

In the driving assistance systems, traffic information can be acquired by sensors to make driving safe and easy [81][82]. For example, vision-based driving assistance systems can determine positions of lanes and obstacles preceding a host vehicle, and the detected information can serve as guidance for driving safety of vehicles [83]-[85]. In the system, the detection of lane is based on image processing techniques to search for the road edges or the lane markings [37][59] and then the lane information is applied to the detection of obstacles in determining obstacle positions [7][33][70]. However, occlusions of obstacles on lane markings may affect results of lane detection [86]. Therefore, lane detection requires not only fast executive speed to achieve real time detection, but also a solution to occlusions.

This dissertation applied geometry transformation and a method of rapid computation of lane width to predict the projective positions and widths of lanes and markings. Then, an approach named *LME FSM* is designed to find lane markings efficiently. A statistical search algorithm is also proposed to correctly and adaptively determine thresholds under various illumination conditions. Furthermore, a dynamic calibration algorithm is presented to update the information of a camera's parameters and lane widths. Besides, a fuzzy logic scheme is adopted to judge the correctness of the detected lane markings and the results are applied to the selection of knots when reconstructing road geometry by B-spline. Finally, the *ROI* determination strategy is proposed to constrain the search region to make the detection more

robust and fast. Therefore, even though obstacles occlude parts of the lane markings, road boundaries still can be reconstructed correctly. Besides, the relative positions between lane markings and cameras can be more precisely estimated with the camera tilt obtained through dynamic calibration.

The rest of this chapter is organized as follows: Section 3.2 presents image analyses using a camera model and the approach of dynamic calibration; Section 3.3 describes the proposed approaches to lane detection, including analyses of lane features, a novel lane marking extraction method adopting a finite state machine, a strategy for determining *ROI*, post processing by fuzzy reasoning, the determination of road boundaries by B-spline curve fitting and overall process of lane detection. Then, the experimental results of the lane detection and analyses are shown in section 3.4.

3.2 Camera model with dynamic calibration

The position of any point in the 3-D world coordinates (X, Y, Z) projected onto a 2-D image plane (u, v) can be obtained through perspective transformation [15]. According to an assumption of a flat ground, mapping a point of the ground plane onto an image plane is a one-to-one transformation. This transformation of the two coordinates can be employed to estimate the distance between the camera and any point on the ground.

3.2.1 Camera Model

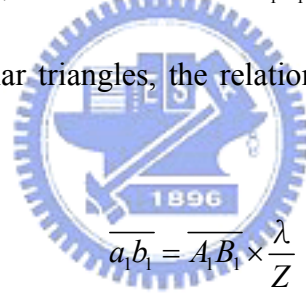
In our previous work [37], a simple camera model was presented to estimate lane projection. In this study, this camera model is extended. Based on this new model, some techniques have been developed. Figure 3-1 shows the projective geometry of a camera model, where O_w denotes the origin of the world coordinates (X, Y, Z) , and O represents the origin of the image coordinates (u, v, w) . Let λ be the focal length of the camera, p the lens center, h the height

between p and O_w , so $(0, h, 0)$ would be the lens center in the world coordinate.

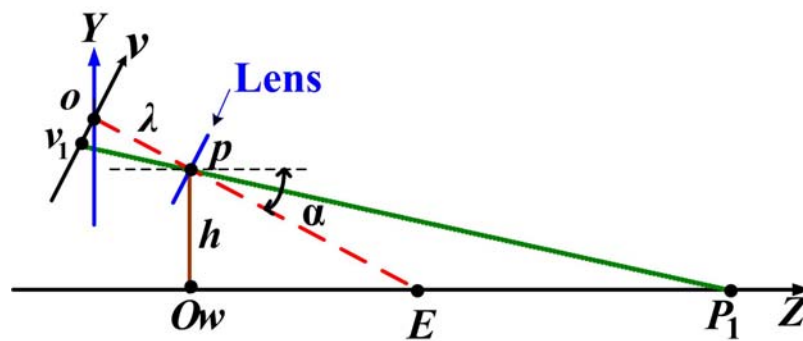
In Fig. 3-1(a), the parameter α is the tilt angle, representing the angle between the Z -axis and the optical axis, \overline{pE} . In Fig. 3-1(a), a point in $P_1(X, 0, Z)$ in the world coordinates is mapped onto $v_1(u, v)$ in the image coordinates. The relation between Z and v is shown as (3.1), and the vertical distance between P_1 and the camera is $\overline{O_w Z}$, where

$$Z = h \cdot \tan \left(\left(\frac{\pi}{2} - \alpha \right) - \tan^{-1} \left(\frac{v}{\lambda} \right) \right) \quad (3.1)$$

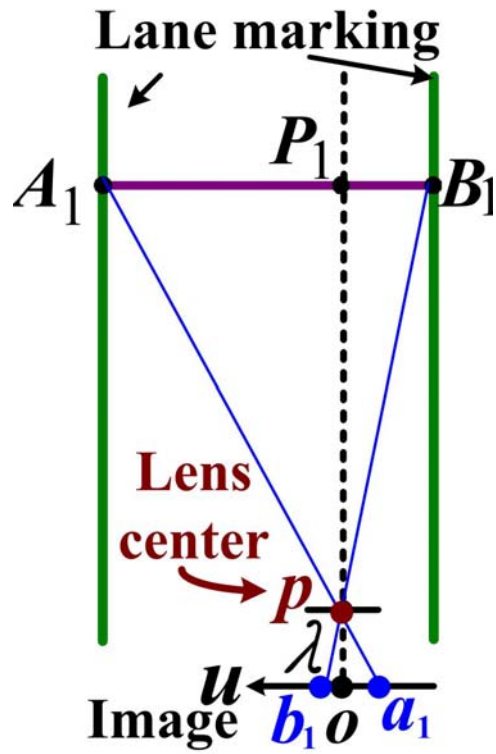
Figure 3-1(b) is a top view of the actual lane. As illustrated, $A_1(X_1, 0, Z)$ is a point on the left lane marking and $B_1(X_2, 0, Z)$ a point on the right one. With the known Z -coordinate obtained from (3.1), the X -coordinate determines where in the u -coordinate A_1 and B_1 are projected onto. In Fig. 3-1 (b), the lane width is $\overline{A_1 B_1}$ and the width of its projection in the image is $\overline{a_1 b_1}$. Based on similar triangles, the relation between $\overline{a_1 b_1}$ and $\overline{A_1 B_1}$ is shown as (3.2).



$$\overline{a_1 b_1} = \overline{A_1 B_1} \times \frac{\lambda}{Z} \quad (3.2)$$



(a)



(b)

Fig. 3-1. The projective geometry of a camera model. (a) The mapping of the Y and Z coordinates on the v -coordinate; (b) The mapping of the X and Z coordinates on the u -coordinate.

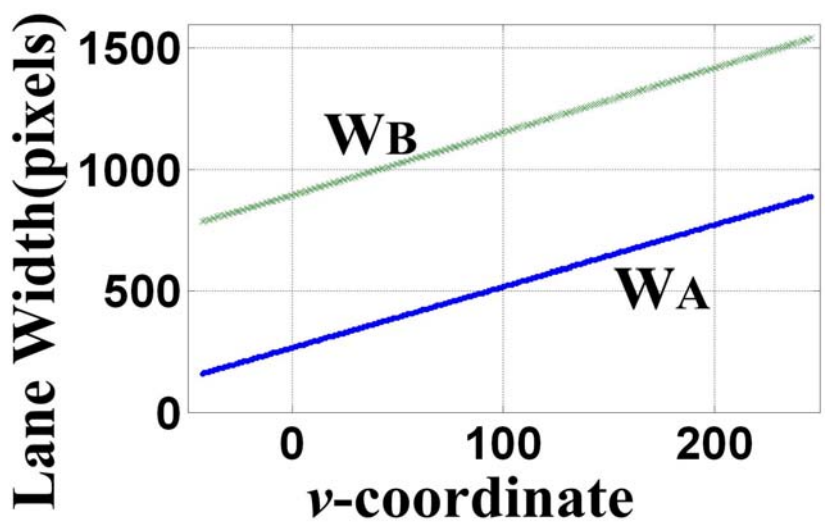
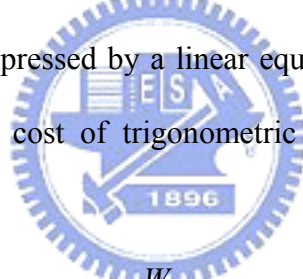


Fig. 3-2. Relation between $w_L(v)$ and the v -coordinate.

According to (3.1) and (3.2), the projective lane width can be appropriately predicted and can be applied to the following lane detection process. Similarly, the projective width of lane markings can also be correctly estimated.

3.2.2 Rapid Estimation of the Projective Width

With the known lane width on the world coordinate, the corresponding projective width of the lane can be computed by (3.1) and (3.2). However, the computation of trigonometric functions is time-consuming. In the study, an approach for rapid estimation of projective lane width is proposed, in which W_{WL} represents the width of a lane in the world coordinates, and its associated width of lane projection in the v -coordinate is $w_L(v)$. The relation between $w_L(v)$ and the v -coordinate can be expressed by a linear equation as shown in (3.3). The approach can suppress the computation cost of trigonometric functions. The proof is presented in appendix A.



$$w_L(v) \cong \left(\frac{W_{WL}}{h}\right) \times v + c \quad (3.3)$$

where c is a translation.

In Fig. 3-2, take the internal parameters of the Hitachi KP-F3 camera for example. The relation between $w_L(v)$ and the v -coordinate is computed by (3.2) and (3.3). The physical pixel size is $7.4\mu\text{m(H)} \times 7.4\mu\text{m(V)}$; and focal length $\lambda=15\text{mm}$. The height h is 1.32m , and the lane width is set to be 3.3m . The horizontal axis represents the v -coordinate of the lane projection, while the vertical stands for the projective width. Line (W_A) shows the estimation result of projective lane width when $\alpha=3^\circ$, and Line(W_B) demonstrates the result when $\alpha=10^\circ$. As shown in the Fig. 3-2, with a fixed parameter of the camera, the relation between $w_L(v)$ and

the v -coordinate is linear. To estimate c in (3.3), let the projective lane width be w_1 , when it is projected onto v_1 . w_1 is obtained from the computation of (3.1) and (3.2). Substitute v_1 and w_1 for v and $w_L(v)$ in (3.3) respectively, and c derives from (3.4). Therefore, the relation between w_L and the v -coordinate can be depicted in (3.5). Take two points on the line from the slope in Fig. 3-2, and the slope is computed as 2.51. Compared with the slope $W_{wL}/h=2.5$ in (3.3), these two results are very similar. Therefore, the calculation of (3.2) and (3.3) can be replaced with the approach of rapid computation of the width to reduce computation cost.

$$c = w_1 - \left(\frac{W_{wL}}{h}\right) \times v_1 \quad (3.4)$$

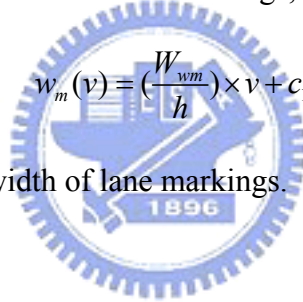
$$w_L = \left(\frac{W_{wL}}{h}\right) \times v + w_1 - \left(\frac{W_{wL}}{h}\right) \times v_1 \quad (3.5)$$

Likewise, the projective width of the lane markings, w_m , can be shown by (3.6).

$$w_m(v) = \left(\frac{W_{wm}}{h}\right) \times v + c_1 \quad (3.6)$$

where W_{wm} denotes the actual width of lane markings.

c_1 : a translation.



3.2.3 Dynamic Calibration

In computing lane width with coordinate transformation, if the tilt angle of the camera is not accurate, huge errors may arise [34]. However, even though the preset tilt angle of the camera is known, there are still some errors because of the road bumps and vibration of moving vehicles. In this paper, an accurate tilt angle and actual lane width can be obtained by using the extracted lane markings in each frame.

1) *Calibration of the tilt angle of camera:* In the study, lane markings are supposed to be two parallel lines, and thus their intersection Z_i would be at infinity. In the image, the intersection of the extension of the two lane markings is the vanishing point $V_P(u_{vp}, v_{vp})$,

which mappings onto Z_i . According to (3.1), the relation of α , Z_i and v_{vp} is shown as (3.7). Substitute (3.8) into (3.7), and α is shown as (3.9). Therefore, α can be obtained through V_P . Furthermore, let the four points of the Z -coordinate $=Z_{N1}$, and Z_{N2} on the left and right lane markings, i.e. Q_{L1} , Q_{L2} , Q_{R1} , Q_{R2} respectively mapping onto P_{L1} , P_{L2} , P_{R1} , and P_{R2} in the image plane. As shown in Fig. 3-3, suppose that the lane width is fixed, $\overline{Q_{L1}Q_{R1}} = \overline{Q_{L2}Q_{R2}}$, and the area enclosed by the closed area formed by the four points will be a parallelogram in the world coordinate. Extend $\overline{P_{L1}P_{L2}}$ and $\overline{P_{R1}P_{R2}}$, and the intersection of them is also a vanishing point, V_P . Then, v_{vp} derives from (3.10). In the study, V_P is determined this way to avoid the wrong calculation caused by the blur or occlusion in the farther part of the lane marking.

$$\alpha = \frac{\pi}{2} - \tan^{-1}\left(\frac{v_{vp}}{\lambda}\right) - \tan^{-1}\left(\frac{Z_i}{h}\right) \quad (3.7)$$

$$\lim_{Z_i \rightarrow \infty} \tan^{-1}\left(\frac{Z_i}{h}\right) = \frac{\pi}{2} \quad (3.8)$$

$$\alpha = -\tan^{-1}\left(\frac{v_{vp}}{\lambda}\right) \quad (3.9)$$

$$v_{vp} = \frac{f_2}{f_1}, \quad (3.10)$$

where $f_1 = \frac{v_{R1} - v_{R2}}{u_{R1} - u_{R2}} - \frac{v_{L1} - v_{L2}}{u_{L1} - u_{L2}},$

$$f_2 = \left(\frac{u_{L1}v_{L2} - v_{L1}u_{L2}}{u_{L1} - u_{L2}}\right)\left(\frac{v_{R1} - v_{R2}}{u_{R1} - u_{R2}}\right) - \left(\frac{v_{L1} - v_{L2}}{u_{L1} - u_{L2}}\right)\left(\frac{u_{R1}v_{R2} - v_{R1}u_{R2}}{u_{R1} - u_{R2}}\right),$$

the coordinates of P_{L1} , P_{L2} , P_{R1} , and P_{R2} are respectively (u_{L1}, v_{L1}) , (u_{L2}, v_{L2}) , (u_{R1}, v_{R1}) , and (u_{R2}, v_{R2}) .

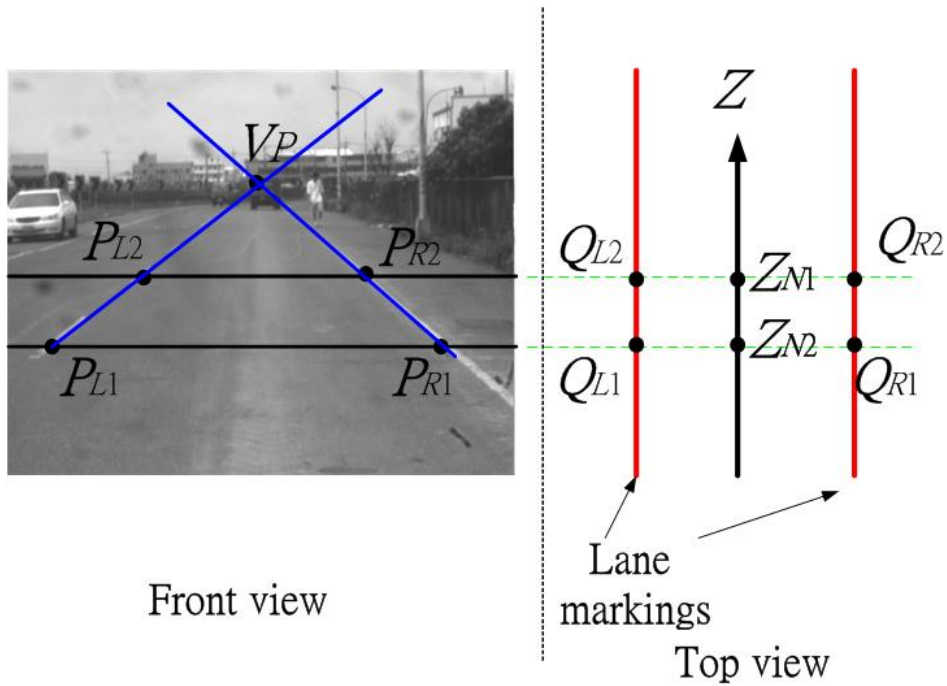
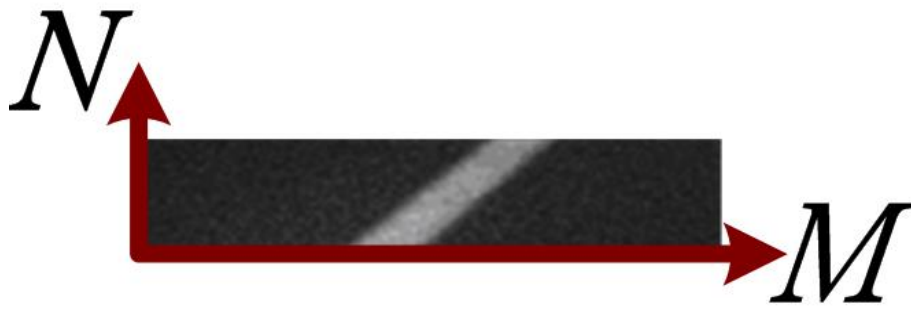
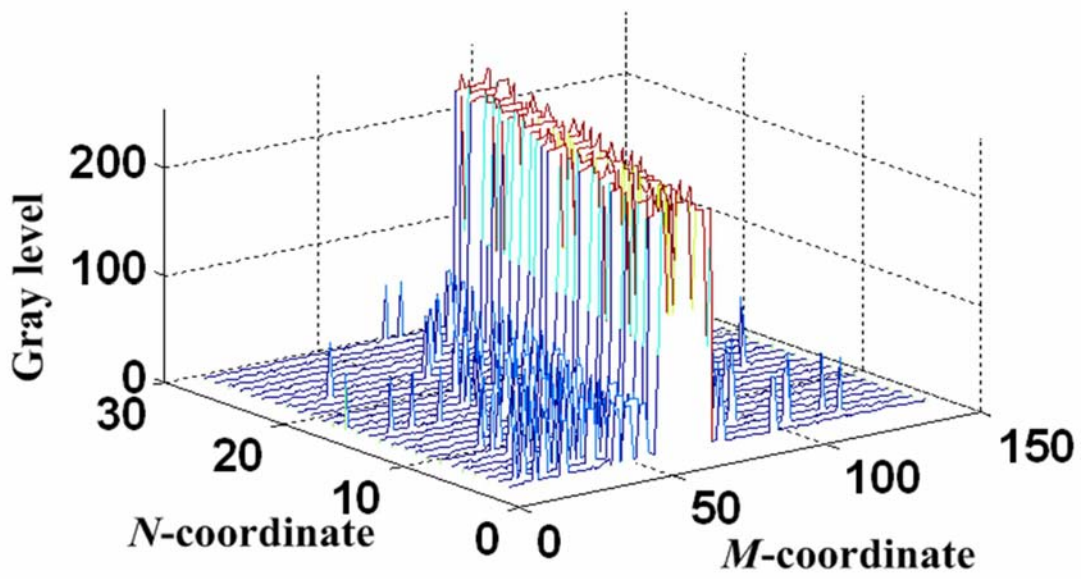


Fig. 3-3. The estimated vanishing point.

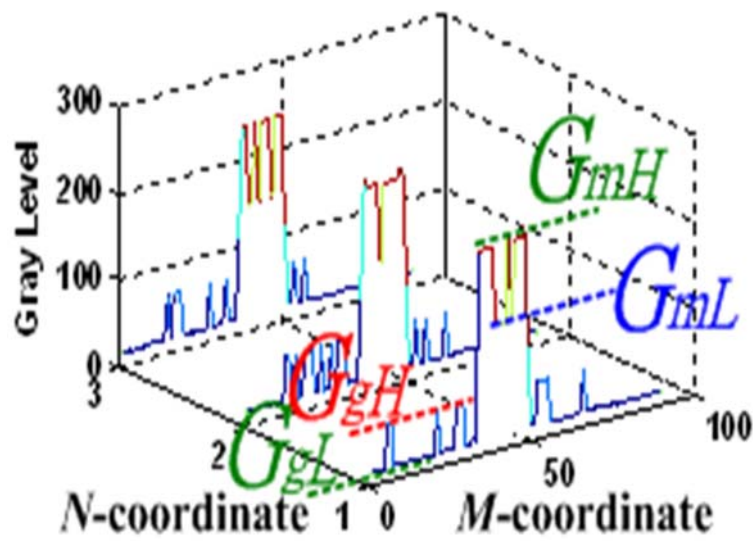
2) *Lane width refinement*: According to the coordinates of P_{L1} and P_{R1} , the associated projective lane width is $|u_{R1} - u_{L1}|$, when projected onto the row at v_{L1} . Substitute $|u_{R1} - u_{L1}|$, and v_{L1} into (3.1) and (3.2), and then the lane width in the world coordinates, $\overline{A_1 B_1}$, can be estimated. It shows that the lane width can be obtained depending on the detected lane markings. Likewise, the actual width of lane markings can be acquired by applying the width of detected lane markings. Thus, those widths can be accurately gained even when they vary with changes of the environment.



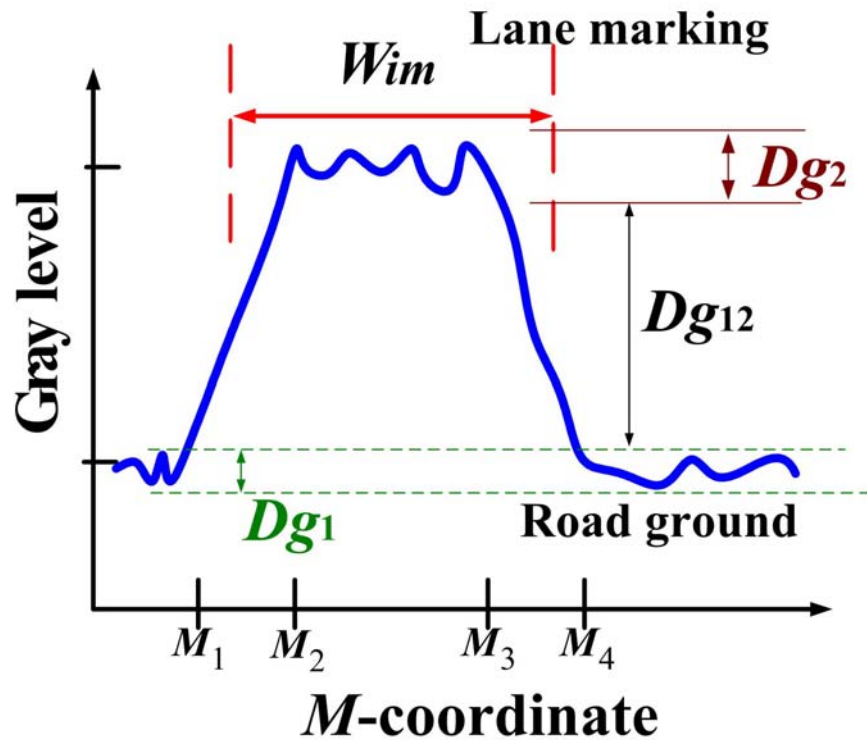
(a)



(b)



(c)



(d)

Fig. 3-4. Lane Marking Model on a road with lane markings. (a) Actual lane marking image; (b) The gray level distribution of (a); (c) The gray level distribution of lane markings in the image coordinates; (d) The variance of gray level in a row of lane marking.

3.3 Lane Detection

Both sides of road markings are supposed to be parallel on the ground plane and their widths are assumed to stay stable or have very slight changes. An approach of extracting lane markings based on a lane model is presented in this section.

3.3.1 Model of Lane Markings

Lane markings usually appear as white, yellow, or red curves and lines. Their intensity in the image is usually higher than that of the ground because they reflect more brightness than road colors. Fig. 3-4 is the analysis of a lane marking model. Fig. 3-4(a) shows a segment of

one lane marking. The M -coordinate and the N -coordinate respectively denote the horizontal and vertical coordinates. Fig. 3-4(b) is the gray level distribution of the pixels in Fig. 3-4(a). In these figures, it can be observed that the gray level of the lane marking is much higher than that of the ground. Fig. 3-4(c) shows both the gray level ranges of lane markings and ground in the image coordinates. As can be seen, G_{mH} and G_{mL} respectively denote the lane marking's largest and smallest gray levels, while G_{gH} and G_{gL} respectively represent the largest and smallest of the ground's gray levels. Fig. 3-4(d) shows the gradient model of the gray level in each row of the lane marking, where D_{g1} is the range of ground's gray level. D_{g2} is the range of lane markings' gray level. D_{g12} is the difference between G_{mL} and G_{gH} . A statistical search algorithm is proposed to adaptively determine D_{g1} , D_{g2} , and D_{g12} . They are adaptively adjusted under various illumination conditions. D_{g1} , D_{g2} , and D_{g12} can be determined by (3.11), and the detail explanation is given in Appendix B. The zone between M_1 and M_2 is the left border of the lane named BS with an upward trend of the gray level, while the zone between M_3 and M_4 is the right border called BT whose gray levels decline. These features of lane markings are called Bright Feature Transition (BFT). The distance between BS and BT represents the length of BFT , and is named by B_L . A lane marking can be reconstructed by searching BFT row by row and connecting BFT s in each row.

$$D_{g1}=G_{gH}-G_{gL} \quad ; \quad D_{g2}=G_{mH}-G_{mL} \quad ; \quad D_{g12}=G_{mL}-G_{gH} \quad (3.11)$$

3.3.2 Lane Marking Extraction

In the image, the BFT approximates to the width of the lane markings and is possibly part of the lane markings. In this subsection, a LME FSM is proposed to extract BFT similar to the lane marking width in the images. First, set a BFT detector in each row of the image, which contains two detection points, P_A and P_B . The distance between these two points is d_m , shown

in (3.12). When this *BFT* detector moves from the left to the right, the difference of the gray levels between P_A and P_B , named $G_d(P_A, P_B)$, will be updated with respect to the detector's move to the right. When the *BFT* detector moves one pixel rightward, $G_d(P_A, P_B)$ is accordingly updated and served as a new input signal of the *LME FSM*. If bright features are found within the current range of the *BFT* detector where P_A and P_B are moving, the input of $G_d(P_A, P_B)$ would accordingly transfer the state of *LME FSM* from state 0 to state 5. Therefore, bright features in every row can be detected according to the transitions of the processing state. If its B_L approximates to the computed width of the lane marking w_m obtained from (3.6), then the likelihood of its being an actual lane marking is high.

$$d_m(N) = \frac{1}{2} \times w_m(N) \quad (3.12)$$

where $w_m(N)$ denotes the projective width of the lane marking in the N -coordinate. $d_m(N)$ represents the distance between P_A and P_B in the N -th row. The distance is set to be half of the estimated width of the lane marking w_m in the same row. When *BFT* detector is applied to detect lane markings, the associated change of $G_d(P_A, P_B)$ passing the lane markings can be shown as Fig. 3-5.

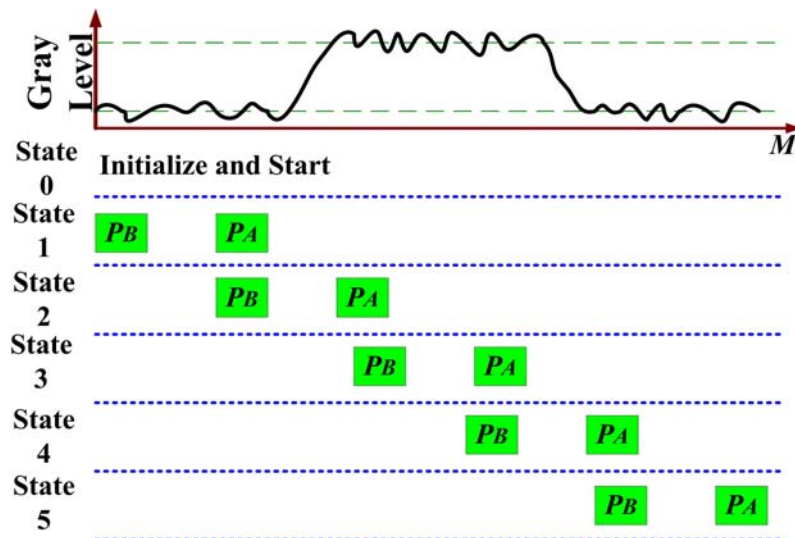


Fig. 3-5. The lane marking's relative positions to P_A and P_B in different states.

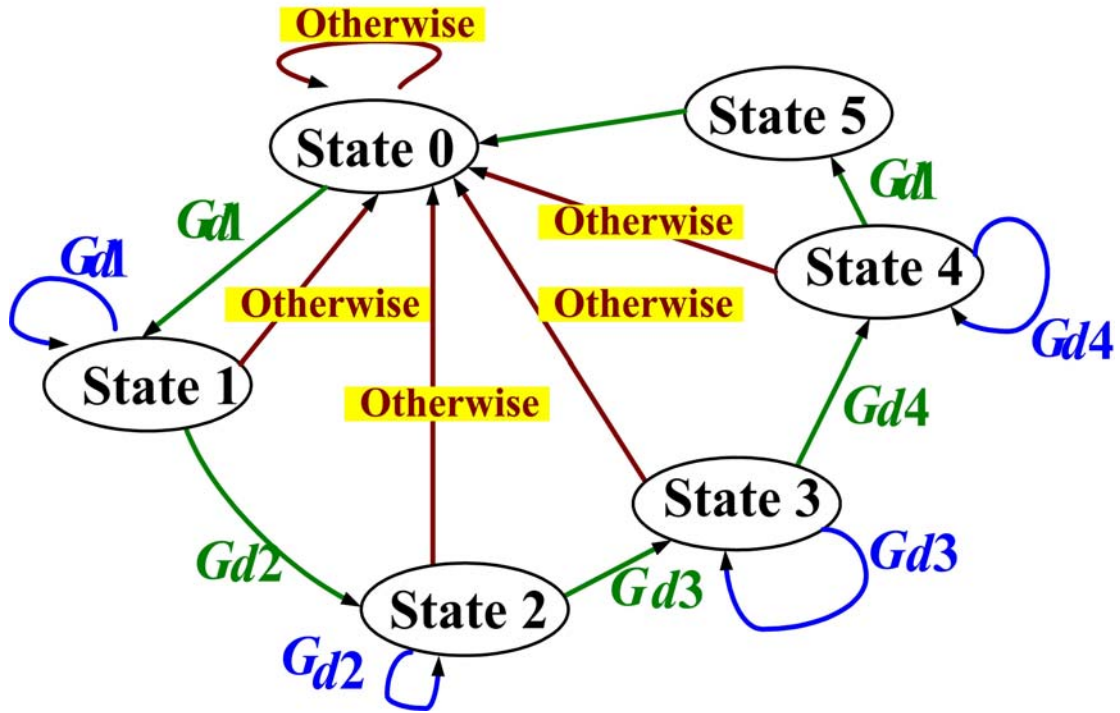


Fig. 3-6. State diagram of *LME FSM*.

In Fig. 3-5, when lane markings appear in the image, the range of $G_d(P_A, P_B)$ will change by five states, associated with *BFT* detector shifting rightward across a lane marking. In State 1, the interval where the detector is located is a lowland zone. In State 2, the part where the detector lies in is an uphill zone. In State 3, the section with the detector is a plateau zone. In State 4, the detector is in a downhill zone. In State 5, the detector comes back to the lowland zone. Table 3-1 shows the range of predictive G_d in those states. If $G_d(P_A, P_B) = G_{d1}$, $G_d(P_A, P_B)$ can match the G_d condition $|G_d| < D_{g1}$. Likewise, the G_d condition of G_{d2} , G_{d3} , and G_{d4} can be obtained from Table 3-1 in the same way. Figure 3-6 is the State Diagram. The transitional operations of the five states are described as follows.

In State 0, *LME FSM* is in the initial state, and no bright feature has been detected yet in this state. When $G_d(P_A, P_B)$ satisfies the condition G_{d1} , *BFT* is possibly within the search region and *FSM* moves into State 1.

In State 1, the *BFT* detector lies in the lowland zone. If $G_d(P_A, P_B)$ still meets G_{d1} , then the

next state will still be State 1; if $G_d(P_A, P_B)$ satisfies G_{d2} , FSM will move into State 2. Otherwise FSM goes back to State 0.

In State 2, the BFT detector is located in the uphill zone. If $G_d(P_A, P_B)$ meets G_{d2} , the next state will still be State 2; if $G_d(P_A, P_B)$ meets G_{d3} , FSM will move into State 3. Otherwise FSM goes back to State 0. As soon as FSM enters State 2, P_A may shift to the region between M_1 and M_2 as in Fig. 3-4(d), the left border between the lane marking and the gray ground. In this condition, the gray level of P_A would be larger than that of P_B .

In State 3, the BFT detector is in the plateau zone. if $G_d(P_A, P_B)$ meets G_{d3} , the next state is still State 3; if $G_d(P_A, P_B)$ meets G_{d4} , FSM will move into State 4. Otherwise, FSM goes back to State 0. When FSM enters State 3, the BFT detector may have already shifted to the range between M_2 and M_3 as in Fig. 3-4(d). Now the gray level of P_A is similar to that of P_B .

In State 4, the BFT detector is situated in the downhill zone. if $G_d(P_A, P_B)$ meets G_{d4} , next state is State 4; if $G_d(P_A, P_B)$ meets G_{d1} , FSM moves into State 5. Otherwise FSM goes back to State 0. When FSM moves into State 4, P_A may have shifted to the zone between M_3 and M_4 as in Fig. 3-4(d), the right border between the lane marking and the road ground. Then the gray level of P_A is smaller than that of P_B .

In State 5, the BFT detector returns to the lowland zone. If FSM enters State 5, that means BFT has been detected and FSM will go back to State 0 to find the next BFT .

$LME FSM$ is efficient in detecting BFT and computing B_L . It is also suitable for hardware implementation.

Table 3-1 Denotations of the five G_d conditions

State	Denotations in different G_d Conditions	G_d Conditions
State 1	G_{d1}	$ G_d < D_{g1}$
State 2	G_{d2}	$G_d > D_{g12}$
State 3	G_{d3}	$ G_d < D_{g2}$
State 4	G_{d4}	$-G_d > D_{g12}$
State 5	G_{d1}	$ G_d < D_{g1}$

3.3.3 ROI Determination Strategy

In this subsection, two properties of changes about positions of lane boundaries are introduced. 1). Longitudinal consistency property: From the nearby position to the farther position, lane markings appear to be lines or curves which are either continuous or dashed. Therefore, by observing the positions of the closer lane markings, the possible positions of the farther parts can be accordingly predicted. 2). Lateral consistency property: Vehicles often move in the middle of the lane, so lateral changes of a lane marking's position are usually slight in the sequential road-scene images. Thus, the possible position of the lane marking in the next frame can be predicted according to that of the current one. The predictive area of the lane marking is the Region of Interest (*ROI*), also the search area of *BFT*. If the *ROI* is too large, the computation cost would increase and the *ROI* may be stained by noise. On the other hand, if the *ROI* is too small, the actual position of the lane marking may not be appropriately covered. Therefore, the *ROI* should be the smallest area which can still include the area of the lane markings. Strategies for determining the *ROI* and three determination approaches to the *ROI* are presented in the subsection. Choosing the best strategy for the associated case is an effective way to reduce errors and computation costs.

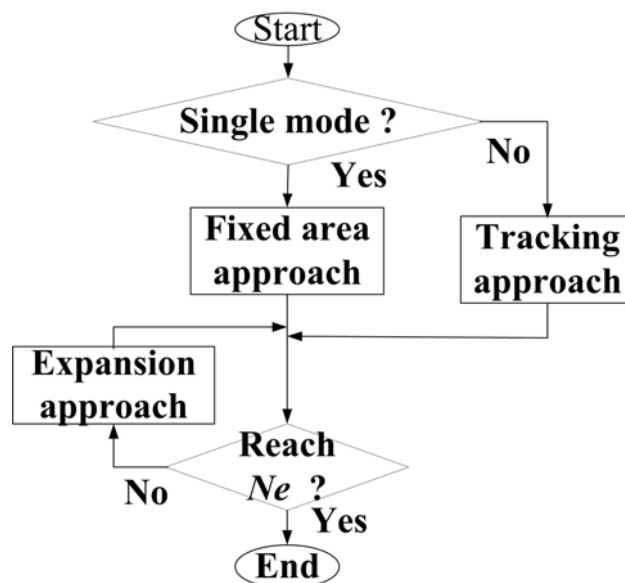


Fig. 3-7. The flow chart of the selection of ROI determination strategies.

$$Roi(M, N_p) = \{I(M, N) \mid M \in [M_L, M_R]; N = N_p\} \quad (3.13)$$

The *ROI* is illustrated as (3.13), where $I(M, N)$ represents the image coordinates; The M -coordinate and the N -coordinate respectively denote the horizontal and vertical coordinates. Here the left bottom coordinate is defined as the origin shown in Fig. 3-8. The *ROI* in the N_p -th row is denoted by $Roi(M_p, N_p)$; where $M \in [M_L, M_R]$, and M_L is the left border within the range, and M_R the right border. Our proposed lane detection method consists of two modes: 1) Single mode: only the information of the current processed frame is considered. 2) Sequential mode: using the temporal information of the previous frames to shrink the search area of the current frame so as to accelerate the detection and reduce errors. The selection of the suitable *ROI* determining strategies for different models are given as follows.

- In every row, the sequence of *ROI* is determined following the bottom-up direction on the N -coordinate and starting from $N=0$ row to the preset terminal row N_e .
- In *single mode*, the *fixed area approach*, as depicted in the following subsection (3.1), is first applied to determine the front parts of two lane markings and then the coordinates of the detected lane markings are considered the start coordinates of the left and right lane markings. Afterwards, the *ROI* of the farther parts of lane markings is determined by the *expansion approach* to follow the bottom-up direction on N -coordinate to the terminal, N_e , as described in subsection (3.2).
- In *sequential mode*, the *ROI* is determined by the *tracking approach* as described in subsection (3.3). If the information of the previous frames does not include N_e , then the *expansion approach* will be conducted to continue the detection to reach N_e .

The flow chart of selecting *ROI* determination strategies is given in Fig. 3-7.

The following subsections will present three kinds of *ROI* decision approaches.

1) *Fixed Area Approach*: This approach is to detect the position of the nearby part of the lane marking. As shown in Fig. 3-8, the determination of the coordinates N_1 and N_2 was based

on their mappings onto the two Z -coordinates, respectively 8 meters and 25 meters on the ground plane because lane markings in this range are usually very clear. After determining N_1 and N_2 , let the two hexagonal areas be the ROI , and these sections are divided by the ν axis. The BFT detected on the left side are the possible positions of the left lane markings and the ones on the right side are the possible right lane markings. The search area of this approach is larger and it is used when no temporal information of lane markings is available.

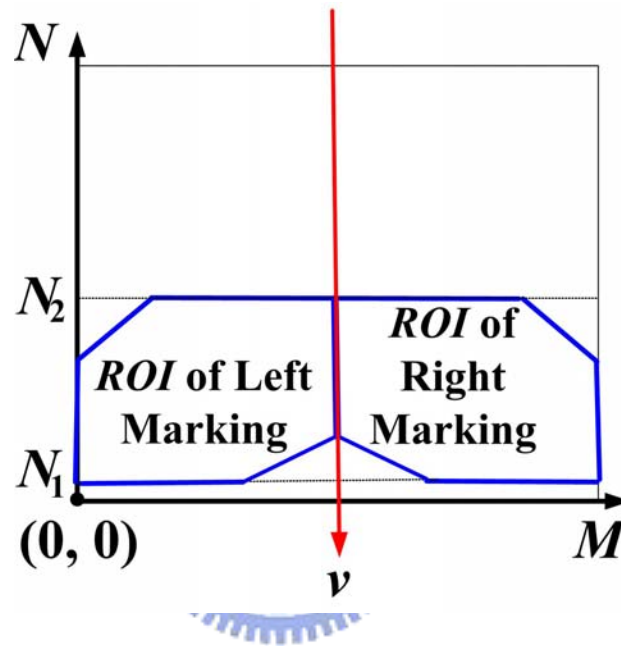


Fig. 3-8. ROI of fixed area.

2) *Expansion Approach*: This approach includes two phases. Phase 1 is a bi-directional expansion scheme. In this scheme, the latest detected position of the BFT is considered as a center, and then the ROI is determined by expanding row by row along the direction of the N -coordinate, as shown in (3.14) and (3.15). Fig. 3-9(a) illustrates the ROI set in this way, where the ROI is the area within the two blue dotted lines along the two sides of the lane markings. In this way, the ROI is set by linear equations as in (3.14) and (3.15). The approach is simple and rapid, but the ROI may expand when the distance between the current row and the last row is extended. Phase 2 is a tendency expansion scheme. This approach is performed by computing the slope of the lane marking to predict its trend and expanding along the direction of the N -coordinate to determine the ROI . The computation method of the slope is

shown in Fig. 3-9(b), where m_b denotes the slope of the lane marking. If a *BFT* is detected continuously in some rows, but can not be detected in the following several consecutive rows, then let $M_{BS(NL)}$ be the *BS* on the latest *BFT*, and M_{BS1} be the *BS* on the *BFT* in the previous rows of $M_{BS(NL)}$. Then the slope of the lane markings can be computed using these two points. With the slope, the *ROI* can be determined by (3.16) and (3.17). The *ROI* calculated in this way is smaller, where the lane marking is included; however, the computational cost of the slope may increase.

$$M_L = (M_{BS(NL)} - D_s) - (N_p - N_L) \times \tan(\beta_{s1}) \quad (3.14)$$

where

$M_{BS(NL)}$: the *M*-coordinate of *BS* in the N_L row.

N_L : the row where *BFT* is latest detected.

D_s : the fixed shift range.

β_{s1} : the fixed angle of expansion.

$$M_R = (M_{BT(NL)} + D_s) + (N_p - N_L) \times \tan(\beta_{s1}) \quad (3.15)$$

where

$M_{BT(NL)}$: the *M*-coordinate of *BT* in the N_L row.

$$M_L = (M_{BS(NL)} - D_s) + (N_p - N_L) / m_L \quad (3.16)$$

where

$$M_{BS(NL)} = (m_{BS}, N_L)$$

m_{BS} denotes the *M*-coordinate of *BS*.

$M_{BS1} = (m_1, n_1)$ represents another M_{BS} .

$$\beta = \tan^{-1} \left(\frac{N_L - n_1}{m_{BS} - m_1} \right)$$

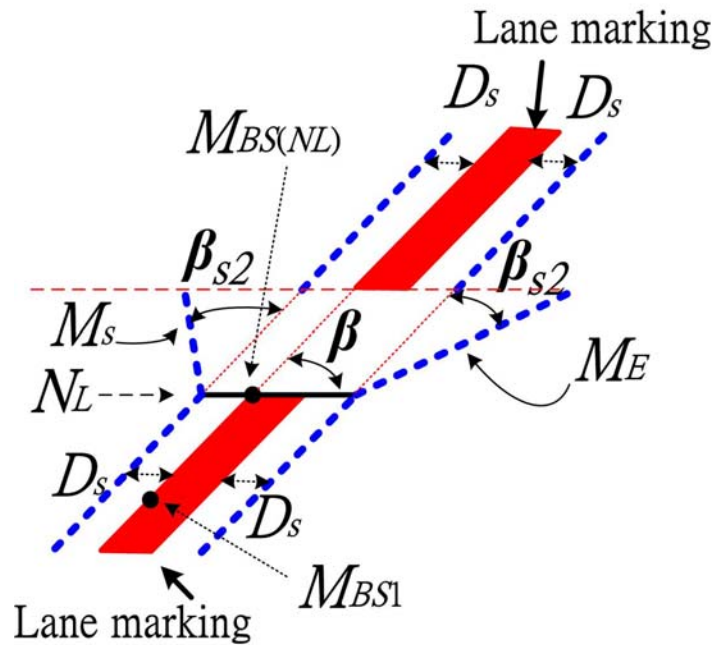
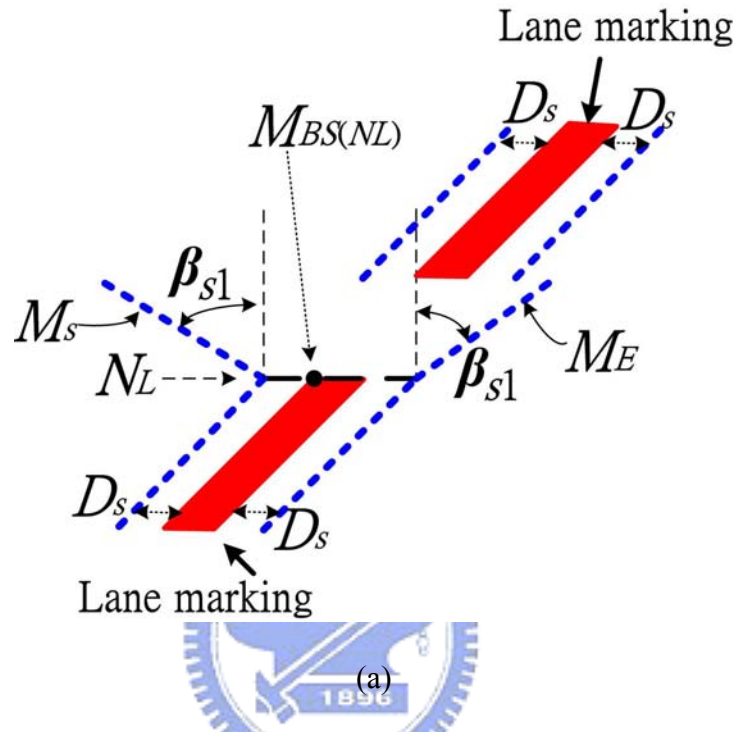
$$m_L = \tan(\beta + \beta_{s2})$$

β_{s2} : the fixed angle of expansion.

$$M_R = (M_{BT(NL)} + D_s) + \frac{N_p - N_L}{m_R} \quad (3.17)$$

where

$$m_R = \tan(\beta - \beta_{s2})$$



(b)

Fig. 3-9. (a) Bi-directional expansion scheme; (b) Tendency expansion scheme.

3) *Tracking approach*: Based on the lane marking features found in previous frames, the *ROI* can be found by (3.18) and (3.19). The *ROI* area found in this way is the smallest one, so it is the best choice for the sequential prediction mode of lane detection.

$$M_L = M_{BS(t-1)} - D_s \quad (3.18)$$

where

$M_{BS(t-1)}$: the *M*-coordinate of *BS* in the N_p row in the previous frame.

t: the current frame. t-1: the last frame.

$$M_R = M_{BT(t-1)} + D_s \quad (3.19)$$

where

$M_{BT(t-1)}$: the *M*-coordinate of *BT* in the N_p row in the previous frame.

Figure 3-10 shows the acquisition of *BFT* in a fixed area. The detection distance is set to be about 25m. In the figure, black lines appear only when the distance between *BFT* on both sides approximates to w_L . Figure 3-11 is the selection of the *ROI* and its range. In (a), (b) and (c), the two-side expansion phase and tendency expansion phase are applied in turn, while the tracking approach is adopted in (d). In Fig. 3-11, the black lines on the two sides of the lane markings respectively represent M_L and M_R of those rows. On the lane markings of both sides, there are totally four big black points denote P_{L1} , P_{L2} , P_{R1} , and P_{R2} for calibrating α .

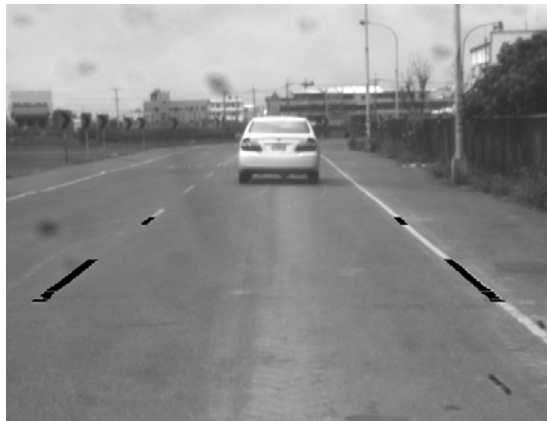
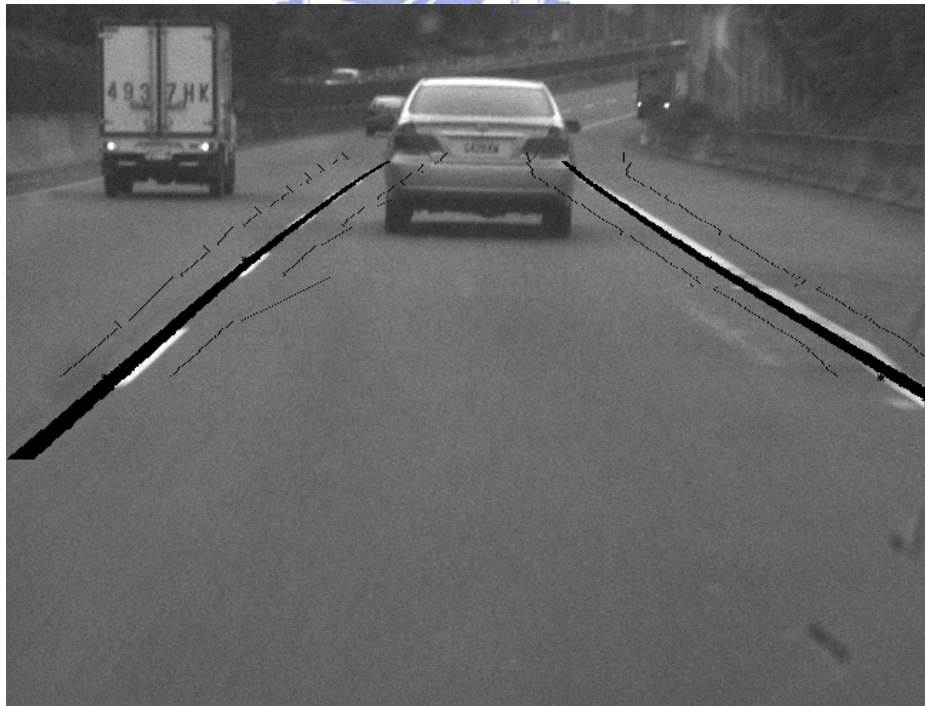


Fig. 3-10. The acquirement of *BFT* in a fixed area.



(a)



(b)



(c)



(d)

Fig. 3-11. The selection of *ROI* and its range. (a)(b)(c) The application of the expansion approach; (d) The adoption of the tracking approach.

3.3.4 Post processing by Fuzzy Reasoning

Some objects or noises whose features are similar to those of lane markings may exist in the image, so they may also be extracted simultaneously. In this study, a post-processing scheme based on fuzzy logic is adopted to determine whether the potential objects are actual lane markings in the extracted image. The following rules are applied to the identification of lane markings.

1) When the length of BFT , $B_L(N)$, detected in the N -th row of the image approximates closer to the computed width of the lane markings, $w_m(N)$, the BFT has a higher possibility of being part of the lane markings. A triangular fuzzy number is used as a membership grade, μ_1 , to represent the degrees of their similarity as in (3.20). The larger the membership grade is, the higher possibility it is for the detected BFT to be part of the actual lane markings. Otherwise, a smaller membership grade reveals that the detected BFT may just be noise.

2) Given a row on the image plane, a pair of BFT s is detected within ROI of both the left and right lane markings, and then the two BFT s may possibly be parts of the lane markings. The possibility rises with the distance between the two BFT , D_B , getting more close to the computed width of the projected lane marking, w_L . The notation $\mu_2(N)$ represents the degrees of similarity between D_B and w_L in (3.21).

$$\mu_1(N) = \begin{cases} (B_L(N) - w_m(N)) / w_m(N) + 1, & \text{if } 0 \leq B_L(N) \leq w_m(N) \\ -(B_L(N) - w_m(N)) / w_m(N) + 1, & \text{if } w_m(N) \leq B_L(N) \leq 2 \times w_m(N) \\ 0, & \text{others} \end{cases} \quad (3.20)$$

where $B_L(N)$ means the length of BFT first detected by FSM in the N -th row and $w_m(N)$ denotes the width of the lane marking projected on the N -th row by (3.6). The notation $\mu_1(N)$ represents the degrees of similarity between $w_m(N)$ and $B_L(N)$.

$$\mu_2(N) = \begin{cases} 2 \times (D_B(N) - w_L(N)) / w_L(N) + 1, & \text{if } 0.5 \times w_L(N) \leq D_B(N) \leq w_L(N) \\ -2 \times (D_B(N) - w_L(N)) / w_L(N) + 1, & \text{if } w_L(N) \leq D_B(N) \leq 1.5 \times w_L(N) \\ 0, & \text{others} \end{cases} \quad (3.21)$$

where $D_B(N)$ represents the distance between two *BFT*s on the N -th row and $w_L(N)$ means the projective lane width on the N -th row by (3.3); and $\mu_2(N)$ denotes the similarity between $D_B(N)$ and $w_L(N)$.

3) Suppose that all lane markings are longitudinally consistent, thus, the *BFT* detected within the *ROI* on the left or right lane markings should be parts of them. Let the range of the projective lane markings be the rows of $[0, N_e]$ on the N -coordinate, then each *BFT* detected within the area can obtain a membership grade μ_1 . Let a fuzzy set F_M denote the set of μ_1 on the same lane marking as in (3.22). All membership grades in F_M should be similar since they belong to the *BFT* on the same lane marking. Therefore, if μ_1 of one *BFT* matches the condition in (3.23), then the *BFT* is regarded as a part of the lane marking; otherwise, it is noise.

$$F_M = \{(N, \mu_1(N)) \mid N \in [0, N_e]\} \quad (3.22)$$

where N_e represent the preset terminal row.

$$|\mu_1(N) - \mu_m| \leq \sigma_1^2 \quad (3.23)$$

where μ_m is the mean of $\mu_1(N)$ in Fuzzy set F_M .

σ_1^2 is the variance of $\mu_1(N)$ in Fuzzy set F_M .

4) Let lane projections be within the range $[0, N_e]$ in the N -coordinate. If *BFT* is detected within the left and right areas of the *ROI*, then $\mu_2(N)$ can be obtain by (3.21). Let Fuzzy set F_L denote the set of μ_2 on the same lane as in (3.24). Suppose that changes of lane width are slight, then each $\mu_2(N)$ computed based on the *BFT* should be similar. The existence of lane

markings on both sides in the N row is determined by (3.25) and $\mu_2(N)$. Accordingly, whether lane markings exist on both sides can be determined. Besides, search the *BFTs* on the same lane marking which meet rule 3, and next compute the associated Z -coordinates of those *BFTs*' v -coordinates by (3.1). If the Z -coordinates between two neighboring *BFTs* exceed 10 meters, it means that the area between them is occluded. Then one side of the lane marking should be compensated by the other side.

$$F_L = \{(N, \mu_2(N)) \mid N \in [0, N_e]\} \quad (3.24)$$

$$|\mu_2(N) - \mu_{2m}| \leq \sigma_2^2 \quad (3.25)$$

where μ_{2m} is the mean of $\mu_2(N)$ in the fuzzy set F_L .

σ_2^2 is the variance of $\mu_2(N)$ in the fuzzy set F_L .

The application of the rules is described as follows: first, compute $\mu_1(N)$ and $\mu_2(N)$ by rule 1 and 2. Then, choose the *BFT* which satisfies most conditions of lane markings by rule 3. Next, rule 4 is applied to judge whether there is any occlusion on the left and right lane markings. Finally, determine the positions of knots based on rules 3 and 4 to reconstruct the lane as shown in the following section.

3.3.5 Reconstruction Process of Occluded lanes

Some lane markings are dashed lines and some may be occluded by obstacles; thus, the detected lane markings cannot completely reveal the driving lane in the whole area. To overcome these issues, the B-spline technique is used to interpolate the positions of lane markings to obtain the complete lane boundaries. The Cubic B-spline is a smooth curve with continuous second order derivatives [57][87]-[90], fitting curves of various lane markings by using several control points.

(1) Decision of control points

Let C_i be the i^{th} control point in the control point set C_s , as expressed in (3.26), and then the cubic B-spline is $B(s)$, as shown in (3.27); which contains connected curve segments $g_i(s)$.

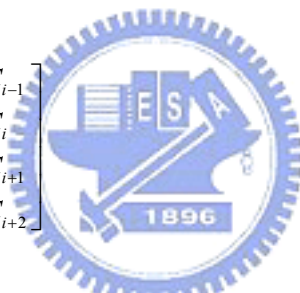
$$C_s = \{C_i \mid i = 1, 2, \dots, n\} \quad (3.26)$$

where the coordinates of C_i are (M_i, N_i) . M_i and N_i respectively represent the M -coordinate and N -coordinate in the image. i ranges from 1 to n , which means the number of control points is n .

$$B(s) = \sum_i g_i(s), 0 \leq s \leq 1 \quad (3.27)$$

where

$$g_i(s) = (M_i(s), N_i(s))$$

$$= \begin{bmatrix} s^3 & s^2 & s & 1 \end{bmatrix} \begin{bmatrix} -\frac{1}{6} & \frac{1}{2} & -\frac{1}{2} & \frac{1}{6} \\ \frac{1}{2} & -1 & \frac{1}{2} & 0 \\ -\frac{1}{2} & 0 & \frac{1}{2} & 0 \\ \frac{1}{6} & \frac{2}{3} & \frac{1}{6} & 0 \end{bmatrix} \begin{bmatrix} C_{i-1} \\ C_i \\ C_{i+1} \\ C_{i+2} \end{bmatrix}$$


where $i=2, 3, \dots, n-2$.

s is a normalized curve length.

Lane markings may appear in straight lines, curves, and even S-shape turns. Therefore, it is difficult to completely model lane markings with various forms with linear or quadratic equation models. In this study, a B-spline of connected curve segments $g_i(s)$ is applied to fitting the curved lane markings. A variety of lane markings with general characteristics can be modeled by this approach. To enable B-spline to go through the first and last control points, the two control points are repeated three times. Five control points are determined to be $C_1, C_1, C_1, C_2, C_3, C_4, C_5, C_5, C_5$ as shown in Fig. 3-12. The connected points of the curves are named knot points. The positions of the control points can be determined according to those of the

knot points. Substituting $s=0$ into (3.27) and the results in (3.28) can be obtained. Then, based on (3.28), three knot points k_2 , k_3 , and k_4 on the lane marking are selected between C_1 and C_5 to obtain three control points C_2 , C_3 , and C_4 as shown in (3.29).

$$C_i = \frac{3}{2}k_i - \frac{1}{4} \times (C_{i-1} + C_{i+1}) \quad (3.28)$$

where

$i=2, 3, \dots, n-2$.

$$\begin{bmatrix} C_2 \\ C_3 \\ C_4 \end{bmatrix} = \begin{bmatrix} -\frac{15}{56} & \frac{45}{28} & -\frac{3}{7} & \frac{3}{28} & -\frac{1}{56} \\ \frac{1}{14} & -\frac{3}{7} & \frac{12}{7} & -\frac{3}{7} & \frac{1}{14} \\ -\frac{1}{56} & \frac{3}{28} & -\frac{3}{7} & \frac{45}{28} & -\frac{15}{56} \end{bmatrix} \begin{bmatrix} C_1 \\ k_2 \\ k_3 \\ k_4 \\ C_5 \end{bmatrix} \quad (3.29)$$

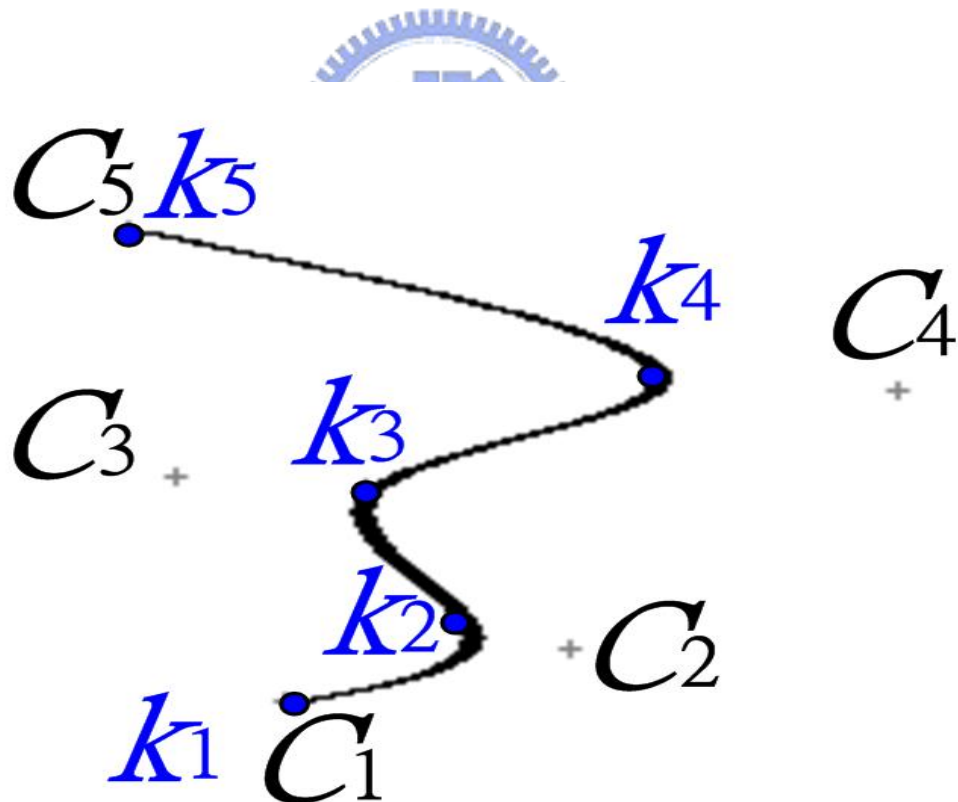


Fig. 3-12. The B-spline model for lane marking detection.

(2) Decision of knot points

In this study, a lane marking is formed by connecting five knot points using B-spline. The position of 2nd knot point, k_2 , is selected by the mapping position in the image of the lane marking near Z -coordinate =10m; in the 3rd knot, k_3 , the associated Z -coordinate is about 25m. The lines passing through k_3 and k_2 intersect at the bottom row of the image coordinate, and the associated intersection is denoted by k_1 . Knot 5 is at the end of the lane marking, and knot 4 is chosen from a suitable place between knots 3 and 5 which is the most probable position of a *BFT* on a lane marking by Fuzzy rule. Knot 1 and 5 are determined by this way as well, and they are the control points C_1 and C_5 .

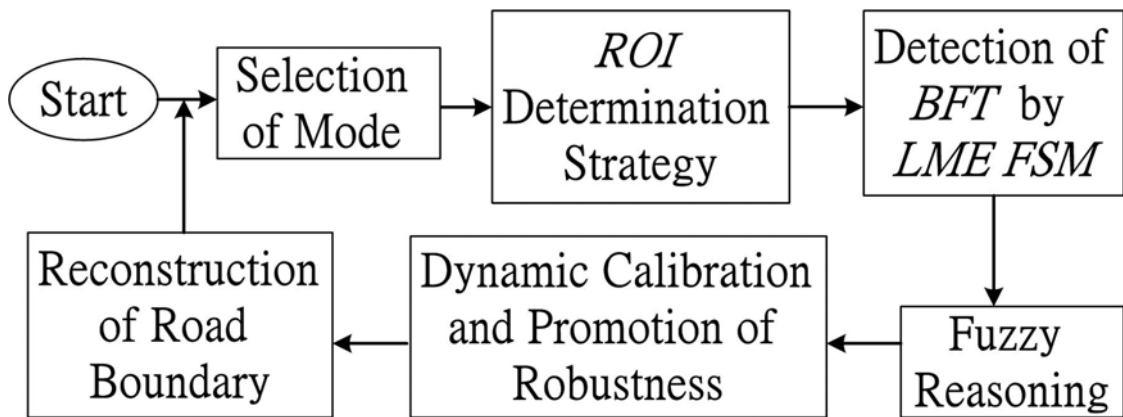


Fig. 3-13. Procedures of the lane marking detection.

3.3.6 Overall Process of Lane Detection

In single mode, the Fixed Area *ROI* approach is first applied to the *LME FSM* process to extract lane markings. After lane markings are found, the lane width and the tilt angle of the camera are updated by the dynamic calibration process, and then the Expansion *ROI* approach is applied again to extracting lane markings. This process can provide more accurate detection results. Because the calibration of the camera tilt angle and lane widths requires information of two lane markings, therefore, in the single mode, the information of the two lane markings

in the fixed *ROI* is needed. If only the information of the left or right lane marking is available, it is possible that one side of the lane marking is occluded.

The information of this occluded lane marking can be compensated by the information of the previously detected lane width and the other side of the lane marking. The procedures are shown in Fig. 3-13.

Step 1: Selection of Modes. Apply the sequential mode when the previous information is logical and adequate; otherwise, use the single mode.

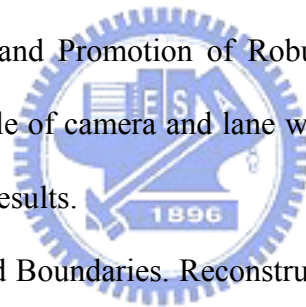
Step 2: *ROI* Determination Strategy.

Step 3: Detection of *BFT* by *LME FSM*.

Step 4: Fuzzy Reasoning. Determine the points used to calibrate the tilt angle of the camera and the knots adopted to reconstruct road boundaries.

Step 5: Dynamic Calibration and Promotion of Robustness. Apply dynamic calibration to obtain the actual tilt angle of camera and lane width. Then, apply the Kalman filters to stabilize the calibration results.

Step 6: Reconstruction of Road Boundaries. Reconstruct road boundaries using B-spline, and then go back to step 1.



3.4 Experimental Results

In this section, comparative experiments on lane detection are conducted. This study utilizes a Hitachi KP-F3 camera mounted in an experimental intelligent car with a physical pixel size of $7.4\mu\text{m}$ (H) $\times 7.4\mu\text{m}$ (V), and the image resolution is 644×493 . The height of the camera is set at 1.32m, the focal length $f=15\text{mm}$, and tilt angle α about 4 degree. Our experimental system is a PC with CPU Pentium IV 2.8GHz. Suppose the width of the lane marking is 0.1meters and the initial lane width is 3.3m. The farthest distance of detection is 60 meters, and the associated computed projective width of the lane marking is about 5 pixels.

The experimental conditions and results are shown as Table 3-2. The average computation time that the proposed method required is less than 13ms per frame. Under general conditions, the average detection ratio can reach above 98% and exceed 95% when there are occlusions.

Table 3-2 The computation timings under different conditions by the proposed system

Conditions	The number of frames	Average computation time	Detection ratio
Straight road	3500	4.5 ms	99.1%
Curve road	2200	7.3 ms	98.7%
Daytime occluded	1250	12.2 ms	96.4%
Shadow	1100	9.5 ms	96.5%
Strong sunlight	500	9.3 ms	97.2%
Night	2100	7.2ms	98.3%
Night occluded	1200	12.9 ms	95.1%

3.4.1 Lane Detection Results

1) Dynamic calibration of camera tilt angle

Figure 3-14 demonstrates the result of the dynamic calibration of camera's tilt angle. In the figure, "Original" means the calculated tilt angle in each frame. "Kalman" denotes the processed tilt angle by a Kalman filter. The Kalman filter can provide the robust estimation of the current tilt angles through recursive functions [91][92]. This process provides the more stable and robust calibration results of the tilt angle for the lane detection system. Figure 3-14 shows that the change of "Kalman" gets smaller.

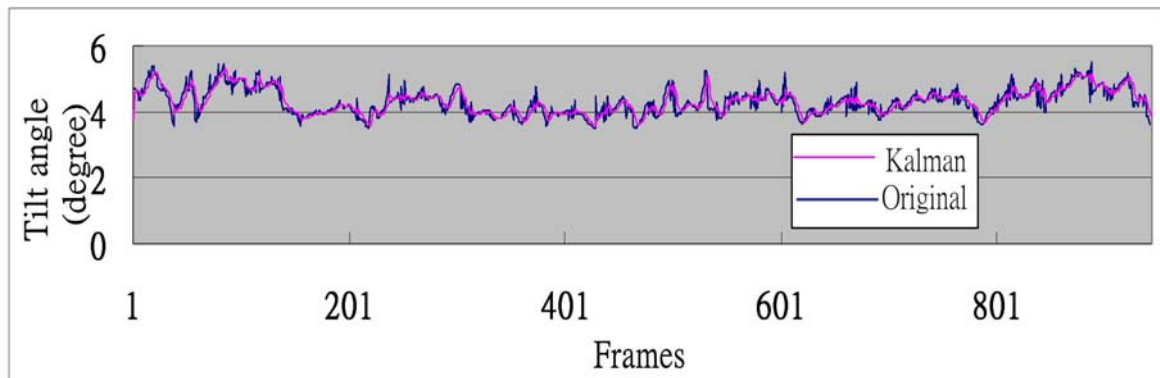


Fig. 3-14. The result of the dynamic calibration of camera's tilt angle.

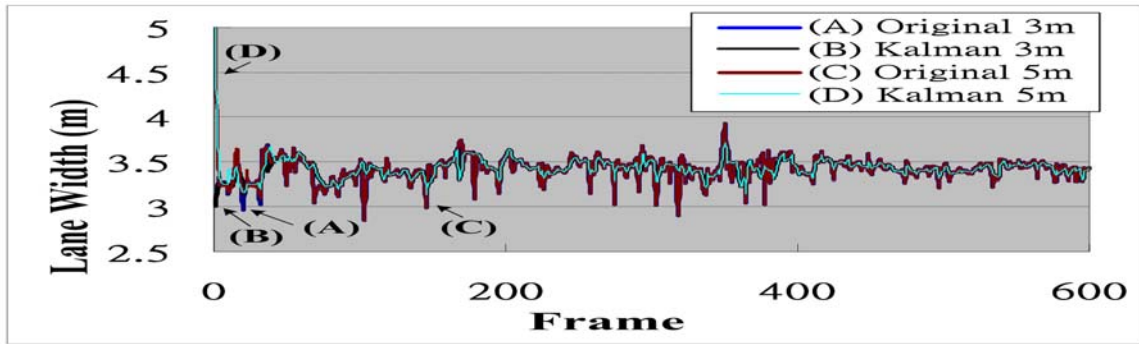
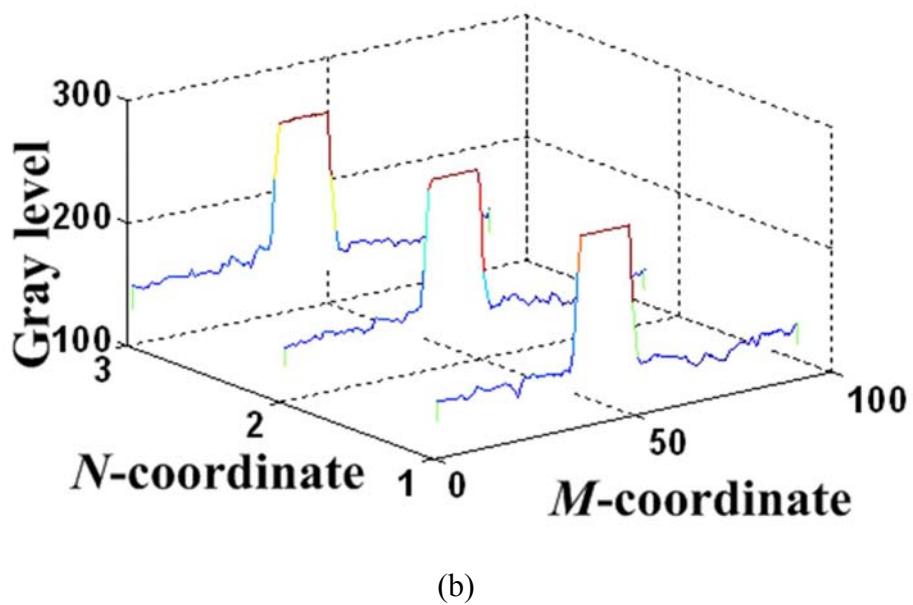
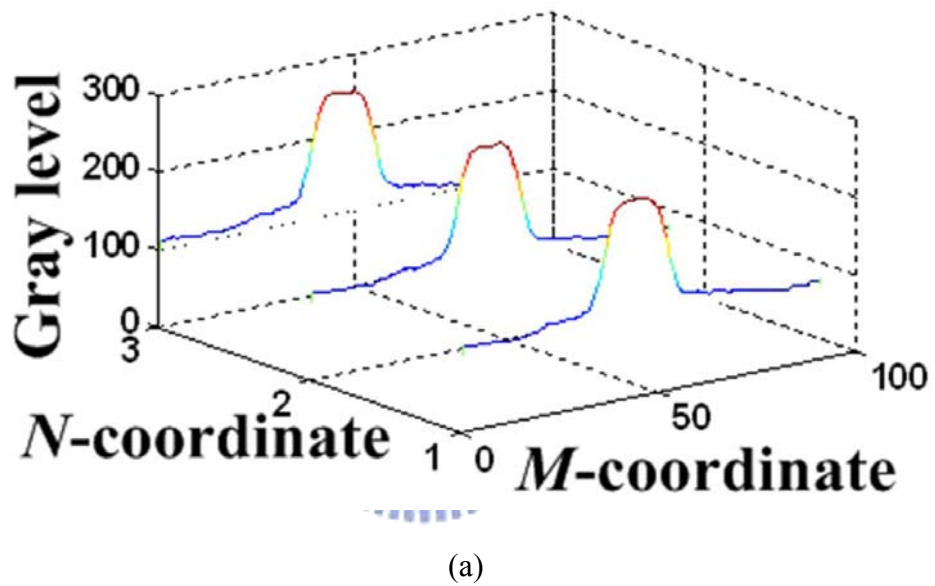
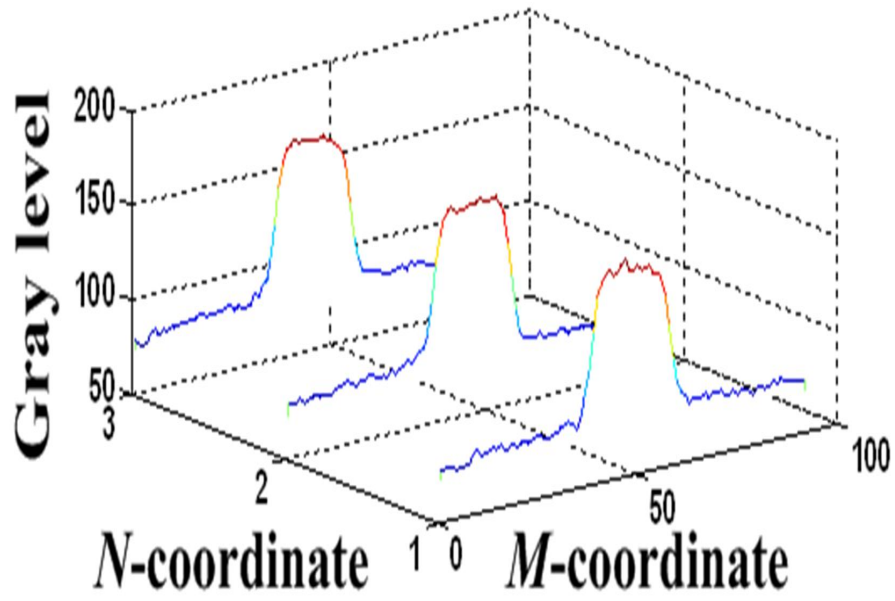
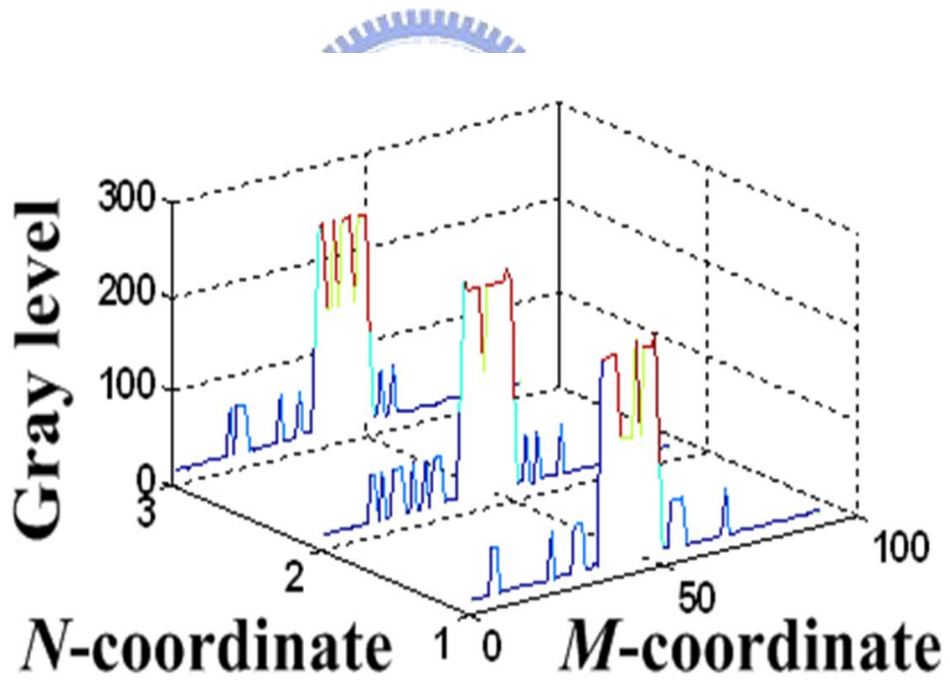


Fig. 3-15. The estimated lane width in every frame.





(c)



(d)

Fig. 3-16. The gray level of lane markings under different illumination. (a) General light; (b) Strong sunshine; (c)Dusk ; (d) Night.

Table 3-3 Results of lane width estimation in the four situations

Curve	(A)	(B)	(C)	(D)
Mean (m)	3.422	3.421	3.423	3.424
Standard deviation (m)	0.1221	0.0874	0.1217	0.0885
Average error (m)	0.022	0.021	0.023	0.024

2) Lane width refinement

In lane detection, the initial settings are based on general width of lanes, i. e. 3m-5m, and the actual lane widths will later be adaptively refined based on the detected positions of the left and right lane markings in the image. Besides, to promote the robustness of lane width refinement, a Kalman filter is also adopted to stabilize and refine the process of lane width estimation.

Figure 3-15 shows the estimated lane widths with different preset widths and with/without Kalman filters in the sequential frames, where curve ‘(A) original 3m’ and ‘(C) original 5m’ respectively represent the estimated lane widths with initial lane widths in 3m and 5m. The initial lane width of curve (A) and (C) were respectively set to be 3m and 5m. The curve ‘(B) Kalman 3m’ and ‘(D) Kalman 5m’ respectively denote the estimated lane widths of curve (A) and (C) refined by the Kalman filter. By observing those results, the estimated lane widths with different preset lane widths will finally be refined to be closer to the actual ones. The application of the Kalman filter ensures stable and robust estimate results of the lane widths in the world coordinates. Table 3-3 displays the mean, standard deviation and average errors of the estimated lane widths in curve (A), (B), (C), and (D), and the actual lane width is about 3.4m. As can be seen, the estimated results in sequential frames are all quite close to the actual lane width and all of the average errors are under 0.024m. Furthermore, when the initially set lane width changes within the range from 3-5m, the obtained estimation results are still similar and close to the actual lane widths. The results show that our approach of lane width refining is robust and accurate.

3) Results of adaptation to illumination conditions

D_{g1} , D_{g2} , and D_{g12} are determined by a statistical search algorithm based on the following two principles. (a) All gray level of lane markings is higher than those of the ground. (b) The variations of the gray levels of the ground and lane markings are within a reasonably fixed range. To demonstrate that our approaches are robust and adaptive to changes of illumination, variations of the gray levels of lane markings and grounds under four different illuminations are analyzed. The results are shown as Fig. 3-16, where lanes and lane markings display different gray level and contrast under different illumination. As can be seen from this fact, the principles (a) and (b) are appropriately followed under different illumination conditions, and the proposed statistical search algorithm can correctly and adaptively determine D_{g1} , D_{g2} , and D_{g12} under various illumination conditions. Table 3-4 displays D_{g1} , D_{g2} , and D_{g12} obtained from the four sample road scenes under different illumination conditions in Fig. 3-16, where D_{g1} , D_{g2} , and D_{g12} are adaptively adjusted with various illuminations. As shown in Figs. 3-17~3-21, the adaptively determined thresholds can provide satisfactory lane detection results under different illumination conditions.

Table 3-4 The obtained parameters under different illumination conditions

Illumination conditions	D_{g1}	D_{g2}	D_{g12}
(a)General light	35	60	55
(b)Strong sunshine	30	10	85
(c)Dusk	25	20	50
(d)Night	70	110	75

Figure 3-17 shows the conditions of curves and a slope. In these figures, the roads with sharp curves and slopes still can be described by B-spline with four segments. Figure 3-18 is the situations with occlusion of obstacles. (a) The near front vehicle occluded lane markings of both sides. (b) The vehicle occluded the right lane marking. (c) The vehicle moved back to the road center. (d) The vehicle occluded the left lane marking. (e) The vehicles approached lane markings. (f) Another vehicle occluded the right lane marking. The figures prove the

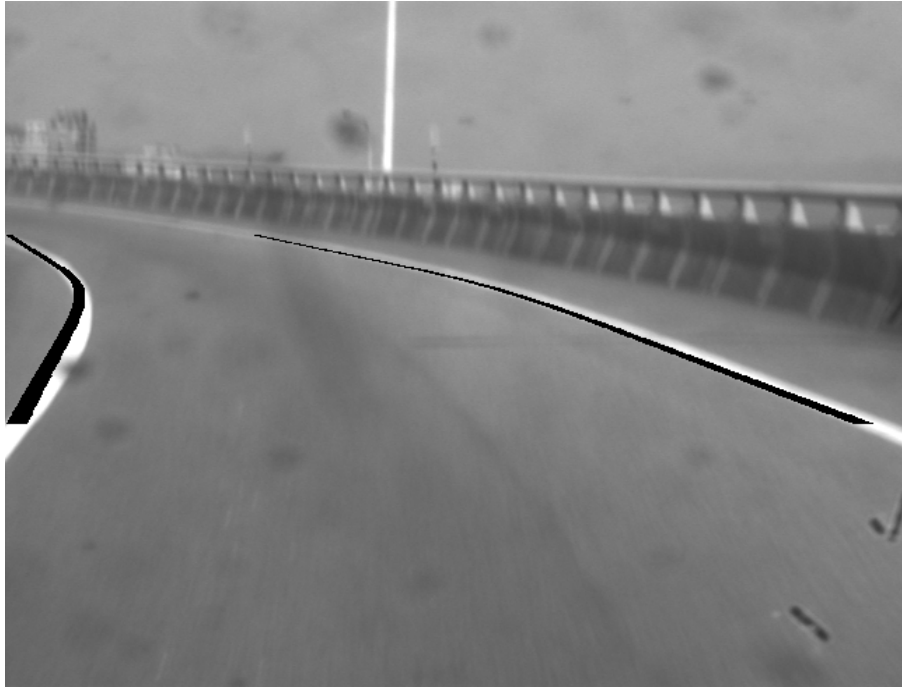
problem of occlusion can be solved by the proposed approaches. The information of the side which is not occluded can be used to substitute the occluded one. When both sides of the lane markings are occluded, then only the parts that are not occluded can be shown.



(a)



(b)

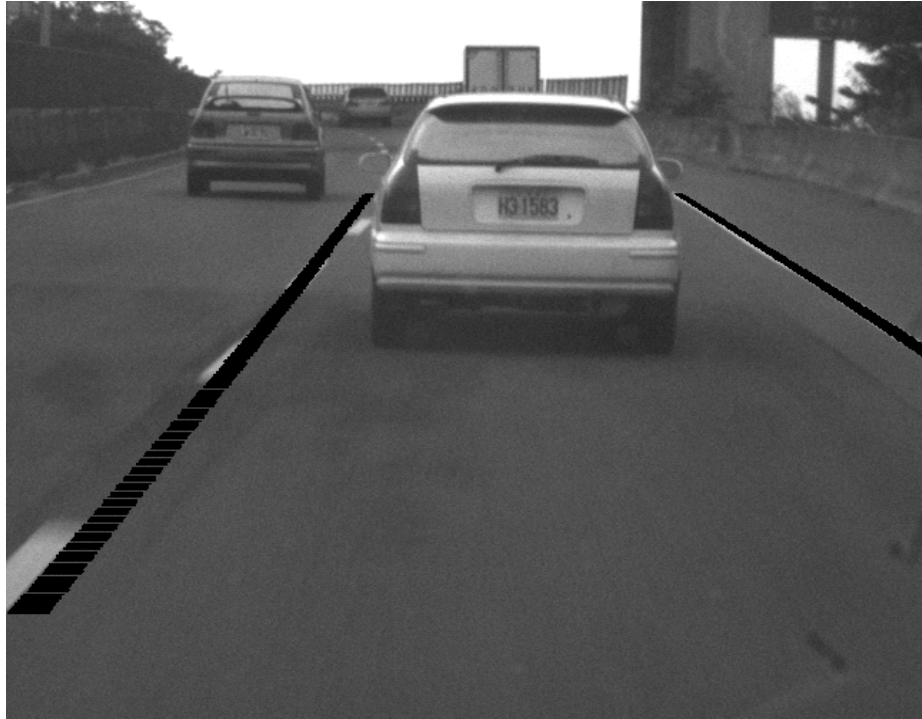


(c)



(d)

Fig. 3-17. (a) Curves; (b) A slope; (c)(d) A cloverleaf interchange.



(a)



(b)



(c)



(d)



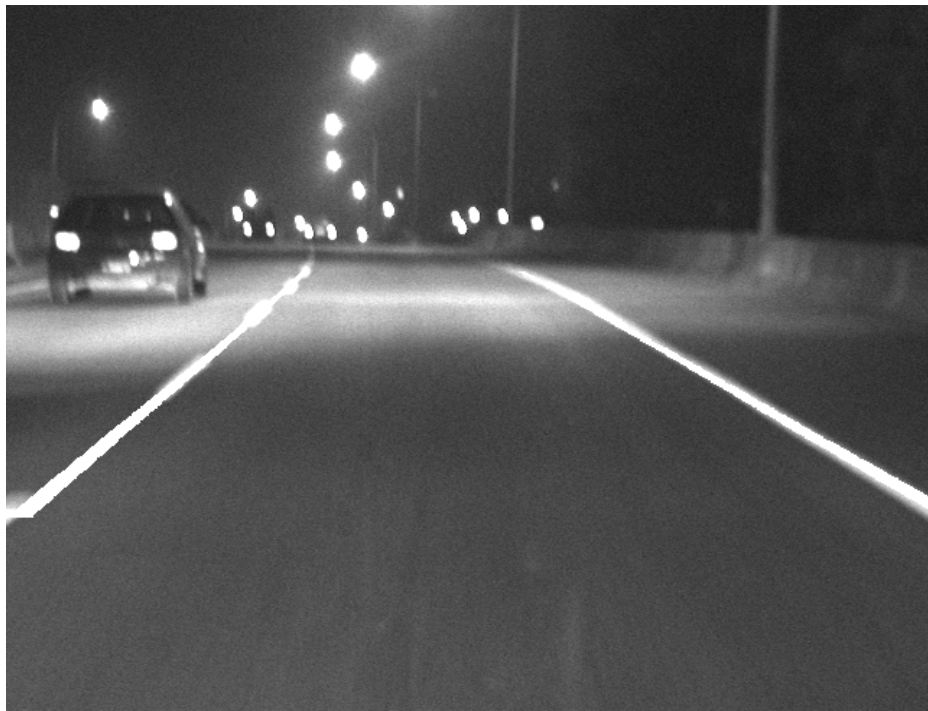
(e)



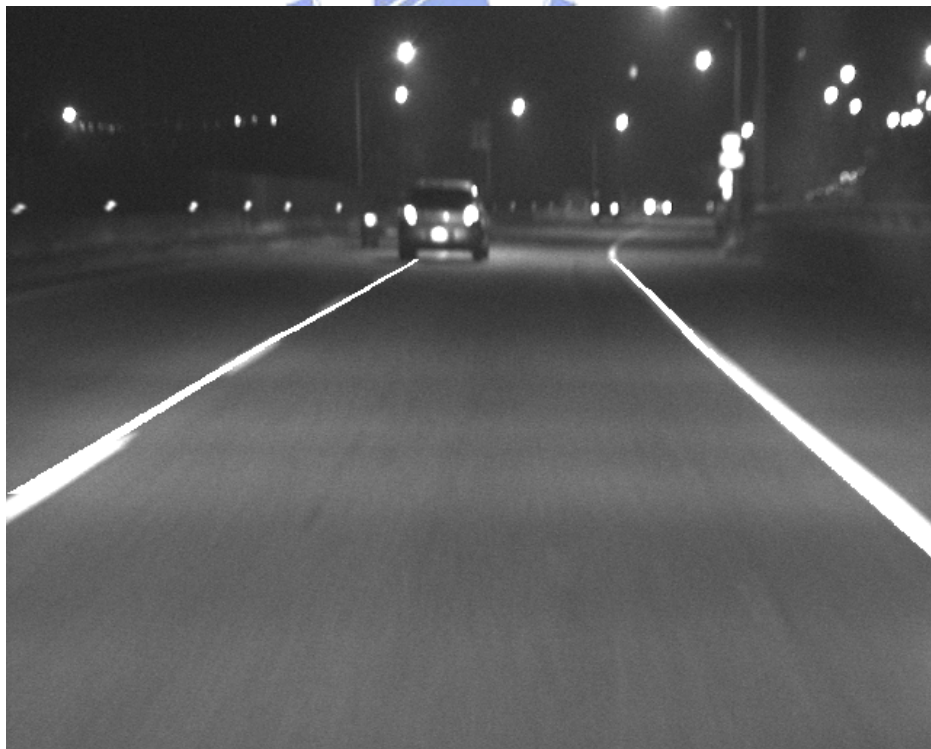
(f)

Fig. 3-18. (a)(b)(c)(d)(e)(f) Situations of occlusion with different obstacles.

Figure 3-19 displays the detection results at night in situations including roads with or without road lamps and textures on the road surface, roads with curves and occlusion.



(a)



(b)



(c)



(d)

Fig. 3-19. Results of the nighttime road scene. (a)(b) With road lamps; (c)(d) Without road lamps.

Figure 3-17~3-19 present that *FSM* can extract *BFT* in various situations regardless of the influences of patterns on the road surface and illumination, and B-spline with four sections is able to display a variety of road conditions.



(a)



(b)



(c)



(d)

Fig. 3-20. The detection results under strong sunlight. (a)(b) No occlusion of vehicles; (c)(d) with the occlusion of a vehicle.

Figure 3-20 is the detection result under strong sunlight. The proposed approach can correctly detect the lane markings without being influenced by the strong sunlight.



(b)

Fig. 3-21. The detection result of a motorcycle inside and outside the lane. (a) Inside; (b) Outside.

Figure 3-21(a) and (b) respectively show a clear discrimination of a motorcycle inside and outside the lane. Obstacles inside the lane will affect driving safety. However, most contemporary lane detection approaches may not be able to discriminate whether an obstacle is inside or outside the lane when obstacles appear near the lane so they cannot correctly detect lane markings. In contrast, the proposed approach can resolve the problem of obstacle occlusion to reconstruct correct lane markings.

3.4.2 Comparative Performance Evaluation

In this subsection, comparative experiments on Jung and Kelber's method [46] and the proposed approach is conducted to evaluate their performances on lane detection under different conditions. The following is a comparison of acquiring *BFT* by *FSM* and other approaches:

Figures 3-22~3-26 are respectively the comparative results of Jung and Kelber's [46] and our proposed approach under different situations, where (a) is Jung and Kelber's approach and (b) is our proposed approach. Figure 3-22 is the condition that the lane markings are occluded with shadows, signs of braking and other vehicles. Jung and Kelber adopted Sobel edge features of lane boundaries, which left large gradient points in the thresholded edge image, as shown in Fig. 3-22(a), the surrounding vehicle may cause false detection in the edge feature extraction process and result in detective errors. As shown in Fig. 3-22(b), the proposed approach successfully extracts features of lane markings with the *BFT* detector. The end part of the reconstructed lane boundary is the position of the last *BFT*, and the missing part at the end of the left-side lane marking is reconstructed with the information of the lane width and of the right-side lane marking.



(a)



(b)

Fig. 3-22. Results of the road scene that the lane markings are occluded with shadows, signs of braking. (a) Results of Jung and Kelber's [46]; (b) Results of the proposed approach.



(a)



(b)

Fig. 3-23. Results of road scenes with a curve lane and occlusion. (a)Results of Jung and Kelber's [46]; (b) Results of the proposed approach.

Figure 3-23 shows the results of the road scene consisted of curve lane and occlusion. Figure 3-23(a) shows that the lane markings obtained by Jung and Kelber's method have errors occurring on curves of roads when edge features of vehicles are mis-detected as the lane markings. Figure 3-23(b) demonstrates that our *BFT* approach can compensate the influences of appearing vehicles.



Fig. 3-24. Results of the road scene under strong sunlight. (a)Results of Jung and Kelber [46]; (b) Results of the proposed approach.

Figure 3-24 displays the detection results under strong sunlight. In Fig. 3-24 (a), edge features of vehicles associated with significant gradient features under strong sunlight cause possibly wrong determination of lane features. As shown in Fig. 3-24(b), with the *BFT* method, the proposed approach will not capture positions without lane markings to avoid wrong judgments in the far end of the lane. Therefore, lane boundaries can be reconstructed successfully.

Figure 3-25 displays the detection results at night. In Fig. 3-25(a), larger gradient arouses detection errors because of the opposite vehicle light and the light reflection of the preceding vehicle. The proposed approach can detect lane markings efficiently and correctly as shown in Fig. 3-25(b), because it takes projective sizes and sequences of lane markings into consideration in capturing *BFT*.

Figure 3-26 shows the detection results of the road scene with an S-shape lane. In Fig. 3-26(a), the S-shaped lane cannot be completely reconstructed when Jung and Kelber applied a linear-parabolic model to reconstruct lane boundaries. Figure 3-26(b) demonstrates that the proposed approach can successfully reconstruct the S-shaped lane boundary.

As can be seen from the above comparative results, the proposed approach can obtain satisfactory detection results under different situations, such as different illumination conditions, curve roads, and occlusions. This is because lane markings are extracted by the proposed *BFT* detector, and extraction errors can be effectively reduced by the proposed dynamic calibration method, *ROI* determination strategy and fuzzy rule-based scheme, and road boundaries are effectively reconstructed by the B-spline technique. Besides, when both sides of lane markings do not exist, or are occluded at the farther parts of the road, the range of the reconstructed lane is determined by the actual visible position of the lane, so the information obtained from previous frames will not be misused to reconstruct false lanes and driving safety can be improved.



(a)



(b)

Fig. 3-25. Results of the nighttime road scene. (a). Results of Jung and Kelber's [46]; (b) Results of the proposed approach.



(a)



(b)



(c)



(d)

Fig. 3-26. Results of the road scene with an S-shaped lane. (a)(b) Results of Jung and Kelber's [46]; (c)(d) Results of the proposed approach.

3.4.3 Comparative Analysis

In this subsection, a comparative analysis on Jung and Kelber [46], Jeong and Nedeveschi [43], Cheng *et al.* [56], and the proposed method is provided as shown in Table 3-5. Cheng *et al.* adopted a color camera, while others used monochrome cameras. The color camera is able to obtain information on colors in the images, but it costs more and takes more time to process more information.

As to the extraction methods, Jung and Kelber [46] used a Sobel mask to conduct edge extraction, in which processing one pixel required 10 additions, 4 multiplications, and a Hough Transform to carry out line detection, so this method suffers high computation cost. Jeong and Nedeveschi [43] applied a Gabor filter, which required complicated computational cost for exponential and trigonometric functions. Cheng *et al.* [56] adopted three multivariable Gaussian distributions to show three classes of lane-mark colors and computed the probability distribution of pixels belonging to the lane-mark, which also involved more complicated computations to analyze three color classes. The proposed *LME FSM* needs only simple linear equation in every row to determine widths of lanes and lane markings, and it only requires one subtraction to calculate the difference in gray level of each pixel. Therefore, the computation cost is the smallest and is applicable to an embedded system. The proposed *ROI* could effectively choose a suitable strategy to narrow down the detection area and greatly reduce the time for detection. Furthermore, only the proposed approaches obtains both the camera tilt angle and the lane width with the information of images, and solved the problem of moving camera vibrations and occlusion on the lane marking without the information of colors. Besides, the proposed approach adopts the statistical search algorithm to determine the gray level range of ground and lane markings, so it enables *BFT* detector to effectively extract lane markings in various conditions of illumination.

Table 3-5 Comparison of different algorithms

Method	Camera type	Extraction method	Dynamic calibration	Occlusion handling	Computational cost	Illumination condition adapting
Jung and Kelber [46]	Mono-chrome	Sobel mask and Hough Transform	N/A	Poor	High	Fair
Jeong and Nedevschi [43]	Mono-chrome	Gabor filter	N/A	Poor	High	Fair
Cheng <i>et al.</i> [56]	Color	Multivariable Gaussian distributions	Tilt	Fair	Medium	Fair
Our proposed method	Mono-chrome	<i>LME FSM</i> + <i>ROI</i> strategy	Tilt, width of lane	Good	Low	Good

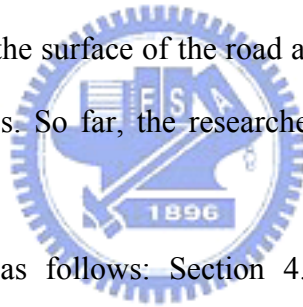


Chapter 4

Vehicle Detection

4.1 Introduction

A vision-based vehicle and lane detection system can detect vehicles and lanes with a camera mounted on a vehicle, compute the range between the camera and the vehicles in lanes, provide the results of lane and vehicle detection for driving assistance systems to avoid collisions [62][93][94]. This kind of the intelligent vehicle system identifies lanes, obstacles, vehicles, texts and patterns on the surface of the road and shadows from 2D images by means of image processing techniques. So far, the researches in this area are still open questions [95]-[98].



This chapter is organized as follows: Section 4.2 presents features of rectangle-like obstacles. Section 4.3 provides the approach, CSS, used to detect rectangle-like obstacles. The experimental results are shown in Section 4.4.

4.2 Vehicle Model

If the size of a rectangle-like object inside the driving lane resembles that of a vehicle, it is regarded as a vehicle. The closest preceding vehicle in the lane of the autonomous vehicle, whose influence on the movement of the autonomous vehicle is the greatest, is the main target of the vehicle detection. The proposed approach aims to detect the target vehicle based on its feature of rectangle-like contour and the estimation of its projective size.

4.2.1 Vehicle Features

Vehicles in the image look like rectangles. Rectangular obstacles contain all of the following features 1, 2 and 3.

- Feature 1: The contact plane between the road surface and a rectangular obstacle projects a horizontal line on the image, as w_i shown in Fig. 4-1(a).
- Feature 2: The left and right sides of rectangular obstacles project vertical lines on the image, as h_i shown in Fig. 4-1(a). Conversely, objects such as lane markings or shadows on the road do not project vertical lines in the image as shown in Fig. 4-1(b).

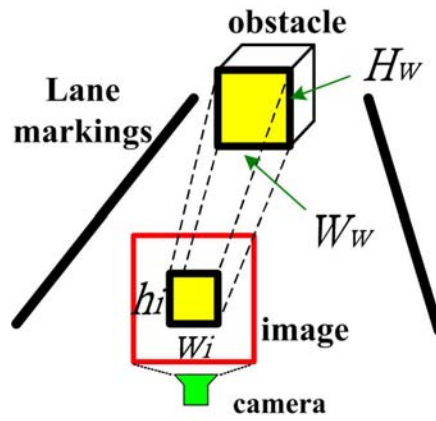
Based on features 1 and 2, the projection of a rectangular obstacle contains both horizontal and vertical lines.

- Feature 3: The projective size of an object in the image varies with its distance to the camera. In Fig. 4-1(c), p is the lens center and Z_1 projects on v_1 . Based on the properties of similar triangles, the relation between Z_1 and v_1 is shown as (4.1), where Z_1 represents the vertical range between the obstacle and the camera. Besides, the projective height of the obstacle H_w is h_i and their relation is shown in (4.2). Similarly, in Fig. 4-1(a), the projective width of the obstacle W_w is w_i in (4.3). Based on (4.1)-(4.3), the projective height and width are predictable.

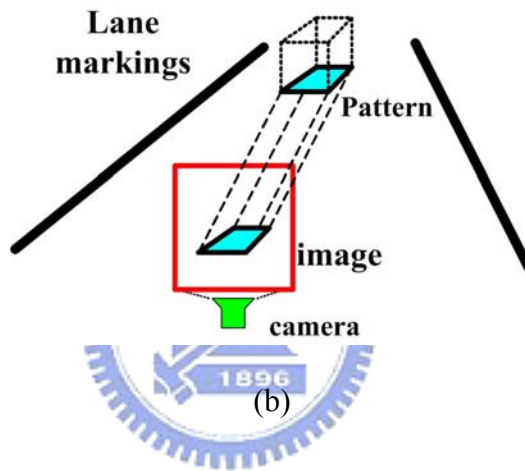
$$Z_1 = \lambda \frac{h}{v_1} \quad (4.1)$$

$$h_i = \lambda \frac{H_w}{Z_1} \quad (4.2)$$

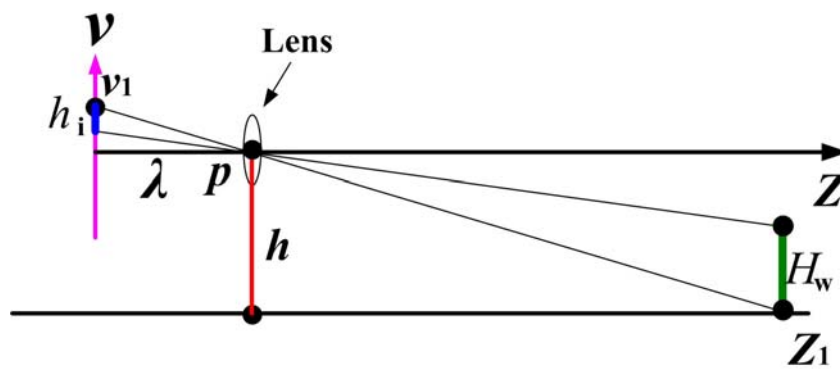
$$w_i = \lambda \frac{W_w}{Z_1} \quad (4.3)$$



(a)



(b)



(c)

Fig. 4-1. (a) The projection of an obstacle in the image. (b) The projection of a pattern in the image. (c) The relation between H_w and h_i .

4.2.2 Adaptive Edge Detection

The proposed vehicle detection approach adopts the feature that the contours of vehicles are mostly made of horizontal and vertical lines. So edges of an object in the image are detected first with Sobel masks.

The result of edge detection is closely related to thresholds. If the threshold is too low, noise will be generated, which reduces the accuracy and performance of the detection. In contrast, if the threshold is too high, important information may be gone, which also affects the detection results. Furthermore, when the brightness changes from regular to strong illumination, the preset threshold must be adjusted accordingly to prevent errors. The experimental results have discovered the most suitable thresholds under various levels of illumination. Moreover, sampling the images by (4.4) accelerates the acquisition of illumination. With the information, the threshold can be adjusted automatically in different surroundings, meaning the approach of edge detection is adaptable.


$$i_s = \sum_{R_u} \sum_{R_v} f(u, v) \quad (4.4)$$

where $f(u, v)$ is the gray level at point (u, v) in the image.

i_s represents the total gray value of the sampled points, showing the illumination of the surroundings.

R_u and R_v are the sampled points. R_u is taken from every p pixels in the u axis and R_v from every q pixels in the v axis.

4.3 Vehicle Detection Based on Contour Size Similarity

Contour Size Similarity (CSS) is an algorithm with the function of detecting objects similar to rectangles, such as vehicles. Since vehicle sizes are within certain range, estimation of their projective sizes can be fulfilled by geometry projection. If the contour of a detected object

resembles the projective contour of a vehicle, the object is probably a vehicle.

4.3.1 Vehicle Detection Procedures

The main target of the detection is the closest preceding vehicle in the lane of the autonomous vehicle and the cutting-in vehicle. To reduce the detection time, vehicles and obstacles outside the lane of the autonomous vehicle are skipped, because they have little influence on its movement. Therefore, the ROI of vehicle detection is determined to be inside the current lane of the autonomous vehicle. A technique of temporal consistency is generally adopted to make the detection of the target vehicle more robust. For example, the surrounding area of the target vehicle in the previous frame is considered the preset region of vehicle detection (*PROVD*) in the following frame. However, when another vehicle cuts in the lane of the autonomous vehicle to be the new target vehicle, the technique will not be suitable because the position of the new target is not always within *PROVD*. Therefore, in our approach, the search region of vehicles is set to be the lane of autonomous vehicle and the detection is conducted from the near to the far searching for the closest preceding vehicle. When another car cuts in the lane of the autonomous vehicle, this car will be detected first because it becomes the closest vehicle instead. The flowchart of the vehicle detection is shown in Fig. 4-2. As can be seen, the lane detection is followed by the edge detection conducted on the lane regions. The detection of horizontal lines starts upward row by row in the current frame. In each row, the detection is performed rightward to look for neighboring pixels with the same gray level in the thresholded image and count the number of pixels in each horizontal line, which represents the length of the horizontal lines. Once the length of horizontal line approximates a vehicle width, the detection of vertical line starts upward from the current row and the number of pixels in each vertical line is counted. Rectangle-like obstacles project approximately horizontal and vertical edges on the image. If these

horizontal and vertical edges form a joint contour, the object may be a vehicle. Then, its size is compared with the estimated sizes of vehicles. If they match, the object is recognized as a vehicle.

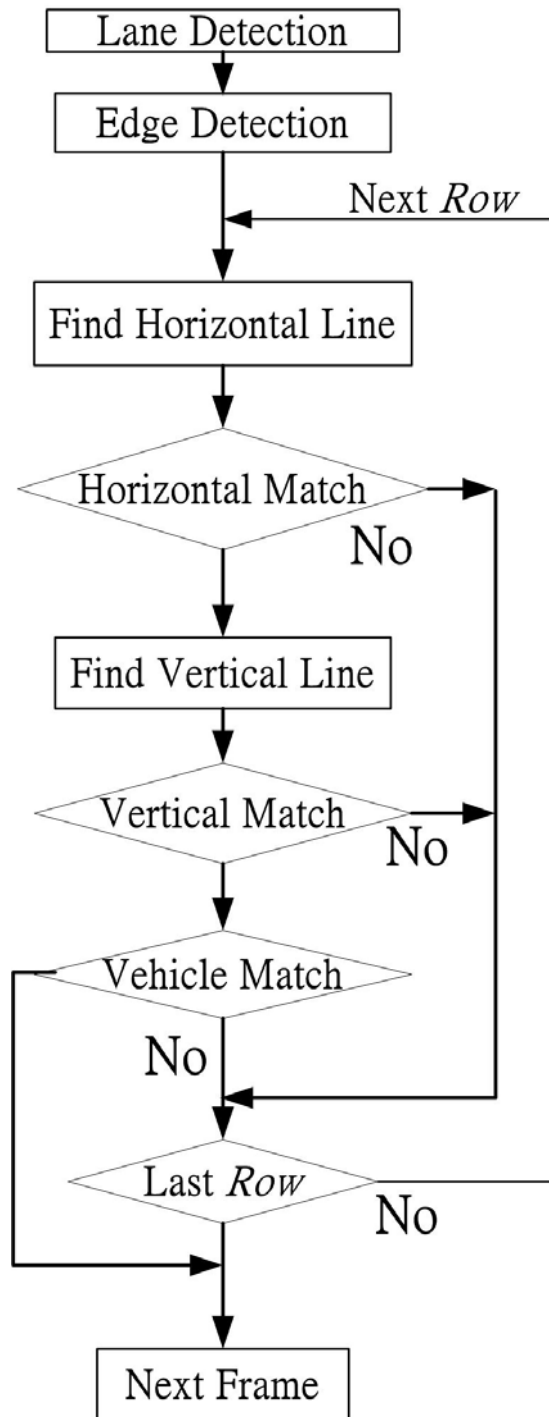


Fig. 4-2. Vehicle detection flowchart.

4.3.2 Fuzzy Match

The detected heights and widths of an object are compared with the estimated ones of a vehicle projection. In Fig. 4-3, A_w is a rectangular obstacle, whose projection on the image is A_i . In Fig. 4-3(a), the width of A_i is A_h , and the height is A_v . The size of A_i changes with the range between the camera and A_w . In Fig. 4-3(b), B_w is a vehicle, whose projection is B_i in the image. The width of B_i is B_h , with B_v being the height. If an image includes an object whose dimensions match both B_i and the projective position, then the object is considered a vehicle.

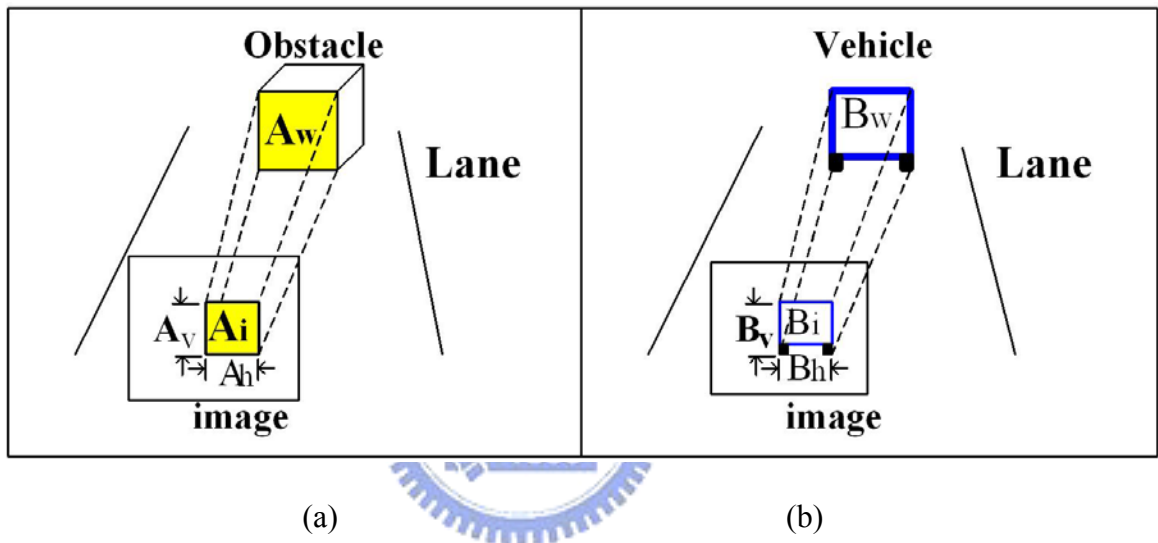


Fig. 4-3. (a) Size of the obstacle projected on the image. (b) Size of the vehicle projected on the image.

B_h and B_v can be estimated by (4.2) and (4.3). Once A_i is found, A_h is compared with B_h and A_v with B_v , respectively. If the width and height of A_i are similar to those of B_i , A_i may be the vehicle B_i . Some fuzzy sets shown in (4.5)-(4.8) are proposed to express their degree of similarity. In (4.5), F_h represents the degree of similarity between the horizontal width of A_i and B_i , and F_v denotes that between the vertical length of A_i and B_i as shown in (4.6). Equations (4.7)-(4.8) are their membership functions. In Fig. 4-4(a), A_h denotes the width of the detected object while $u_{Fh}(A_h)$ represents the degree of similarity between A_h and the vehicle width, B_h . With the growth of A_h , $u_{Fh}(A_h)$ presents three changing phases of being

rising, declining and flat. 1) The rising phase: B_{hs} represents the widths of small cars. When $A_h = B_{hs}$, $u_{Fh}(A_h)$ is defined as h_1 . If A_h is larger than B_{hs} , $u_{Fh}(A_h)$ rises accordingly. 2) The declining phase: B_h denotes the width of a medium vehicle. When $A_h = B_h$, $u_{Fh}(A_h)$ is 1, the largest value of $u_{Fh}(A_h)$. If A_h is larger than B_h , $u_{Fh}(A_h)$ declines. 3) The flat phase: the width of a large-sized vehicle is named B_{hc} . On condition that $A_h = B_{hc}$, $u_{Fh}(A_h)$ is defined as h_2 . If $A_h > B_{hc}$, $u_{Fh}(A_h)$ stays unchanged as h_2 . The reason to keep $u_{Fh}(A_h)$ stable in this phase is that the width of the detected object appearing larger than that of a large-sized vehicle may be because of the overlap of objects. Therefore, the detected object may still be part of the vehicle, and $u_{Fh}(A_h)$ will not drop under the situation. Likewise, A_v denotes the height of the detected object while $u_{Fv}(A_v)$ represents the degree of similarity between A_v and a vehicle height, B_v . Fig. 4-4(b) reveals a similar relation between A_v and $u_{Fv}(A_v)$.

$$F_h = \{A_h, \mu_{Fh}(A_h) \mid A_h \in N\} \quad (4.5)$$

where F_h is a fuzzy set, representing the degree of similarity between the horizontal width of A_i and B_i . $\mu_{Fh}(A_h)$ is the membership function of F_h .

$$F_v = \{A_v, \mu_{Fv}(A_v) \mid A_v \in N\} \quad (4.6)$$

where F_v represents the degree of similarity between the vertical length of A_i and B_i . $\mu_{Fv}(A_v)$ is the membership function of F_v .

$$\mu_{Fh}(A_h) = \begin{cases} 0, & A_h \leq B_{hs} \\ 1 + \left(\frac{1-h_1}{B_h - B_{hs}} \right) (A_h - B_h), & B_{hs} < A_h \leq B_h \\ 1 + \left(\frac{1-h_2}{B_h - B_{hc}} \right) (A_h - B_h), & B_h < A_h \leq B_{hc} \\ h_2, & A_h > B_{hc} \end{cases} \quad (4.7)$$

$$\mu_{F_v}(A_v) = \begin{cases} 0, & A_v \leq B_{vs} \\ 1 + \left(\frac{1-v_1}{B_v - B_{vs}} \right) (A_v - B_{vs}), & B_{vs} < A_v \leq B_v \\ 1 + \left(\frac{1-v_2}{B_v - B_{vc}} \right) (A_v - B_v), & B_v < A_v \leq B_{vc} \\ v_2, & A_v > B_{vc} \end{cases} \quad (4.8)$$

where B_{vs} is the minimum vehicle height.

B_v represents the height of a medium-sized vehicle.

B_{vc} denotes the height of a large-sized vehicle; v_1 and v_2 are constants.

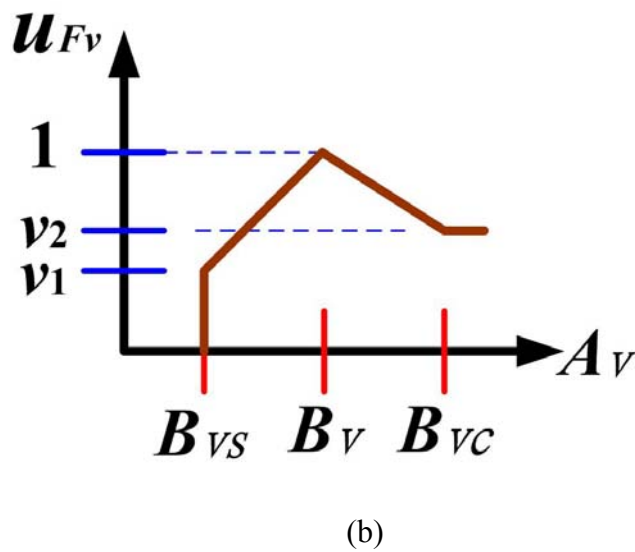
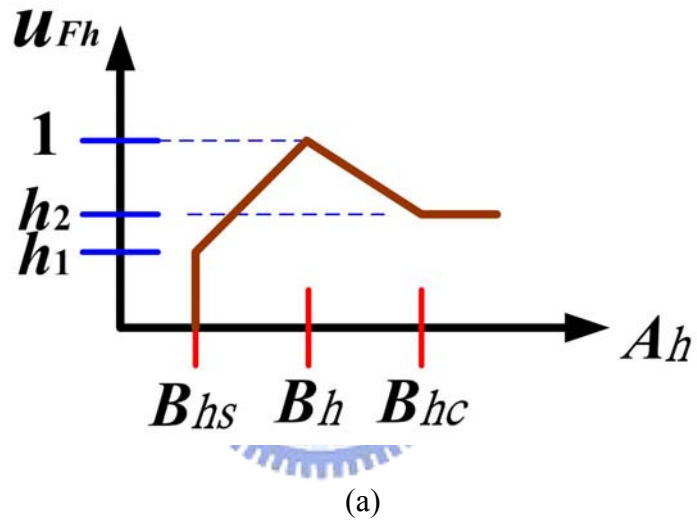


Fig. 4-4. (a) The membership function of F_h (b) The membership function of F_v .

The detection of the target vehicle starts with the search of horizontal lines from left to right side of the image. When a horizontal line exceeding B_{hs} is found, the search of vertical lines starts upwardly from the current row. When the width and height of the detected object is obtained, the fuzzy rules in section 3.3.3 will be applied to identify whether the object is a vehicle.

4.3.3 Vehicle Recognition Based on Fuzzy Rules

The following fuzzy rules can verify the likelihood of A_i being B_i .

- Fuzzy Rule1: If A_h exceeds B_{hs} , then A_i may be B_i , and the degree of horizontal similarity is $\mu_{Fh}(A_h)$.
- Fuzzy Rule2: If A_v is larger than B_{vs} , then A_i may be B_i , and $\mu_{Fv}(A_v)$ is their degree of vertical similarity.

As shown in (4.9), $\mu_{Fhv}(A_h, A_v)$ means the degree of similarity between A_i and B_i . The way to compose two fuzzy sets is to use an algebraic product.

$$\mu_{Fhv}(A_h, A_v) = \mu_{Fh}(A_h) \times \mu_{Fv}(A_v) \quad (4.9)$$

4.3.4 Vehicle Recognition based on a Defuzzifier

The detected object is recognized as a car when both its width and height are larger than the minimum level of a vehicle. Equation (4.10) presents the requirements for objects to be recognized as vehicles.

$$\mu_{Fhv}(A_h, A_v) \geq h_1 \times v_1 \quad (4.10)$$

4.4 Experimental Results

This study utilizes a Hitachi KP-F3 camera equipped in an experimental smart car, Taiwan *its-1*, with a screen resolution of 644×493 , whose every physical pixel size is $7.4(H) \times 7.4(V)$ μm . The camera is mounted at the height of 1.32m. The equipment adopted in the system

includes a PC with CPU Pentium 2.8G and 512MB DRAM. The average processing time of lane detection is less than 9 ms, and edge and vehicle detection takes about 23 ms. Experiments of vehicle detection are conducted in conditions with diverse illumination, roads with patterns, and vehicles cutting in the lane of the autonomous vehicle. The results of vehicle detection are shown as follows.

4.4.1 Vehicle Detection Results

The proposed approach of vehicle detection is applied to situations with regular illumination or strong sunshine, and roads with text as shown in Figs 4-5, 4-6 and 4-7. Figure 4-5 reveals a successful detection of the closest preceding vehicle on the lane of the autonomous vehicle. Even though the bottom part of the vehicle contour is not a straight horizontal line, its shadow below still forms a horizontal line in the image. So the vehicle and its shadow still compose a quasi-rectangular contour in the image.



Fig. 4-5. Vehicle detection with regular illumination.

Figure 4-6 is a road with some patterns, such as lane markings, text markings and crossing line. Patterns on the road do not affect our vehicle detection, because they can not form any vertical edges in the images.

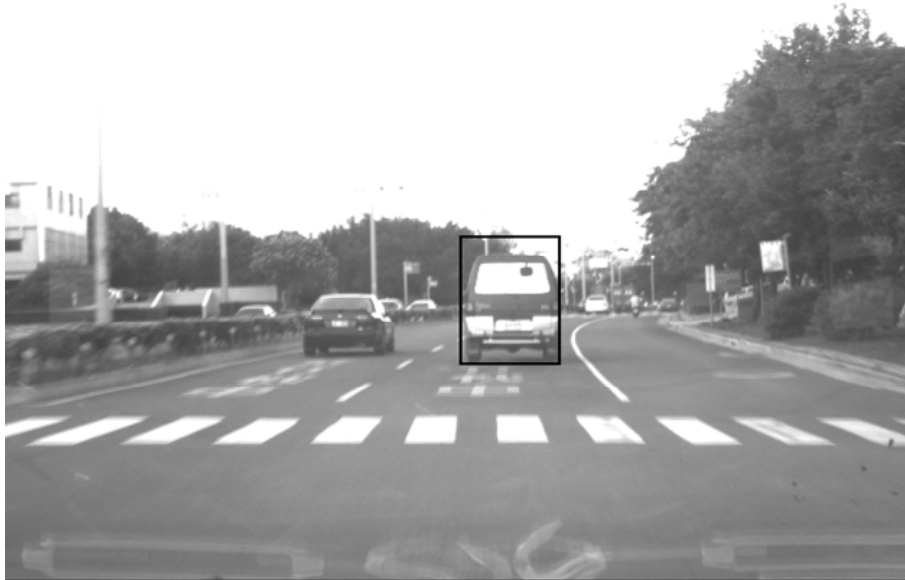


Fig. 4-6. Vehicle detection with patterns on the road.



Fig. 4-7. Vehicle detection under sunny conditions.

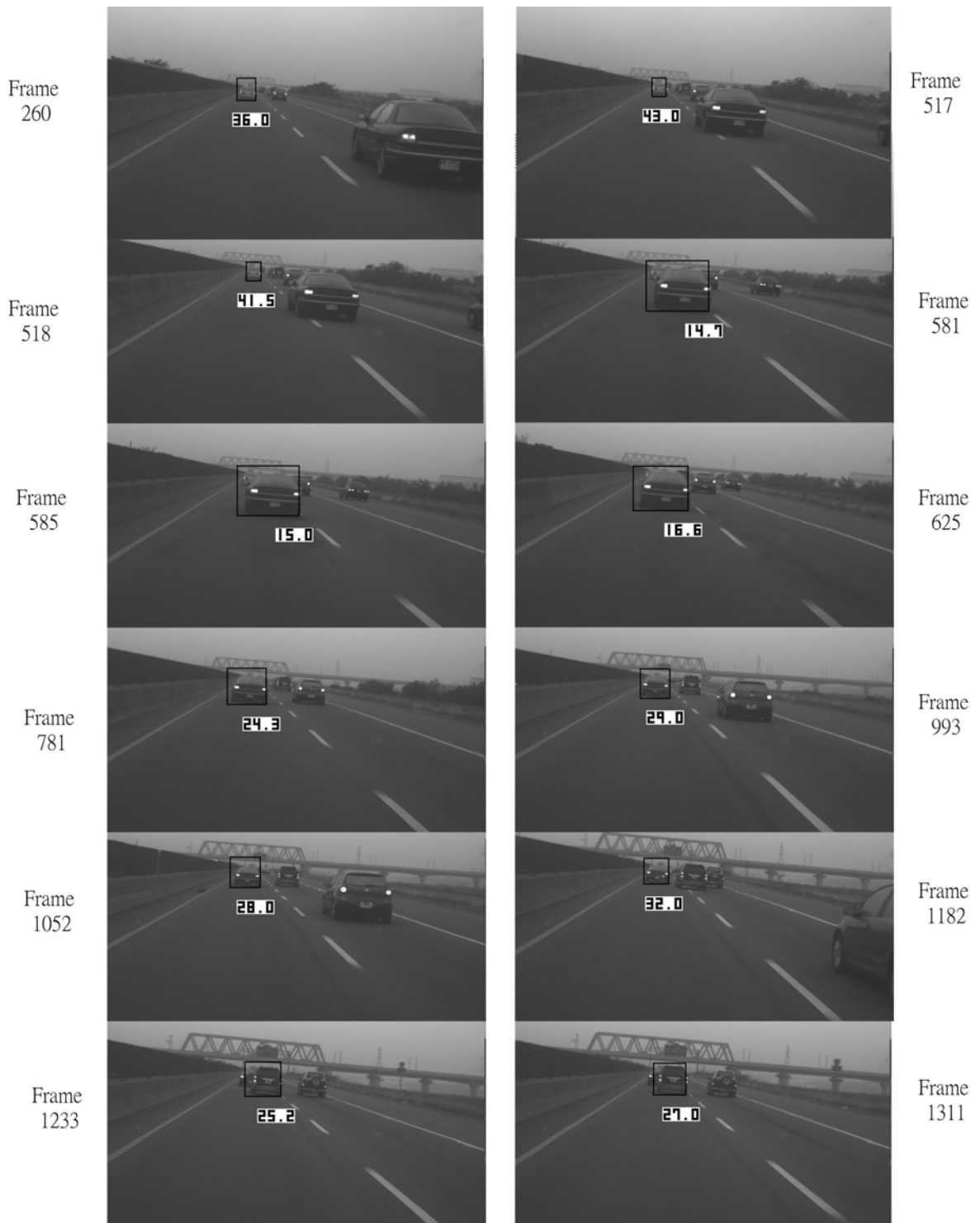


Fig. 4-8. The results of vehicle detection with vehicles cutting in the lane of the autonomous vehicle.

Figure 4-7 displays the experimental results under sunny conditions. Although the reflection of light generated noise, the proposed algorithm still recognized the target vehicle

efficiently in this adverse condition.

Figure 4-8 exhibits detection results of consecutive images. At the bottom of every image is a number showing the distance between the camera and the preceding vehicle computed by (4.1). In frame 518, the range to the closest preceding car was 41.5 meters. In frame 581, the car in the right lane cut in, so the detected distance changed to 14.7 meters. Likewise, the detected range to the preceding vehicle was 32 meters in frame 1182, and became 25.2 meters in frame 1233 when a car cut in.

Figure 4-9 shows results of lane and vehicle detections in the freeway. The distance between the vehicle and the camera is estimated to be 35.5 m.



Fig. 4-9 Results of lane and vehicle detection.

4.4.2 Comparative Analysis

The experimental results were compared with other systems in terms of lane and vehicle detection in Table 4-1 [29][66]. As it can be observed, GOLD [29] adopted a stereo camera,

and the cost is higher than the other two. In computation cost, GOLD could effectively detect lane markings by IPM and black-white-black transitions on the flat roads. Although IPM may require plenty of time for computation, the application of a pre-computed table helps rapidly create top-view images. However, with various road conditions, the vibration of the camera may cause extra mapping distortion and errors. Besides, vehicle detection of GOLD requires a comparison of disparity between two cameras so more time is needed. Sun. et al [66] applied the Gabor filter and SVM (support vector machines) to detect vehicles. These approaches are time-consuming because the algorithms involve high computation complexity. The proposed approach in this study conducts lane detection first and then defines the current lane region as ROI for vehicle detection to achieve real time lane and vehicle detection and reduce errors. Besides, in our vehicle detection, a Kalman filter is designed to process the estimated range between the preceding vehicle and the camera, and to enhance the robustness of range estimation.

Table 4-1 Comparison of approaches in lane and vehicle detection

Approach	Camera Type	Computational Cost	Lane detection		Vehicle detection		
			Straight Roadway	Curvature Roadway	ROI Selection	Vehicle Detection & Cut-in Management	Techniques of Temporal Consistency
GOLD [29]	Stereo	Medium	Good	N/A	N/A	Good	N/A
Sun. et al.[66]	Single	High	N/A	N/A	N/A	Good	N/A
The proposed approach	Single	Low	Good	Good	Within the Lane	Good	Kalman filter

Chapter 5

Conclusion and Future Works

5.1 Range Estimation and Dynamic Calibration

In this study, we have presented several approaches for the estimation of the range between the preceding vehicle and the camera, range errors, the actual height of vehicles and the projective height of the detected vehicles in various positions. The results of error estimation can be adopted as a reference to determine the preset camera parameters, suppress estimation errors and facilitate rapid and accurate estimation of vehicle sizes.

According to the error analyses, the variations of camera tilt and swing angles lead to significant errors in range estimation results. A dynamic calibration approach has been proposed to effectively reduce errors of range estimation. A Kalman filter is also integrated in order to more stably estimate swing angles so that the estimation results can be sufficiently robust and estimation errors can be further reduced. Experimental results demonstrate that our approaches can provide accurate and robust estimations of range and size of target vehicles. The proposed approaches can serve as reference for designers of vision-based driving assistance systems to improve the efficiency of vehicle detection and range estimation.

5.2 Lane detection

To apply lane detection for the guidance of autonomous vehicles and driving assistance system, a variety of road conditions should be considered, such as changes of illumination, a great diversity of road curvature, difference in the configurations of lane markings like

continuous, dashed or occluded road markings. A lane detection system should have high efficiency, robustness, and reliability to make driving at high speed safe.

This study has proposed a rapid computation of lane width to predict the projective positions and widths of lane markings and an approach *LME FSM* is designed to extract lane markings efficiently. A statistical search algorithm is also proposed to correctly and adaptively determine thresholds under various kinds of illumination conditions. Moreover, a dynamic calibration algorithm is applied to update the information of a camera's parameters and lane width. Additionally, a method of fuzzy reasoning is adopted to determine whether the lane marking is continuous, dashed and occluded. Finally, the strategy of the *ROI* is proposed to narrow the search region and make the detection more robust. Experimental results shows that even when obstacles occlude parts of the lane markings or lane markings have complicated curvature, road boundaries still can be reconstructed correctly by B-spline with four segments. In conclusion, even with the information of lanes, there are still many threats from surrounding vehicles and obstacles when driving. Thus, the function of obstacle detection should be combined with lane detection systems to make the guidance of autonomous vehicles and driving assistance systems better in the future.

5.3 Vehicle detection

A real-time obstacle detection system to detect obstacles and vehicles whose shapes are similar to rectangles is presented. When detecting, we start with edge detection, and then identify obstacles and recognize whether they are vehicles according to their contour sizes in the vertical and horizontal edges. Many obstacles can be found in the detection and their distance to the camera can be acquired. With the information of lane detection, the closest preceding car in the lane of the autonomous vehicle can successfully be detected in real time. This work can be applied in vehicle detector for the driving assistance system.

5.4 Future Works

Some directions for future study are recommended below:

- (1) In the future, simultaneous detections of several lanes and vehicles will be conducted and the obtained information will be applied to the throttle and brake systems of vehicles to support the automatic driving of intelligent autonomous vehicles.
- (2) The changeable illumination and weather condition of outdoor surroundings and the high speed of vehicle movements increase the difficulty of lane and vehicle detection. More robust and rapid approaches should be proposed to make the driving assistance systems real-time and adaptive.
- (3) Besides vehicles, pedestrians, motorcycles and other obstacles also can affect driving safety. Therefore, techniques for detecting those objects should be developed to increase the feasibility of the driving assistance system and improve driving safety.



APPENDIX A

Relation of Projected Width and v -coordinate

If the lane width is W_{wL} and the projective lane width on the v -coordinate is $w_L(v)$, then (A-1) can be obtained from (1) and (2). (A-2) means the first derivative for v to $w_L(v)$. Let $\xi = (\pi/2 - \alpha)$, and $\tau = \tan^{-1}(v/\lambda)$. Then (A-4) and (A-5) can be derived from (A-2) and (A-3). Since the camera was placed in a vehicle to detect the lane, when α is large, the farther part of the lane would not appear in the image. Therefore, α is usually between 0-6 degrees. In the study, let the tilt angle $\alpha < 10^\circ$, and then the value of ξ will be larger than 80° , and they are substituted in (A-6)(A-7). Next, they are applied to (A-5) to obtain (A-8) and (A-9). (A-9) shows the first derivative of $w_L(v)$ is a constant. The relation between $w_L(v)$ and v can be expressed by a linear equation as (A-10).

$$w_L(v) = \frac{W_{wL} \times \lambda}{h \cdot \tan\left(\left(\frac{\pi}{2} - \alpha\right) - \tan^{-1}\left(\frac{v}{\lambda}\right)\right)} \quad (\text{A-1})$$

$$\frac{dw_L(v)}{dv} = \frac{W_{wL} \times \lambda}{h} \times \left(d \cot\left(\left(\frac{\pi}{2} - \alpha\right) - \tan^{-1}\left(\frac{v}{\lambda}\right)\right) / dv \right) \quad (\text{A-2})$$

$$\cot(\xi - \tau) = \frac{1 + \tan(\xi) \times \tan(\tau)}{\tan(\xi) - \tan(\tau)} \quad (\text{A-3})$$

$$\frac{dw_L(v)}{dv} = \frac{W_{wL} \times \lambda}{h} \times \left(\kappa \times \frac{d\omega}{dv} - \omega \times \frac{d\kappa}{dv} \right) / \kappa^2 \quad (\text{A-4})$$

where $\omega = 1 + \tan(\xi) \times \tan(\tau)$; $\kappa = \tan(\xi) \times \tan(\tau)$.

$$\frac{dw_L(v)}{dv} = \frac{W_{WL} \times \lambda}{h} \times \frac{\left(\tan(\xi) - \frac{v}{\lambda}\right) \times \frac{\tan(\xi)}{\lambda} - \left(1 + \tan(\xi) \times \frac{v}{\lambda}\right) \times \left(-\frac{1}{\lambda}\right)}{\left(\tan(\xi) - \frac{v}{\lambda}\right)^2} \quad (\text{A-5})$$

$$\tan(\xi) \gg \frac{v}{\lambda} \quad (\text{A-6})$$

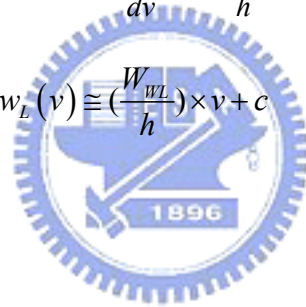
where $\xi > 80^\circ$.

$$\tan(\xi) \times \frac{\tan(\xi)}{\lambda} \gg \left(\frac{v}{\lambda^2} \times \tan(\xi) + \frac{1}{\lambda}\right) \quad (\text{A-7})$$

$$\frac{dw_L(v)}{dv} \approx \frac{W_{WL} \times \lambda}{h} \times \frac{(\tan(\xi)) \times \frac{\tan(\xi)}{\lambda}}{(\tan(\xi))^2} \quad (\text{A-8})$$

$$\frac{dw_L(v)}{dv} \approx \frac{W_{WL}}{h} \quad (\text{A-9})$$

$$w_L(v) \cong \left(\frac{W_{WL}}{h}\right) \times v + c \quad (\text{A-10})$$



APPENDIX B

Adaptation to Illumination Conditions

The proposed statistical search algorithm determines G_{gH} , G_{gL} , G_{mH} , and G_{mL} in the region of interest (*ROI*) for detecting lane markings. The procedures for determining the thresholds in each row are given as follows:

Step 1) *Setting search windows*: Set a window in each N -th row to search for G_{gH} , G_{gL} , G_{mH} , and G_{mL} . The width of the search window on the N -th row, $W_w(N)$, is shown as (B-1). Here the left border of the search window is also the left border of the search region of the lane marking on the N -th row.

$$W_w(N) = \begin{cases} 5 \times w_m(N), & \text{if } (S_R \geq 5 \times w_m(N)) \\ S_R, & \text{otherwise} \end{cases} \quad (\text{B-1})$$

where $w_m(N)$ is the estimated width of the lane marking on the N -th row. S_R denotes the search region.

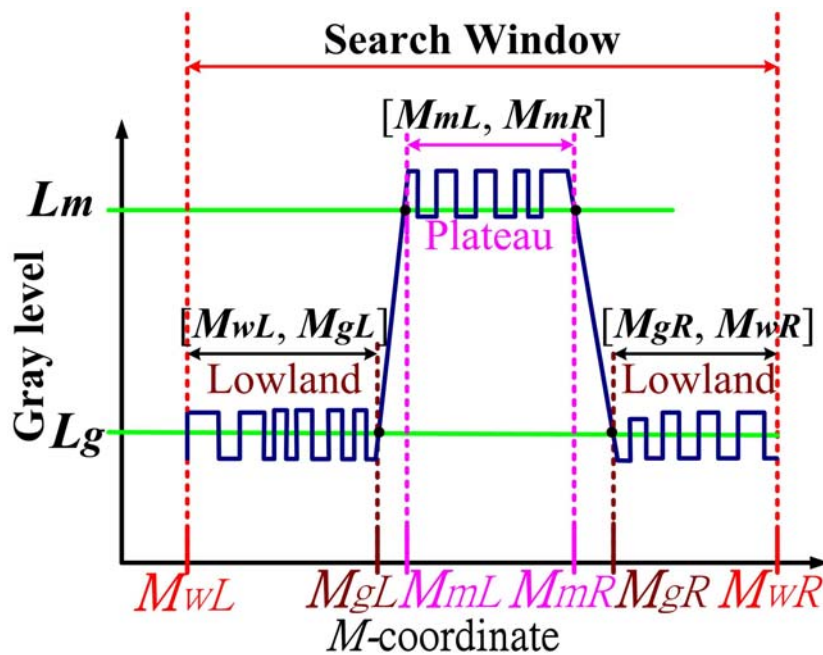


Fig. B-1. The gray level distribution with a row of lane marking in the search window.

Step 2) *Finding zone of lane marking and ground in the window*: Since the gray levels of lane markings are obviously higher than those of the ground's, the distribution of gray levels in a search window can be divided into three main zones if a row of lane markings appears close to the center of the search window. The three main zones in sequence are a lowland, a plateau, and again a lowland of gray level groups. These three zones can be determined according to the representative bright and dark levels of the lane markings and the ground, which are respectively the average gray levels of lane markings and the ground. Let G denote the gray levels in M -coordinate in the search window, as shown in (B-2). Compute the pixel number of the lane marking and the ground in the window, respectively A_m and A_g , by (B-3). Let a set, L , be the ordered gray levels of the pixels in G , which are arranged from large to small as in (B-4), where L_1, L_{A_w} respectively represent the highest and lowest gray level in G . L_m is the average gray levels of lane markings, i. e. the average of the brightest A_m pixels with the highest gray level among the set L . L_g is the average gray levels of the ground, also the average of the darkest A_g pixels with the lowest gray level among L as shown in (B-5). After finding the representative bright and dark levels of the lane markings and the ground, three zones of interest can be found based on the following definitions. In the search window, the left and right borders of the lane marking, M_{mL} and M_{mR} , is respectively defined as the leftest and rightest pixel whose gray levels are larger than L_m . The left border of ground, M_{gL} , is defined as the pixel whose gray level is lower than L_g and being closest to M_{mL} . The right border of the ground, M_{gR} , is defined as the pixel with gray level lower than L_g and closest to M_{mR} . Figure B-1 shows the gray level of each pixel in G when a row of the lane marking exists in the search window. As can be seen, the plateau zone, $[M_{mL}, M_{mR}]$ of the lane marking in G can be found by L_m , and the lowland zone, union $[M_{wL}, M_{gL}]$ and $[M_{gR}, M_{wR}]$ of the ground by L_g .

$$G = \{G_M \mid M \in [M_{wL}, M_{wR}]\} \quad (B-2)$$

where G_M denotes the gray level in M -coordinate. M_{wL} and M_{wR} respectively represent the left and right boundaries of the search window.

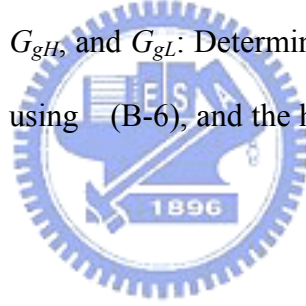
$$A_m = r_{mw} \times A_w; r_{mw} = \frac{w_m(N)}{W_w(N)}; A_g = A_w - A_m; \quad (\text{B-3})$$

where A_w is the number of pixels in the search window; r_{mw} denote the ratio of $w_m(N)$ to $W_w(N)$.

$$L = \{L_j \mid j \in [1, A_w]\} \quad (\text{B-4})$$

$$L_m = \frac{1}{A_m} \sum_{j=1}^{A_m} L_j; \quad L_g = \frac{1}{A_g} \sum_{j=A_m+1}^{A_w} L_j \quad (\text{B-5})$$

Step 3) Determining G_{mH} , G_{mL} , G_{gH} , and G_{gL} : Determine the highest and lowest gray levels in the plateau zone, G_{mH} and G_{mL} , using (B-6), and the highest and lowest in the lowland zone, G_{gH} , and G_{gL} by (B-7).



$$\begin{aligned} G_{mH} &= \max \{G_M \mid M \in [M_{mL}, M_{mR}]\}; \\ G_{mL} &= \min \{G_M \mid M \in [M_{mL}, M_{mR}]\} \end{aligned} \quad (\text{B-6})$$

$$\begin{aligned} G_{gH} &= \max \{G_M \mid M \in \{[M_{wL}, M_{gL}] \cup [M_{gR}, M_{wR}]\}\}; \\ G_{gL} &= \min \{G_M \mid M \in \{[M_{wL}, M_{gL}] \cup [M_{gR}, M_{wR}]\}\}; \end{aligned} \quad (\text{B-7})$$

Step 4) *Verifying* G_{mH} , G_{mL} , G_{gH} , and G_{gL} : Check whether the determined G_{gH} , G_{gL} , G_{mH} , and G_{mL} are correct by verifying that G_{gH} is smaller than G_{mL} . If so, substitute G_{gH} , G_{gL} , G_{mH} , G_{mL} in (11) to obtain the corresponding D_{g1} , D_{g2} , D_{g12} on this row and go to step 6. Otherwise, go to step 5.

Step 5) Checking whether S_R is completely searched: If so, let D_{g1} , D_{g2} , D_{g12} in this row be

the same as those in the previous row and go to step 6. Otherwise, shift the window rightward for the distance of $w_m(N)$ and return to step 2.

Step 6) Terminate the determination process of the N -th row, and export the results of G_{mH} , G_{mL} , G_{gH} , and G_{gL} .



References

- [1] Z. Sum, G. Bebis, and R. Miller, "On-Road Vehicle Detection: A Review," *IEEE Trans. Pattern Analysis and Machine Intelligence*, vol. 28, no. 5, pp. 694-711, May 2006.
- [2] W. Jones, "Keeping cars from Crashing," *IEEE Spectrum*, vol. 38, no 9, pp. 40-45, 2001.
- [3] W. Jones, "Building Safer Cars," *IEEE Spectrum*, vol. 39, no 1, pp. 82-85, 2002.
- [4] Bing-Fei Wu, Chuan-Tsai Lin, and Yen-Lin Chen, "Dynamic Calibration and Occlusion Handling Algorithms for Lane Tracking," *IEEE Trans. Industrial Electronics*, vol 56, No 5, pp. 1757-1773, May 2009.
- [5] Yen-Lin Chen, Bing-Fei Wu, Chuan-Tsai Lin, Chung-Jui Fan, and Chih-Ming Hsieh, "Real-time Vision-based Vehicle Detection and Tracking on a Moving Vehicle for Nighttime Driver Assistance," accepted for publication in *International Journal of Robotics and Automation*.
- [6] Bing-Fei Wu, Chuan-Tsai Lin, and Chao-Jung Chen, "Real-time Lane and Vehicle Detection Based on a Single Camera Model," accepted for publication in *International Journal of Computers and Applications*.
- [7] Bing-Fei Wu and Chuan-Tsai Lin, "Real-Time Fuzzy Vehicle Detection Based on Contour Size Similarity," *Int. J. Fuzzy Systems*, vol. 7, No. 2, pp. 54-62, June 2005.
- [8] Bing-Fei Wu, Chuan-Tsai Lin, and Yen-Lin Chen, "Range and Size Estimation Based on a Coordinate Transformation Model for Driving Assistance Systems," accepted for publication in *IEICE Transactions on Information and Systems*.
- [9] Y. Chen, "Highway Overhead Structure Detection Using Video Image Sequences," *IEEE Transactions on Intell. Trans. Syst.*, vol. 4, no.2, pp. 67-77, 2003.
- [10] E. Segawa, M. Shiohara, S. Sasaki, N. Hashiguchi, T. Takashima, and M. Tohno, "Preceding Vehicle Detection Using Stereo Images and Non-scanning Millimeter-Wave Radar," *IEICE Trans D: Information*, E89-D, pp. 2101 - 2108, July 2006.
- [11] N. Hautiere, R. Labayrade, and D. Aubert, "Estimation of the Visibility Distance by Stereovision: A Generic Approach," *IEICE Trans D: Information*, E89-D, pp. 2084 -

2091, July 2006.

- [12] S. Nedevschi, R. Danescu, D. Frentiu, T. Marita, F. Oniga, C. Pocol, R. Schmidt, T. Graf, “High accuracy stereo vision system for far distance obstacle detection,” in *Proc. IEEE Intelligent Vehicles Symp.*, pp. 292 – 297, June 2004.
- [13] L. L. Wang and W. H. Tsai, “Camera Calibration by Vanishing Lines for 3-D Computer Vision,” *IEEE Trans. Pattern Analysis and Machine Intelligence*, vol. 13, no. 4, pp. 370-376, 1991.
- [14] T. N. Schoepflin and D. J. Dailey, “Dynamic Camera Calibration of Roadside Traffic Management Cameras for Vehicle Speed Estimation,” *IEEE Transactions on Intell. Trans. Syst.*, vol. 4, no.2, pp. 90-98, 2003.
- [15] Y. M. Liang, H. R. Tyan, S. L. Chang, H. Y. M. Liao, and S. W. Chen, “Video Stabilization for a Camcorder Mounted on a Moving Vehicle,” *IEEE Transactions on Vehicular Technology*, vol. 53, no.6, pp. 1636-1648, 2004.
- [16] Y. Hwang, J. Seo, and H. Hong, “Key-Frame Selection and an LMedS-Based Approach to Structure and Motion Recovery,” *IEICE Trans D: Information*, E91-D, pp. 114 - 123, Jan. 2008.
- [17] J. Wang, F. Shi, J. Zhang and Y. Liu, “A new calibration model of camera lens distortion,” *Pattern Recognition*, vol. 41, Issue 2, pp. 607-615, Feb. 2008.
- [18] B. W. He and Y. F. Li, “Camera calibration from vanishing points in a vision system,” *Optics & Laser Technology*, vol. 40, Issue 3, pp. 555-561, April 2008.
- [19] K. T. Song and J. C. Tai, “Dynamic Calibration of Pan–Tilt–Zoom Cameras for Traffic Monitoring,” *IEEE Transactions on Systems, Man and Cybernetics, Part B.*, vol. 36, pp. 1091-1103, Oct. 2006.
- [20] A. Yilmaz, X. Li, and M. Shah, “Contour-Based Object Tracking with Occlusion Handling in Video Acquired Using Mobile Cameras,” *IEEE Trans. Pattern Analysis*

and Machine Intelligence, vol. 26, no. 11, pp. 1531-1536, 2004.

- [21] S. F. Lin, J. Y. Chen, and H. X. Chao, "Estimation of Number of People in Crowded Scenes Using Perspective Transformation," *IEEE Trans. Syst., Man, Cybern. A*, vol. 31, pp. 645-654, 2001.
- [22] C. C. C. Pang, W. W. L. Lam, and N. H. C. Yung, "A Novel method for resolving vehicle occlusion in a monocular traffic-image sequence," *IEEE Trans. Intelligent Transport. Syst.*, vol. 5, no. 3, pp. 129-141, 2004.
- [23] A. Broggi, M. Bertozzi, Lo Guarino, C. Bianco, and A. Piazzzi, "Visual perception of obstacle and vehicles for platooning," *IEEE Trans. Intelligent Transport. Syst.*, vol. 1, no. 3, pp. 164-176, 2000.
- [24] Y. L. Chen, Y. H. Chen, C. J. Chen, and B. F. Wu, "Nighttime Vehicle Detection for Driver Assistance and Autonomous Vehicles", in *Proc. IAPR International Conference on Pattern Recognition*, vol.1, pp. 687-690, 2006.
- [25] A. Hidaka, K. Nishida, and T. Kurita, "Object Tracking by Maximizing Classification Score of Detector Based on Rectangle Features," *IEICE Trans. Inf. & Syst.*, vol.E91-D, no. 8, pp. 2163-2170, Aug. 2008.
- [26] E. D. Dickmanns and B. D. Mysliwetz, "Recursive 3-D road and relative ego-state recognition," *IEEE Trans. Pattern Anal. Mach. Intell.*, vol. 14, no. 2, pp. 199-213, Feb. 1992.
- [27] E. D. Dickmanns and V. Graefe, "Dynamic monocular machine vision," *Machine Vision and Applications*, vol. 1, pp. 223-240, 1988.
- [28] E. D. Dickmanns and V. Graefe, "Applications of dynamic monocular machine vision," *Machine Vision and Applications*, vol. 1, pp. 241-261, 1988.
- [29] M. Bertozzi and A. Broggi, "GOLD: A parallel real-time stereo vision system for generic obstacle and lane detection," *IEEE Trans. on Image Processing*, vol. 7, pp.

62-81, Jan. 1998.

- [30] M. Bertozzi and A. Broggi, "Vision-Based Vehicle Guidance," *Computer*, vol. 30, pp. 49-55, July. 1997.
- [31] C. Kreucher and S. Lakshmanan, "LANA: A Lane Extraction Algorithm that Uses Frequency Domain Features," *IEEE Trans. on Robotics and Automation*, vol. 15, April 1999.
- [32] V. Kastrinaki, M. Zervakis, and K. Kalaizakis, "A survey of video processing techniques for traffic applications," *Image Vis. Comput.*, vol. 21, no. 4, pp. 359-381, Apr. 2003.
- [33] J. C. McCall and M. M. Trivedi, "Video-based lane estimation and tracking for driver assistance: survey, system, and evaluation," *IEEE Trans. Intell. Transp. Syst.*, vol. 7, no. 1, pp.20-37, March 2006.
- [34] B. F. Wu, and C. T. Lin, "Robust Image Measurement and Analysis Based on Perspective Transformations," in *Proc. IEEE Syst., Man, Cybern. Symp.*, pp.2390-2395, Oct. 2006.
- [35] S. Nedeveschi, C. Vancea, T. Marita, and T. Graf, "Online Extrinsic Parameters Calibration for Stereovision Systems Used in Far-Range Detection Vehicle Applications," *IEEE Trans. Intell. Transp. Syst.*, vol. 8, pp.651-660, Dec. 2007.
- [36] Y. Motai and A. Kosaka, "Hand-Eye Calibration Applied to Viewpoint Selection for Robotic Vision," *IEEE Trans. Ind. Electron.*, vol. 54, no. 2, pp. 3731-3741, Oct. 2008.
- [37] Bing-Fei Wu and Chuan-Tsai Lin, "Robust Lane Detection and Tracking for Driving Assistance Systems," in *Proc. IEEE Syst., Man, Cybern. Symp.*, pp. 3848-3853, Oct. 2007.
- [38] M. Chen, T. Jochem, and D. Pomerleau, "AURORA: A Vision-Based Roadway Departure Warning System," in *Proc. IEEE Intelligent Robots Systems*, pp. 243-248,

1995.

- [39] K. Kluge and S. Lakshmanan, "A deformable-template approach to lane detection," in *Proc. IEEE Intelligent Vehicle Symp.*, 1995, pp. 54 – 59.
- [40] A. Takahashi, Y. Ninomiya, M. Ohta, and K. Tange, "A Robust Lane Detection using Real-time Voting Processor," in *Proc. IEEE on Intelligent Transportation Systems*, pp. 577-580, Oct. 1999.
- [41] J. Goldbeck and B. Huertgen, "Lane Detection and Tracking by Video Sensors," in *Proc. IEEE/IEEJ/JSAI International Conference on Intelligent Transportation Systems*, pp. 74-79, Oct. 1999.
- [42] P. Jeong and S. Nedeveschi, "Local Difference Probability (LDP)-Based Environment Adaptive Algorithm for Unmanned Ground Vehicle" *IEEE Trans. on Intell. Trans. Syst.*, vol. 7, no.3, pp. 282-292, Sep. 2006.
- [43] P. Jeong and S. Nedeveschi, "Efficient and robust classification method using combined feature vector for lane detection," *IEEE Trans. Circuits and Systems for Video Technology*, vol. 15, pp. 528-537, April 2005.
- [44] Y. He, H. Wang, and B. Zhang. "Color-Based Road Detection in Urban Traffic Scenes," *IEEE Trans. on Intell. Transp. Syst.*, vol. 5, no.4, pp. 309-318, Dec. 2004.
- [45] B. Fardi and G. Wanielik, "Hough transformation based approach for road border detection in infrared images," in *Proc. IEEE Intelligent Vehicles Symp.*, Parma, Italy, June 2004, pp. 549-554.
- [46] C. R. Jung and C. R. Kelber, "Lane following and lane departure using a linear-parabolic model," *Image and Vision Computing*, vol 23, pp. 1192-1202, Nov. 2005.
- [47] A. Broggi, M. Cellarario, P. Lombardi, and M. Porta, "An evolutionary approach to visual sensing for vehicle navigation," *IEEE Trans. Ind. Electron.*, vol. 50, no. 1, pp.

18-29, Feb. 2003.

- [48] R. Arnay, L. Acosta, M. Sigut, and J. Toledo, "Ant colony optimisation algorithm for detection and tracking of non-structured roads," *Electronics Letters*, vol 44, pp. 725-727, June 2008.
- [49] C. F. Juang, C. M. Lu, C. Lo, and C. Y. Wang, "Ant Colony Optimization Algorithm for Fuzzy Controller Design and Its FPGA Implementation," *IEEE Trans. Ind. Electron.*, vol. 55, no. 3, pp. 1453-1462, Mar. 2008.
- [50] K. Sundareswaran, K. Jayant, and T. N. Shanavas, "Inverter Harmonic Elimination Through a Colony of Continuously Exploring Ants," *IEEE Trans. Ind. Electron.*, vol. 54, no. 5, pp. 2558-2565, Oct. 2007.
- [51] C. D'Cruz and J. J. Zou, "Lane detection for driver assistance and intelligent vehicle applications," in *Proc. International Symposium on Communications and Information Technologies*, pp. 1291-1296, Oct. 2007.
- [52] T. Liu, N. Zheng, H. Cheng, and Z. Xing, "A novel approach of road recognition based on deformable template and genetic algorithm," in *Proc. IEEE Intell. Transp. Syst.*, pp. 1251-1256, Oct. 2003.
- [53] S. Sehestedt, S. Kodagoda, A. Alempijevic, and G. Dissanayake, "Robust lane detection in urban environments," in *Proc. IEEE Intelligent Robots and systems*, pp. 123-128, Oct. 2007.
- [54] C. Caraffi, S. Cattani, P. Grisleri, "Off-Road Path and Obstacle Detection Using Decision Networks and Stereo Vision," *IEEE Trans. Intell. Transp. Syst.*, vol. 8, pp.607-618, Dec. 2007.
- [55] Q. Li, N. Zheng, and H. Cheng, "Springrobot A Prototype Autonomous Vehicle and Its Algorithms for Lane Detection," *IEEE Trans. on Intell. Transp. Syst.*, vol. 5, no.4, pp. 300-308, Dec. 2004.

- [56] H. Y. Cheng, B. S. Jeng, P. T. Tseng, and K. C. Fan, "Lane Detection With Moving Vehicles in the Traffic Scenes," *IEEE Trans. on Intell. Trans. Syst.*, vol. 7, no.4, pp. 571-582, Dec. 2006.
- [57] Y. Wang, D. Shen, and E. K. Teoh, "Lane detection using spline model," *Pattern Recognition Letters*, vol.21 , pp. 677-689, July 2000.
- [58] H. Lin, S. Ko, W. shi, Y. Kim, and H. Kim, "Lane departure identification on highway with searching the region of interest on hough space," in *Proc. International Conference on Control, Automation and Systems*, pp.1088-1091, Oct. 2007.
- [59] R. Chapuis, R. Aufrere, and F. Chausse, "Accurate Road following and Reconstruction by Computer Vision," *IEEE Trans. on Intelligent Transportation Systems*, vol. 3, Dec. 2002.
- [60] M. Bertozzi and A. Broggi, and A. Fascioli, "Obstacle and lane detection on ARGO autonomous vehicle," in *Proc. IEEE Intelligent Transportation System Conf. '97*, Boston, MA. pp. 1010-1015, 1997.
- [61] M. Zayed and J. Boonaert. "Obstacles detection from disparity properties in a particular Stereo vision system configuration," in *Proc. IEEE Intelligent Transportation Systems*, pp. 311-316, 2003.
- [62] M. Bertozzi, A. Broggi, M. Cellario, A. Fascioli, P. Lombardi, and M. Porta, "Artificial vision in road vehicles," in *Proc. IEEE*, 2002 , pp.1258 – 1271.
- [63] J. Chu, L. Ji, L. Guo, B. Li, and R. Wang, "Study on method of detecting preceding vehicle based on monocular camera," in *Proc. IEEE Intelligent Vehicles Symp.*, Parma, Italy, pp. 750 – 755, June 2004.
- [64] U. Franke and S. Heinrich, "A Study on Recognition of Road Lane and Movement of Vehicles using Vision System," *SICE*, Nagoya, pp. 38-41, July 2001.
- [65] Z. Sum, G. Bebis, and R. Miller, "Monocular Precrash Vehicle Detection: Features and

- Classifiers,” *IEEE Trans. on Image Processing*, vol. 15, no. 7, pp. 2019-2034, July 2006.
- [66] Z. Sum, G. Bebis, and R. Miller, “On-Road Vehicle Detection Using Evolutionary Gabor Filter Optimization,” *IEEE Trans. Intell. Transp. Syst.*, vol. 6, no. 2, pp. 252-260, June 2005.
- [67] U. Franke and S. Heinrich, “Fast Obstacle Detection for Urban Traffic Situations,” *IEEE Trans. Intell. Trans. Syst.*, vol. 3, pp. 173-181, Sept. 2002.
- [68] U. Franke, “Real-time stereo vision for urban traffic scene understanding,” in *proc. IEEE Intelligent Vehicles*. Detroit, MI, pp. 273-278, Oct. 2000.
- [69] M. Watanabe, N. Takeda, and K. Onoguchi, “A Moving Object Recognition Method by Optical Flow Analysis,” in *Proc. ICPR*, pp. 528-533, 1996.
- [70] B. F. Wu and C. T. Lin, “A Fuzzy Vehicle Detection Based on Contour Size Similarity,” in *Proc. IEEE Intelligent Vehicles Symp.*, pp. 495-500, June 2005.
- [71] B. F. Wu, C.T. Lin, and C. J. Chen, “A Fast Lane and Vehicle Detection Approach for Autonomous Vehicles,” in *Proc. the 7th IASTED International Conference Signal and Image Processing*, pp. 306-310, Aug. 2005.
- [72] H. Sawano and M. Okada, “A Road Extraction Method by an Active Contour Model with Inertia and Differential Features,” *IEICE Trans. Inf. & Syst.*, vol.E89-D, no. 7, pp. 2257-2267, July 2006.
- [73] K. Sakurai, S. Kyo, and S. Okazaki, “Overtaking Vehicle Detection Method and Its Implementation Using IMAPCAR Highly Parallel Image Processor,” *IEICE Trans. Inf. & Syst.*, vol.E91-D, no. 7, pp. 1899-1905, July 2008.
- [74] S. K. Joo, Y. Kim, S. I. Cho, K. Choi, and K. Lee, “Traffic Light Detection Using Rotated Principal Component Analysis for Video-Based Car Navigation System,” *IEICE Trans. Inf. & Syst.*, vol.E91-D, no. 12, pp. 2884-2887, Dec. 2008.

- [75] K. Kanatani, Y. Sugaya, and H. Ackermann, “Uncalibrated Factorization Using a Variable Symmetric Affine Camera,” *IEICE Trans. Inf. & Syst.*, E90-D, pp. 851 – 858, May 2007.
- [76] M. Morimoto and K. Fujii, “A Flexible Gaze Detection Method Using Single PTZ Camera,” *IEICE Trans D: Information*; E90-D: 199 – 207, Jan. 2007.
- [77] H. Y. Lin and J. H. Lin, “A Visual Positioning System for Vehicle or Mobile Robot Navigation,” *IEICE Trans D: Information*, E89-D, pp. 2109 - 2116, July 2006.
- [78] Z. BIAN, H. ISHII, H. SHIMODA, and M. IZUMI, “Real-Time Tracking Error Estimation for Augmented Reality for Registration with Linecode Markers,” *IEICE Trans. Inf. & Syst.*, vol.E91-D, no. 7, pp. 2041-2050, July 2008.
- [79] C. C. Yang, M. M. Marefat, and F. W. Ciarallo, “Error Analysis and Planning Accuracy for Dimensional Measurement in Active Vision Inspection,” *IEEE Trans. Robot. Automat.*, vol. 14, pp. 476-487, 1998.
- [80] B. Kamgar-Parsi and B. Kamgar-Parsi, “Evaluation of Quantization Error in Computer Vision,” *IEEE Trans. Pattern Analysis and Machine Intelligence*, vol. 11, no. 9, pp. 929-939, 1989.
- [81] H. Takahashi, D. Ukishima, K. Kawamoto, and K. Hirota, “A Study on Predicting Hazard Factors for Safe Driving,” *IEEE Trans. Ind. Electron.*, vol. 54, no. 2, pp. 781-789, Apr. 2007.
- [82] M. Wada, K. S. Yoon, and H. Hashimoto, “Development of advanced parking assistance system,” *IEEE Trans. Ind. Electron.*, vol. 50, no. 1, pp. 4-17, Feb. 2003.
- [83] G. Ogawa, K. Kise, T. Torii, and T. Nagao, “Onboard Evolutionary Risk Recognition System for Automobiles—Toward the Risk Map System,” *IEEE Trans. Ind. Electron.*, vol. 54, no. 2, pp. 878-886, Apr. 2007.
- [84] T. Bucher, C. Curio, J. Edelbrunner, C. Igel, D. Kastrup, I. Leefken, G. Lorenz, A.

- Steinhage, and W. V. Seelen, "Image processing and behavior planning for intelligent vehicles," *IEEE Trans. Ind. Electron.*, vol. 50, no. 1, pp. 62-75, Feb. 2003.
- [85] A. Kuma, "Computer-Vision-Based Fabric Defect Detection: A Survey," *IEEE Trans. Ind. Electron.*, vol. 55, no. 1, pp. 348-363, Jan. 2008.
- [86] S. Kim, J. H. Park, S. I. Cho, S. Park, K. Lee, and K. Choi, "Robust Lane Detection for Video-Based Navigation Systems," in *Proc. the 19th IEEE International Conference on Tools with Artificial Intelligence*, pp. 535-538, Oct. 2007.
- [87] Y. Wang, E. Teoh, and D. shen, "Lane detection and tracking using B-Snake," *Image Vis. Comput.*, vol. 22, no. 4, pp. 269-280, Apr. 2004.
- [88] D. Heng, R. Oruganti, and D. Srinivasan, "Neural Controller for UPS Inverters Based on B-Spline Network," *IEEE Trans. Ind. Electron.*, vol. 55, no. 2, pp. 899-909, Feb. 2008.
- [89] Z. Lin; D. S. Reay, B. W. Williams, and X. He, "Online Modeling for Switched Reluctance Motors Using B-Spline Neural Networks," *IEEE Trans. Ind. Electron.*, vol. 54, no. 6, pp. 3317-3322, Dec. 2007.
- [90] Y. Wang, E. K. Teoh, and D. Shen, "Lane Detection Using B-Snake," in *Proc. IEEE Trans. on Information Intelligence and Systems*, pp. 438-443, 31 Oct.-3 Nov. 1999.
- [91] K. Szabat and T. Orłowska-Kowalska, "Performance Improvement of Industrial Drives With Mechanical Elasticity Using Nonlinear Adaptive Kalman Filter," *IEEE Trans. Ind. Electron.*, vol. 55, no. 3, pp. 1075-1084, Mar. 2008.
- [92] M. Chueh, Y. L. W. Au Yeung, K.-P.C. Lei, and S. S. Joshi, "Following Controller for Autonomous Mobile Robots Using Behavioral Cues," *IEEE Trans. Ind. Electron.*, vol. 55, no. 8, pp. 3124-3132, Aug. 2008.
- [93] L .Fletcher, N. Apostoloff, L. Petersson, A. Zelinsky, "Vision in and out of Vehicles," *IEEE Transactions on Intell. Syst.* Vol. 18, pp. 12-17, May-June 2003.

- [94] Takeo Kato, Yoshiki Ninomiya, Ichiro Masaki, "Preceding Vehicle Recognition Based on Learning From Sample Images," *IEEE Transactions on. Intell. Trans. Syst.*, Vol. 3, No. 4, pp. 252-260, Dec. 2002.
- [95] D.M. Gavrila, U. Franke, C. Wohler, S. Gorzig, "Real-Time Vision for Intelligent Vehicles," *IEEE Instrumentation & Measurement Magazine* , Vol. 4, pp. 22 – 27, June 2001.
- [96] Nelson H., C. Yung, Chan Ye, "An Intelligent Mobile Vehicle Navigator Based on Fuzzy Logic and Reinforcement Learning," *IEEE Transactions on Syst., Man, Cybern. Part B: Cybernetics*, Vol. 29, No.2, pp. 314-321, April 1999.
- [97] S. Sugimoto, H. Tateda, H. Takahashi, M. Okutomi, "Obstacle Detection Using Millimeter-wave Radar and Its Visualization on Image Sequence," in *Proc. ICPR*, pp. 342 – 345, 2004.
- [98] R. Labayrade, J. Douret, J. Laneurit, and R. Chapuis, "A Reliable and Robust Lane Detection System Based on the Parallel Use of Three Algorithms for Driving Safety Assistance," *IEICE Trans. Inf. & Syst.*, vol.E89-D, no. 7, pp. 2092-2100, July 2006.

VITA



博 士 生：林全財(Chuan-Tsai Lin)

指導教授：吳炳飛(Bing-Fei Wu)

論文題目：影像處理與電腦視覺技術應用於駕駛輔助系統之研究 (A Study of Image Processing and Computer Vision Techniques for Driving Assistance Systems)

學歷

1. 79年9月~83年6月
2. 87年9月~89年6月
3. 92年9月~ now

國立彰化師範大學工業教育學系

國立中正大學電機工程研究所

國立交通大學電機與控制工程學系博士班



經歷

1. 83年8月~88年7月
2. 84年7月~86年6月
3. 89年8月~94年7月
4. 88年8月~now

國立基隆海事職業學校電子通信科 教師

空軍少尉軍官(預官)

國立彰化師範大學附屬高工電子科 教師兼電子科主任

國立彰化師範大學附屬高工電子科 教師

Publication List

Journal Papers

- [1] Bing-Fei Wu and Chuan-Tsai Lin, “Real-Time Fuzzy Vehicle Detection Based on Contour Size Similarity,” *International Journal of Fuzzy Systems*, vol. 7, No. 2, pp. 54-62, June 2005. (SCI, EI)
- [2] Bing-Fei Wu, Chuan-Tsai Lin, and Yen-Lin Chen, “Dynamic Calibration and Occlusion Handling Algorithms for Lane Tracking,” *IEEE Transactions on Industrial Electronics*, vol. 56, No 5, pp. 1757-1773, May 2009. (SCI, EI, 2007 IF=2.216)
- [3] Yen-Lin Chen, Bing-Fei Wu, Chuan-Tsai Lin, Chung-Jui Fan, and Chih-Ming Hsieh, “Real-time Vision-based Vehicle Detection and Tracking on a Moving Vehicle for Nighttime Driver Assistance,” accepted for publication in *International Journal of Robotics and Automation*. (SCI, EI)
- [4] Bing-Fei Wu, Chuan-Tsai Lin, and Chao-Jung Chen, “Real-time Lane and Vehicle Detection Based on a Single Camera Model,” accepted for publication in *International Journal of Computers and Applications*. (EI)
- [5] Bing-Fei Wu, Chuan-Tsai Lin, and Yen-Lin Chen , “Range and Size Estimation Based on a Coordinate Transformation Model for Driving Assistance Systems,” accepted for publication in *IEICE Transactions on Information and Systems*. (SCI, EI)

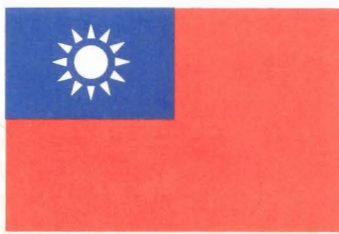
Conference Papers

- [1] Bing-Fei Wu and Chuan-Tsai Lin, “Robust Image Measurement and Analysis Based on Perspective Transformations,” *Proceedings of the IEEE Syst., Man, Cybern. Symp.*, pp.2390-2395, Oct. 2006.
- [2] Bing-Fei Wu and Chuan-Tsai Lin, “A Fuzzy Vehicle Detection Based on Contour Size Similarity,” *Proceedings of the IEEE Intelligent Vehicles*

- Symp.*, pp. 495-500, June 6-8, 2005.
- [3] Yen-Lin Chen, Chuan-Tsai Lin, Chung-Jui Fan, Chih-Ming Hsieh, and Bing-Fei Wu, "Vision-based Nighttime Vehicle Detection and Range Estimation for Driver Assistance," in *Proceedings of the 2008 IEEE International Conference on Systems, Man and Cybernetics(SMC2008)*, pp. 2988-2993, Oct. 2008.
- [4] Bing-Fei Wu and Chuan-Tsai Lin, "Robust Lane Detection and Tracking for Driving Assistance Systems," *Proceedings of the IEEE Syst., Man, Cybern. Symp.*, pp. 3848-3853, Oct. 2007.
- [5] Bing-Fei Wu, Chuan-Tsai Lin, and Chao-Jung Chen, "A Fast Lane and Vehicle Detection Approach for Autonomous Vehicles," *Proceedings of the 7th IASTED International Conference on Signal and Image Processing*, pp. 305-310, August 15-17, 2005.
- [6] Bing-Fei Wu, Yen-Lin Chen, Yuan-Hsin Chen, Chao-Jung Chen, and Chuan-Tsai Lin, "Real-Time Image Segmentation and Rule-based Reasoning for Vehicle Head Light Detection on a Moving Vehicle," *Proceedings of the 7th IASTED International Conference on Signal and Image Processing*, pp. 388-393, August 15-17, 2005, Honolulu, Hawaii, USA.
- [7] Bing-Fei Wu, Chuan-Tsai Lin, and Yen-Lin Chen, "Robust Lane Tracking in Diverse Environmental Conditions," in *Proceedings of the 16th National Conference on Fuzzy Theory and Its Applications*, pp. 121-126, Dec. 2008.
- [8] 吳炳飛、林全財、陳彥霖，"基於視覺的車道偵測與追蹤演算法"，中華民國九十六年全國計算機會議(2007 National computer Symposium)，第 509~516 頁，2007 年 12 月。
- [9] 陳彥霖、謝至明、林全財、吳炳飛，"智慧型夜間駕駛安全輔助暨即時監控系統之研究"，中華民國九十六年全國計算機會議(2007 National computer Symposium)，第 517~530 頁，2007 年 12 月。

Patents

- [1] 「車輛周圍障礙物之偵測方法及顯示方法」，吳炳飛、林全財，中華民國發明專利，發明第 I 304776 號。



中華民國專利證書

發明第 I 304776 號

發明名稱：車輛周圍障礙物之偵測方法及顯示方法

專利權人：國立交通大學

發明人：吳炳飛、林全財

專利權期間：自2009年1月1日至2025年3月24日止

上開發明業經專利權人依專利法之規定取得專利權

經濟部智慧財產局

局長

王美花

中華民國

98



月 1 日

注意：專利權人未依法繳納年費者，其專利權自原繳費期限屆滿之次日消滅。